

A NEW INSIGHT INTO THE CRUSTAL STRUCTURE OF THE
CENTRAL ANATOLIA TO EASTERN MEDITERRANEAN FROM A
WIDE ANGLE SEISMIC DATA

by

Alper Denli

B.S., Geophysical Engineering, Istanbul University, 2004

M.S., Geophysics, Boğaziçi University, 2008

Submitted to the Kandilli Observatory and
Earthquake Research Institute in partial fulfillment of
the requirements for the degree of
Doctor of Philosophy

Graduate Program in Geophysics

Boğaziçi University

2016

ACKNOWLEDGEMENTS

I would like to express my sincere gratitude to my advisors Prof. Dr. Nurcan Meral Ozel for her helpful guidance and Prof. Dr. Cemil Gürbüz who have been encouraging me, supporting me, helping me, giving freedom to select and execute my research subject.

I am grateful to Dr. James Mechie for his propositions about my performance elicit to complete my study with a self-confidence. I would like to express my special thanks to Esen Arpat for sharing his knowledge about geology and tectonics in the study area. German Research Centre of Geosciences (GFZ) provided a financial support and seismic equipments for the project. Also, the University of Hamburg, Delhousie University and the Bogazici University opened their laboratory to use seismic equipments for the project. Expenses for field experiment were provided from the Bogazici University and Massachusetts Institute of Technology's common project (Calibration of Regional Seismic Stations in the Middle East with Shots in Turkey) for the Turkish part. I would like to thank to the members of Departments of geophysics and Regional Earthquake-Tsunami Monitoring Center, Boğaziçi University, Geophysical Deep Sounding section in Geophysics Department of German Research Centre of Geosciences (GFZ) and Geophysics Institute of Hamburg University for data collection and their valuable contribution to field experiment. During this thesis, I was supported by the State Planning Organization of Turkey (DPT) under the TAM Project with Grant No. DPT-2007K 120610. Thanks to this support, I could concentrate only on my research rather than working outside academia.

I would like to acknowledge the spiritual and material support of my parents who helped me to conceive the importance of education and encouraged me through all my life. This goal would not be realized without their concerns and patiences.

ABSTRACT

A NEW INSIGHT INTO THE CRUSTAL STRUCTURES OF THE CENTRAL ANATOLIA TO EASTERN MEDITERRANEAN FROM A WIDE ANGLE SEISMIC DATA

As a part of the CyprusArc project a seismic wide angle reflection/refraction profiles, the 300 km and 45 km long north-south trending profiles extended from Cihanbeyli in Central Anatolia to Anamur in eastern Mediterranean and in southern Cyprus, respectively, in March 2010. The seismic experiment was comprised of two land explosions of 1125 kg explosives onshore and 98 cubic liters airguns offshore. 76 three-component and 119 vertical-component sensors were deployed along ~300 km distances between Cihanbeyli and Anamur with an average spacing of 1.25 km. 25 three-component sensors and 25 vertical component sensors were installed along 45 km distances on land at southern Cyprus with an average spacing of 1.25 km. Appropriate band pass filter was applied for each controlled sources to pick the arrival times. Modelling of the CyprusArc profiles data show that a Moho depth of 38 km at the northern end of the profile which increases 45 km through the southern end of the profile from central Anatolia to eastern Mediterranean. An average P-wave velocity is 6.5 km/s beneath Tuz Golu basin till approximately 23 km depth. P-wave velocity of some rock materials which brought into the open by Taurus Mountains is 5.5 – 5.6 km/s till 5 km thickness. A high velocity block (average P-wave velocity is 6 km/s) between 120 -150 km offset, till 8 km thickness probably correspond to ophiolite complex belong to Troodos. 2-D crustal P-wave velocity model shows crustal thinning between south Turkey and Cyprus from 45 km to 30 km. Final 2-D P-wave velocity models were further refined by generating synthetic seismograms to observe the theoretical travel times and amplitudes of the various arrivals. Additionally, 2-D gravity modelling was done to check robustness of the unresolved part of models by seismic phases and the all results were correlated with geology, tectonics and previous investigations in the study area.

ÖZET

ORTA ANADOLU' DAN DOĞU AKDENİZ'E KABUK YAPISINA İLİŞKİN YENİ BİR BAKIŞ

Mart 2010'da Kıbrıs yayı projesi kapsamında, Orta Anadolu'da Cihanbeyli'den Doğu Akdeniz'de Anamur'a kadar 300 km ve güney Kıbrıs'ta 45 km uzunluğunda Kuzey-Güney doğrultulu profiller boyunca geniş açılı sismik yansıma/kırılma çalışması yapılmıştır. Bu çalışmada yapay kaynak olarak karada 1125 kg'lık iki patlayıcı, Kıbrıs'ın güneyinde akdenizde ise 98 litre küplük airgunlar kullanılmıştır. Cihanbeyli ile Anamur arasına yaklaşık 300 km'lik doğrultu boyunca 76 tane üç bileşen ve 119 tane de düşey bileşen sismometreler aralarında ortalama 1.25 km'lik mesafeler ile kurulmuştur. Güney Kıbrıs'ta da yaklaşık 45 km'lik profil boyunca 25 tane üç bileşen, 25 tane de düşey bileşen sismometreler aralarında ortalama 1.25 km'lik mesafeler ile kurulmuştur. Herbir yapay kaynak için faz okuması uygun bant geçişli filtreler kullanılarak yapılmıştır. Data seti için yapılan modelleme sonucunda kabuk kalınlığının orta Anadolu'da 38 km ile başlayıp Doğu Akdeniz'de 45 km'ye kadar arttığı gözlemlenmiştir. Ortalama P dalga hızının Tuz Gölü havzasında 23 km derinlikte 6.5 km/s olduğu görülmüştür. Profilin orta Toroslari kestiği kısımlarda sığ derinlikler için göreceli olarak daha yüksek P dalgası hızlarının (5.5 – 5.6 km/s) varlığı gözlemlenmiştir. Güney Kıbrıs'ta profilin Trodos masifini kestiği yerde sığ derinliklerde P dalga hızının (6 km/s) göreceli olarak daha yüksek olduğu dikkat çekicidir. Elde edilen P dalgası hız modelinde kabuk kalınlığının Türkiye'nin güneyinden Kıbrıs'a doğru 45 km'den 30 km'ye kadar incelendiği de gözlemlenmiştir. Veri işlem sonucunda elde edilen 2 boyutlu P hızına ait modeller esas alınarak teorik seyahat zamanları ve gözlemlenen sismik fazlara ait genliklerin kıyaslanabilmesi amacıyla yapay sismogramlar üretilmiştir. Ek olarak, elde edilen 2 boyutlu P dalga hızı modellerinde sismik fazlar tarafından çözümlenmemiş kısımların doğruluğunu kontrol etmek amacıyla gravite modellemesi de yapılmıştır. Elde edilen tüm sonuçlar çalışma sahasının jeolojik ve tektonik özellikleri ve yine aynı saha içerisinde gerçekleştirilmiş jeofizik çalışmalar ile ilişkilendirilmeye çalışılmıştır.

TABLE OF CONTENTS

ACKNOWLEDGEMENTS.....	iii
ABSTRACT.....	iv
ÖZET.....	v
LIST OF FIGURES.....	viii
LIST OF TABLES.....	xviii
LIST OF SYMBOLS.....	xix
LIST OF ACRONYMS / ABBREVIATIONS.....	xx
1. INTRODUCTION.....	1
2. GEOLOGY AND TECTONIC SETTING.....	5
2.1. Tectonics in the region.....	5
2.2. Geology in the region.....	9
2.3. Seismicity in the region.....	14
2.4. Previous studies in the region.....	17
3. METHODOLOGY.....	21
3.1. Forward Modelling.....	21
3.2. Ray Tracing.....	21
3.2.1. Calculation of Ray Paths and Travel Times for Reflected Phases.....	23
3.2.1.1. Classical Ray Tracing Technique.....	23
3.2.1.2. Shooting Method.....	27
3.2.2. Calculation of Ray Paths and Travel times for Refracted Phases.....	28
3.3. Synthetic Seismograms: A finite-difference approach.....	35
3.4. Theoretic Gravity Computation.....	41
4. DATA ACQUISITION.....	46
4.1. Field Experiment.....	46
4.2. Instrumentation.....	48
5. DATA PROCESSING.....	49
5.1. Creating Shot Gathers.....	49
5.2. Seismic Data and Phase Correlations.....	49
6. 2-D TRAVEL TIME MODELLING RESULTS.....	62

7. RESULTS OF SYNTHETIC SEISMOGRAMS.....	78
8. RESULTS OF GRAVITY MODELLING ALONG THE WRR PROFILES.....	90
9. DISCUSSION AND CONCLUSIONS.....	95
REFERENCES.....	98

LIST OF FIGURES

- Figure 2.1. Tectonic map of Turkey (modified from Taymaz *et al.*, 2007). Red triangle shows study area. NAF, North Anatolian Fault; EAF, East Anatolian Fault; DSF, Dead Sea Fault; NEAF, North East Anatolian Fault; EPF, Ezinepazarı Fault; PTF, Paphos Transform Fault; CTF, Cephalonia Transform Fault; PSF, Pampak–Sevan Fault; AS, Apsheron Sill; GF, Garni Fault; OF, Ovacık Fault; MT, Mus, Thrust Zone; TUF, Tutak Fault; TF, Tebriz Fault; KBF, Kavakbası Fault; MRF, Main Recent Fault; KF, Kagızman Fault; IF, Iğdır Fault; BF, Bozova Fault; EF, Elbistan Fault; SaF, Salmas Fault; SuF, Surgu Fault; G, Gokova; BMG, Buyuk Menderes Graben; Ge, Gediz Graben; Si, Simav Graben; BuF, Burdur Fault; BGF, Beysehir Golu Fault; TF, Tatarlı Fault; SuF, Sultandag Fault; TGF, Tuz Golu Fault; EcF, Ecemis Fault; ErF, Erciyes Fault; DF, Deliler Fault; MF, Malatya Fault; KFZ, Karatas,–Osmaniye Fault Zone; TM, Taurus Mountain; CB, Cilicia Basin.....6
- Figure 2.2. Previous tectonic classifications of some of the main continental and continental margin units exposed in southern Turkey (modified from Özgül 1984a, b).....10
- Figure 2.3. Geological map of the Central Anatolia and the Eastern Mediterranean regions (Geological Map of Turkey, Konya sheet, 1:800000, 1944. Ankara. Black dots show seismic stations along wide-angle reflection/refraction (WRR) profile).....11
- Figure 2.4. Geological map of Cyprus (Geological Map of Cyprus, 1:250000, 1995. Geological Survey Department, Ministry of Agriculture, Natural Resources and Environment, Government of Cyprus). Black dots show seismic stations along profile. Red triangle show study area (top left, modified from Kinnaird *et al.*, 2011).....14
- Figure 2.5. Distribution of seismicity for the study area from 1900 to 2015 (KOERI and USGS catalogs). Black dots show seismic stations along wide-angle reflection/refraction (WRR) profile.....16

Figure 2.6. Crustal thickness map obtained from station delays (Mutlu and Karabulut, 2011).....	18
Figure 3.1. Flow diagrams of forward modelling (Sharma, 1997).....	21
Figure 3.2. Schematic representation of shooting approach. The trajectory of the initial ray at the source is perturbed until the receiver is reached (Thurber, 1993).....	27
Figure 3.3. (a). Grid layout for the brute force mapping approach. The star denotes the source location. (b). One constant slowness grid cell with minimum time raypath impinging upon the node where t is to be computed (Schneider <i>et al.</i> , 1992).....	30
Figure 3.4. The three left-most columns of the grid are shown in (a) and repeated again in (b). The centers of the columns have been “cut away” for clarity. The four configuration types that are used to compute a new time t , on column 2, from a pair of known times t_1 and t_2 , on columns 1 and 2 are illustrated. A star denotes the source point.....	31
Figure 3.5. Density distribution $\rho(\hat{r}_0)$ within volume V as seen from field point \hat{r}	41
Figure 3.6. Geometry of 2.5 –D body, z-axis is positive down, y-axis is along strike, and traverse is along x-axis. A is the angle between the x-axis and true north, and D is the declination of the earth’s magnetic field, both positive clockwise. I is the inclination of the earth’s magnetic field.....	42
Figure 3.7. The x-z relationship along one side of the polygonal cross-section.....	44
Figure 4.1. Seismic experiments in Turkey and south Cyprus. The 300 km long wide angle reflection/refraction profile and the 45 km long profile (black dots). Red stars show explosions. Yellow stars show airguns.....	47

Figure 4.2. Seismic recorders (top), vertical component sensors (middle) and three component sensors (bottom).....48

Figure 5.1. Seismic record section of southern land shot of Turkey. Red dots show picked first arrival times. Green solid lines show calculated first arrival times (P_g) and green dashed lines show calculated travel times from reflected phases from the Moho (P_mP), based on the final 2-D P wave velocity model. Seismic traces are plotted after DC removal. The amplitudes were normalized by the maximum of each trace and geometric spreading effect was alleviated. The trace at 0 m shows the seismic signal recorded close to shot locations.....51

Figure 5.2. Seismic record section of northern land shot of Turkey. Red dots show picked first arrival times and reflected phases. Green solid lines show calculated first arrival times (P_g) and P_n and green dashed lines show calculated travel times from reflected phases from the Moho (P_mP), based on the final 2-D P wave velocity model. Seismic traces are plotted after DC removal. The amplitudes were normalized by the maximum of each trace and geometric spreading effect was alleviated. The trace at 0 m shows the seismic signal recorded close to shot locations.....52

Figure 5.3. Seismic record section of southern land shot of Turkey. Red dots show picked first arrival times. Green solid lines show calculated first arrival times (P_g and P_1) based on the final 2-D P-wave velocity model. Seismic traces are plotted after DC removal. The amplitudes were normalized by the maximum of each trace and geometric spreading effect was alleviated. The trace at 0 m shows the seismic signal recorded close to shot locations.....53

Figure 5.4. Seismic record section of Airgun 38. Red dots show picked first arrival times. Green solid lines show calculated first arrival times (P_g) based on the final 2-D P-wave velocity model. Seismic traces are plotted after DC removal. The amplitudes were normalized by the maximum of each trace and geometric spreading effect was alleviated.....54

Figure 5.5. Seismic record section of Airgun 50. Red dots show picked first arrival times. Green solid lines show calculated first arrival times (Pg) based on the final 2-D P-wave velocity model. Seismic traces are plotted after DC removal. The amplitudes were normalized by the maximum of each trace and geometric spreading effect was alleviated.....55

Figure 5.6. Seismic record section of Airgun 75. Red dots show picked first arrival times. Green solid lines show calculated first arrival times (Pg) based on the final 2-D P-wave velocity model. Seismic traces are plotted after DC removal. The amplitudes were normalized by the maximum of each trace and geometric spreading effect was alleviated.....56

Figure 5.7. Seismic record section of Airgun 100. Red dots show picked first arrival times. Green solid lines show calculated first arrival times (Pg) based on the final 2-D P-wave velocity model. Seismic traces are plotted after DC removal. The amplitudes were normalized by the maximum of each trace and geometric spreading effect was alleviated.....57

Figure 5.8. Seismic record section of Airgun 125. Red dots show picked first arrival times. Green solid lines show calculated first arrival times (Pg) based on the final 2-D P-wave velocity model. Seismic traces are plotted after DC removal. The amplitudes were normalized by the maximum of each trace and geometric spreading effect was alleviated.....58

Figure 5.9. Seismic record section of Airgun 158. Red dots show picked first arrival times. Green solid lines show calculated first arrival times (Pg) based on the final 2-D P-wave velocity model. Seismic traces are plotted after DC removal. The amplitudes were normalized by the maximum of each trace and geometric spreading effect was alleviated.....59

Figure 5.10. Seismic record section of Airgun 175. Red dots show picked first arrival times. Green solid lines show calculated first arrival times (Pg) based on the final 2-D P-wave velocity model. Seismic traces are plotted after DC removal. The amplitudes were

normalized by the maximum of each trace and geometric spreading effect was alleviated.....60

Figure 5.11. Seismic record section of Airgun 200. Red dots show picked first arrival times. Green solid lines show calculated first arrival times (Pg) based on the final 2-D P-wave velocity model. Seismic traces are plotted after DC removal. The amplitudes were normalized by the maximum of each trace and geometric spreading effect was alleviated.....61

Figure 6.1. a) Seismic record section of southern land shot of Turkey b) Seismic record section of northern land shot of Turkey. Red dots show picked first arrival times. Green solid lines show calculated first arrival times based on the 2-D P wave velocity model c) 2-D P-wave velocity model.....64

Figure 6.2. a) Seismic record section of southern land shot of Turkey b) Seismic record section of northern land shot of Turkey. Red dots show picked first arrival times. Green solid lines show calculated first arrival times based on the 2-D P wave velocity model c) 2-D P-wave velocity model.....65

Figure 6.3. a) Seismic record section of southern land shot of Turkey b) Seismic record section of northern land shot of Turkey. Red dots show picked first arrival times. Green solid lines show calculated first arrival times based on the 2-D P wave velocity model c) 2-D P-wave velocity model.....66

Figure 6.4. a) Seismic record section of airgun 38 b) Seismic record section of southern land shot of Turkey. Red dots show picked first arrival times. Green solid lines show calculated first arrival times based on the 2-D P wave velocity model c) 2-D P-wave velocity model.....67

Figure 6.5. a) Ray diagram for refractions, b) Ray diagram for reflections, c) Final 2-D crustal P wave velocity model was produced after travel time modelling by using refractions and reflections are shown. Numbers denote P wave velocity, thick black line shows subsurface layers in the model and red stars indicate locations of land shots.

Raypath with picked travel time is plotted with a thin solid line, raypath without picked travel time is plotted with a thin dashed line. ** = indicate shaded areas which are not resolved by seismic phases, but resolved by gravity modelling. TGB: Tuz Golu Basin, CAP: Central Anatolian Plateau.....68

Figure 6.6. a) Ray diagram for refractions, b) Final 2-D crustal P wave velocity model between southern land shot and airgun shot 38 in the sea was produced after travel time modelling by using refractions. Numbers denote P wave velocity, thick black line shows subsurface layers in the model. Red and yellow stars indicate locations of land shot and airgun, respectively. Raypath with picked travel time is plotted with a thin solid line. ** = shaded areas not resolved by seismic phases, but resolved by gravity modelling. CT: Central Taurides, CB: Cilicia Basin.....70

Figure 6.7. a) Ray diagram for refractions, b) Final 2-D crustal P wave velocity model between southern land shot and airgun shot 50 in the sea was produced after travel time modelling by using refractions. Numbers denote P wave velocity, thick black line shows subsurface layers in the model. Red and yellow stars indicate locations of land shot and airgun, respectively. Raypath with picked travel time is plotted with a thin solid line. ** = shaded areas not resolved by seismic phases, but resolved by gravity modelling. CT: Central Taurides, CB: Cilicia Basin.....71

Figure 6.8. a) Ray diagram for refractions, b) Final 2-D crustal P wave velocity model between southern land shot and airgun shot 75 in the sea was produced after travel time modelling by using refractions. Numbers denote P wave velocity, thick black line shows subsurface layers in the model. Red and yellow stars indicate locations of land shot and airgun, respectively. Raypath with picked travel time is plotted with a thin solid line. ** = shaded areas not resolved by seismic phases, but resolved by gravity modelling. CT: Central Taurides, CB: Cilicia Basin.....72

Figure 6.9. a) Ray diagram for refractions, b) Final 2-D crustal P wave velocity model between southern land shot and airgun shot 100 in the sea was produced after travel time modelling by using refractions. Numbers denote P wave velocity, thick black line shows subsurface layers in the model. Red and yellow stars indicate locations of land shot and

airgun, respectively. Raypath with picked travel time is plotted with a thin solid line. ** = shaded areas not resolved by seismic phases, but resolved by gravity modelling. CT: Central Taurides, CB: Cilicia Basin.....73

Figure 6.10. a) Ray diagram for refractions, b) Final 2-D crustal P wave velocity model between southern land shot and airgun shot 125 in the sea was produced after travel time modelling by using refractions. Numbers denote P wave velocity, thick black line shows subsurface layers in the model. Red and yellow stars indicate locations of land shot and airgun, respectively. Raypath with picked travel time is plotted with a thin solid line. ** = shaded areas not resolved by seismic phases, but resolved by gravity modelling. CT: Central Taurides, CB: Cilicia Basin.....74

Figure 6.11. a) Ray diagram for refractions, b) Final 2-D crustal P wave velocity model between southern land shot and airgun shot 158 in the sea was produced after travel time modelling by using refractions. Numbers denote P wave velocity, thick black line shows subsurface layers in the model. Red and yellow stars indicate locations of land shot and airgun, respectively. Raypath with picked travel time is plotted with a thin solid line. ** = shaded areas not resolved by seismic phases, but resolved by gravity modelling. CT: Central Taurides, CB: Cilicia Basin.....75

Figure 6.12. a) Ray diagram for refractions, b) Final 2-D crustal P wave velocity model between southern land shot and airgun shot 175 in the sea was produced after travel time modelling by using refractions. Numbers denote P wave velocity, thick black line shows subsurface layers in the model. Red and yellow stars indicate locations of land shot and airgun, respectively. Raypath with picked travel time is plotted with a thin solid line. ** = shaded areas not resolved by seismic phases, but resolved by gravity modelling. CT: Central Taurides, CB: Cilicia Basin.....76

Figure 6.13. a) Ray diagram for refractions, b) Final 2-D crustal P wave velocity model between southern land shot and airgun shot 200 in the sea was produced after travel time modelling by using refractions. Numbers denote P wave velocity, thick black line shows subsurface layers in the model. Red and yellow stars indicate locations of land shot and airgun, respectively. Raypath with picked travel time is plotted with a thin solid line. ** =

shaded areas not resolved by seismic phases, but resolved by gravity modelling. CT: Central Taurides, CB: Cilicia Basin.....77

Figure 7.1. Synthetic seismogram section, computed with the finite-difference technique, for shot1 along WRR profile. Reduction velocity is 8 km/s for the record section denotes the vertical component of P wave motion in which each trace is normalized individually. Continuous and dashed green lines show phases computed from the model presented in Figure 6.5c.....79

Figure 7.2. Synthetic seismogram section, computed with the finite-difference method, for shot2 along WRR profile. Reduction velocity is 8 km/s for the record section denotes the vertical component of P wave motion in which each trace is normalized individually. Continuous and dashed green lines show phases computed from the model presented in Figure 6.5c.....80

Figure 7.3. Synthetic seismogram section, computed with the finite-difference technique, for shot1 along WRR profile. Reduction velocity is 8 km/s for the record section denotes the vertical component of P wave motion in which each trace is normalized individually. Continuous and dashed green lines show phases computed from the model presented in Figure 6.6.....81

Figure 7.4. Synthetic seismogram section, computed with the finite-difference technique, for airgun 38 along WRR profile. Reduction velocity is 6 km/s for the record section denotes the vertical component of P wave motion in which each trace is normalized individually. Continuous and dashed green lines represent phases computed from the model presented in Figure 6.6.....82

Figure 7.5. Synthetic seismogram section, computed with the finite-difference technique, for airgun 50 along WRR profile. Reduction velocity is 6 km/s for the record section denotes the vertical component of P wave motion in which each trace is normalized individually. Continuous and dashed green lines show phases computed from the model presented in Figure 6.7.....83

Figure 7.6. Synthetic seismogram section, computed with the finite-difference technique, for airgun 75 along WRR profile. Reduction velocity is 6 km/s for the record section denotes the vertical component of P wave motion in which each trace is normalized individually. Continuous and dashed green lines show phases computed from the model presented Figure 6.8.....84

Figure 7.7. Synthetic seismogram section, computed with the finite-difference technique, for airgun 100 along WRR profile. Reduction velocity is 6 km/s for the record section denotes the vertical component of P wave motion in which each trace is normalized individually. Continuous and dashed green lines show phases computed from the model presented in Figure 6.9.....85

Figure 7.8. Synthetic seismogram section, computed with the finite-difference technique, for airgun 125 along WRR profile. Reduction velocity is 6 km/s for the record section denotes the vertical component of P wave motion in which each trace is normalized individually. Continuous and dashed green lines show phases computed from the model presented in Figure 6.10.....86

Figure 7.9. Synthetic seismogram section, computed with the finite-difference technique, for airgun 158 along WRR profile. Reduction velocity is 6 km/s for the record section denotes the vertical component of P wave motion in which each trace is normalized individually. Continuous and dashed green lines show phases calculated from the model presented in Figure 6.11.....87

Figure 7.10. Synthetic seismogram section, computed with the finite-difference technique, for airgun 175 along WRR profile. Reduction velocity is 6 km/s for the record section denotes the vertical component of P wave motion in which each trace is normalized individually. Continuous and dashed green lines show phases computed from the model shown in Figure 6.12.....88

Figure 7.11. Synthetic seismogram section, computed with the finite-difference technique, for airgun 200 along WRR profile. Reduction velocity is 6 km/s for the record section denotes the vertical component of P wave motion in which each trace is normalized

individually. Continuous and dashed green lines show phases computed from the model presented in Figure 6.13.....89

Figure 8.1. a) The calculated gravity values (circles) compared to observed gravity values (Pink solid line shows gravity values from Makris and Wang, 1994; blue dashed line shows gravity values from Ergün *et al.*, 2005; red solid line shows gravity values obtained from General Directorate of Mineral Research and Exploration (MTA); turquoise blue dashed line shows gravity values from Aydemir and Ateş, 2006). b) Final gravity model. Numbers denote density in g/cm^3 93

Figure 8.2. a) The calculated gravity values (circles) compared to observed gravity values (Pink solid line shows gravity values from Makris and Wang, 1994; blue dashed line shows gravity values from Ergün *et al.*, 2005; green dashed line shows gravity values from Gass and Mason Smith, 1963). b) Final gravity model. Numbers denote density in g/cm^3 94

LIST OF TABLES

Table 8.1. Units of the final 2-D P-wave velocity model and the corresponding density for profile in Turkey. The corresponding density values were derived by equation 8.1.....	90
Table 8.2. Units of the final 2-D P-wave velocity model and the corresponding density for profile in south Cyprus. The corresponding densities were derived by equation 8.1.....	91

LIST OF SYMBOLS

ρ	Slowness vector
α	P wave
β	S wave
φ and δ	Polar angles
S	Slowness
t	Arrival time
S_a	Apparent slowness
f_d	Dominant frequency
Δt	Time increment
Δx	Distance increment
I	Identity operator
θ	Incidence angle
k	Wavenumber
λ and μ	Lame parameters
V	Volume
U	Gravitational potential
G	Universal gravitational constant

LIST OF ACRONYMS/ABBREVIATIONS

2-D	Two Dimensional
3-D	Three Dimensional
BVP	Boundary Value Problem
CAP	Central Anatolian Plateau
CB	Cilicia Basin
CT	Central Taurides
EAF	East Anatolian Fault
EAFZ	East Anatolian Fault Zone
ESM	Eratosthenes Sea Mount
GFZ	GeoForschungsZentrum
GPS	Global Positioning System
LANGASS	Investigations Around North Troodos using Gravity and Seismic Surveys
KOERI	Kandilli Observatory and Earthquake Research Institute
MTA	General Directorate of Mineral Research and Exploration
N	North
NAF	North Anatolian Fault
NAFZ	North Anatolian Fault Zone
NE	Northeast
RMS	Root Mean Square
S	South
SE	Southeast
SW	Southwest
TGB	Tuz Golu Basin
USGS	United States Geological Survey
WRR	Wide-angle reflection/refraction

1. INTRODUCTION

Travel times for seismic waves are classically calculated with ray tracing methods. Contrarily, graphical techniques separated wavefront tracing into examples were suggested by Thornburgh as early as 1930, and also generalized by Riznichenko (1946) to the case of layered media. Vidale (1988, 1990) suggested a general wavefront tracing technique based on a finite difference approximation of the eikonal equation. Saito (1989, 1990) and Moser (1989) applied the graph theory, while Van Trier and Symes (1990, 1991) solved a Hamiltonian representation of the eikonal equation. Qin *et al.* (1990) suggest a progress of Vidale's original algorithm. These techniques are just devoted to calculation of first arrival travel times. According to Van Trier & Symes (1991), this limitation fundamentally originates from mathematical features of the eikonal equation. As a result, on a given model, the finite difference scheme should fail to get several arrival times at a given receiver. However, all existing finite difference techniques up to now encounter serious difficulties when implemented to models including sharp first-order velocity contrast. Podvin and Lecomte (1991) propose a new finite difference algorithm which overcomes both difficulties. This technique based on a systematic implementation of Huygen's principle in the finite difference approximation. Such an approach clearly considers the existence of different propagation modes (transmitted and diffracted body waves, head waves). Local discontinuities of the time gradient in the first arrival time field result, the suggested technique provides exact first travel times in the presence of extremely severe, arbitrarily shaped velocity contrasts (Podvin and Lecomte, 1991). Recently, a two-dimensional dynamic programming travel time calculation method, based on Fermat's principle, suggested. It uses basic computation methods and a systematic mapping scheme to calculate first-arrival times on a uniform grid, given an arbitrary, discrete velocity distribution (Schneider *et al.*, 1992).

In rebuilding the historical progress of basins and their underlying basement, it is important to determine moho depth, from which predicts of, for example, crustal shortening and extension can be made (Ergün *et al.*, 2005). This is best done by forward modelling to obtain 2-D crustal velocity model and gravity modelling to check robustness

of the 2-D velocity model. For the travel time modelling, the forward problem was solved by classical ray tracing techniques (Cerveny *et al.* 1977) for the reflected phases, and finite-difference ray tracing based on the eikonal equation (Vidale 1988; Podvin & Lecomte 1991; Schneider *et al.* 1992) for the first arrival refracted phases. To supplement and guide the travel time modelling, synthetic seismograms were generated, amplitudes were calculated using a finite-difference approximation of the wave equation for 2-D heterogeneous elastic media by Kelly *et al.* (1976) with transparent boundary conditions (Reynolds, 1978) and implemented by Sandmeier (1990). Additionally, to check robustness of the model, gravity computation, which is developed by Talwani *et al.* (1959) and Cady (1980), was performed for final 2-D crustal structure model.

To understand the interaction between the existent of the major geological and tectonic properties related with the tectonic zones and 2-D crustal structure beneath the study areas, we carried out wide-angle reflection/refraction profiles. The Eastern Mediterranean region is a natural laboratory to investigate the various stages of active margin development, including ocean closure and ophiolite formation, continental subduction, continent-continent collision, back-arc basin evolution, slab roll-back and slab-break-off (Yolsal-Çevikbilen and Taymaz, 2012). A major purpose of this study is to provide better constraints on the crustal structure beneath Central Anatolia, Eastern Mediterranean and Cyprus by presenting a 2-D compressional P wave model from an analysis of the P wave data. Having an information about the crustal P wave velocities provides much better constraints on the gravity models along the seismic refraction profiles in the region.

As a part of the CyprusArc project, a seismic wide-angle reflection/refraction profiles were performed in March 2010. The 300 km and 45 km long north – south trending profiles extended from Cihanbeyli in Central Anatolia to Anamur in eastern Mediterranean and in southern Cyprus, respectively. The CyprusArc wide-angle reflection/refraction (WRR) profiles comprised on the source side two land shots of 1125 kg and 98 cubic liters airguns on the sea. The purpose of the land shots was to get arrivals from the whole crust including the Pn arrivals from Moho discontinuity. 77 three-component and 167 vertical-component sensors were installed along ~300 km distances between Cihanbeyli and Anamur with an average station spacing of 1.25 km. 24 three-

component and 21 vertical component sensors were deployed along 45 km distances on land at southern Cyprus with an average station spacing of 1.25 km. During the field experiment, data recorded at different formats which were converted into first SEG-Y and later SAC formats for each receiver, respectively. In chapter 5, the shot gathers were created in SAC format, an uncertainty is calculated by using the signal to noise ratio (S/N ratio) for each pick from the onshore recordings. 390 shot gathers were created for explosions along the 300 km long profile in Turkey and 63 shot gathers were created for the explosion at Anamur and eight airguns along 180 km long profile between south of Turkey and south of Cyprus. Distances less than 60 km (for southern shot point in Turkey) and 40 km (for northern shot point in Turkey), the first arrivals were clearly picked without any filter. A frequency analysis was performed to reveal the dominant frequency content of the main signal. The frequency content of all stations was analyzed by an interactive spectral analysis, which uses the Fourier Transform. For the southern shot-point in Turkey, at short distances (less than 60 km), first arrivals are clearly picked without any filter. Distances between 60 and 130 km through north 1-20 Hz band pass filter and at long distances beyond 130 km 3-10 Hz band pass filters were applied before picking the arrival times. For the northern shot-point in Turkey, at short distances (less than 40 km), first arrivals were clearly picked without any filter. Distances between 40 and 110 km through the south 1-20 Hz band pass filter and at long distances greater than 110 km 3-10 Hz band pass filter were applied before picking the arrival times. For explosions, a delay of 0.542 second due to the firing system has been taken into account. For each receiver recording at the southern Cyprus, first arrivals were picked by applying 4-8 Hz band pass filter to the airgun recordings. After completing data processing, a detailed research was conducted to determine the initial velocity model parameters to start forward modelling and the program based on SEIS81, first written by Vlatislav Cerveny and Ivan Psencik then developed by Pascal Podvin - Isabel Lecomte and James Mechie, was used. A reduced travel time-distance graphs were replotted, after every model modifications, to observe an optimum RMS residual between observed and theoretical data for 2-D travel time modelling (chapter 6). Modelling of the CyprusArc profiles data show that a Moho depth of 38 km at the northern end of the profile which increases to 45 km through the southern end of the profile from central Anatolia to eastern Mediterranean. An average P wave velocity is 6.5 km/s beneath Tuz Golu basin till 23 km depth. P wave velocity of some rock materials which brought into the open by Taurus Mountains is 5.5 – 5.6 km/s till 5 km thickness.

High P wave velocities of 6.5 – 7.2 km/s within the crustal thickness range of 30 – 45 km (from south to north) observed beneath the Cilicia basin. A relatively high velocity block (average P wave velocity is 6 km/s) between 120 -150 km offset, till 8 km thickness probably correspond to ophiolite complex belong to Troodos. 2-D crustal P wave velocity model shows crustal thinning between southern Turkey and Cyprus from 45 km to 30 km. Final 2-D P wave velocity models were further refined by using finite-difference approach to generate synthetic seismograms (chapter 7). Thus by varying the velocity structure, correlation between the theoretical travel times and amplitudes of the various arrivals were observed. General correlation between the observed and theoretical record sections denotes the robustness of final 2-D models. Additionally, 2-D gravity modelling was done by using the obtained final crustal models to check robustness of the unresolved part of models by seismic phases (chapter 8). For gravity modelling, obtained P wave velocity values were converted into densities by using the Birch law. Obtained theoretical gravity anomalies were compared with the observed gravity anomalies and all the results were correlated with geology, tectonics and previous investigations in the study area (chapter 9).

2. GEOLOGY AND TECTONIC SETTING

2.1. Tectonics in the region

Turkey composes one of the most actively deforming regions in the world and has a long history of destructive earthquakes. The preferable comprehension of its neotectonic properties and active tectonics would give an opportunity to understand, not just for the country but also for the whole Eastern Mediterranean region. Active tectonics of Turkey is a kind of declaration of collisional intracontinental convergence- and tectonic escape-associated deformation since the Early Pliocene (~5 Ma). Three main compositions lead to the neotectonics of Turkey; they are dextral North Anatolian Fault Zone (NAFZ), sinistral East Anatolian Fault Zone (EAFZ) and the Aegean–Cyprean Arc. Also, sinistral Dead Sea Fault Zone has a significant role. The Anatolian wedge between the NAFZ and EAFZ has a westward movement through the eastern Anatolia, the collision zone between the Arabian and the Eurasian plates. Continuing deformation along, and collective coactions among them has eventuated in four different neotectonic areas, namely the East Anatolian contractional, the North Anatolian, the Central Anatolian and the West Anatolian extensional provinces. Every region is specified by its original compositional elements, and composes a perfect laboratory to investigate active strike-slip, normal and reverse faulting and the related basin formation (Bozkurt, 2001).

Anatolia is a complicate mixture of a lot of tectonic systems inspected by the mutual effects of the Arabian, African and Anatolia plates. The actual tectonics of the area is controlled by north-ward collision of the Arabian plate and westward extrusion of the Anatolian plate along the NAFZ and EAFZ. Moreover, the northward subduction of African lithosphere along the southwestward withdrawing Aegean trench and blocked Cyprean trench has a significant role in the tectonic progress of the region (Bozkurt, 2001 and Figure 2.1).

Predictions of regional deformation and major fault movements from GPS measurements separate the area into a few major geodynamics zones with the inclusion of the N-S extensional region in western Turkey, an area of strike-slip extension in the

northwest, the stable central interior with < 2 mm yr⁻¹ of internal deformation that is bounded by the North Anatolian and East Anatolian faults and an area of distributed strike-slip deformation in eastern Turkey (Taymaz *et al.*, 1991a,b; McClusky *et al.*, 2000; Şengör *et al.*, 2005; Tan and Taymaz, 2006).

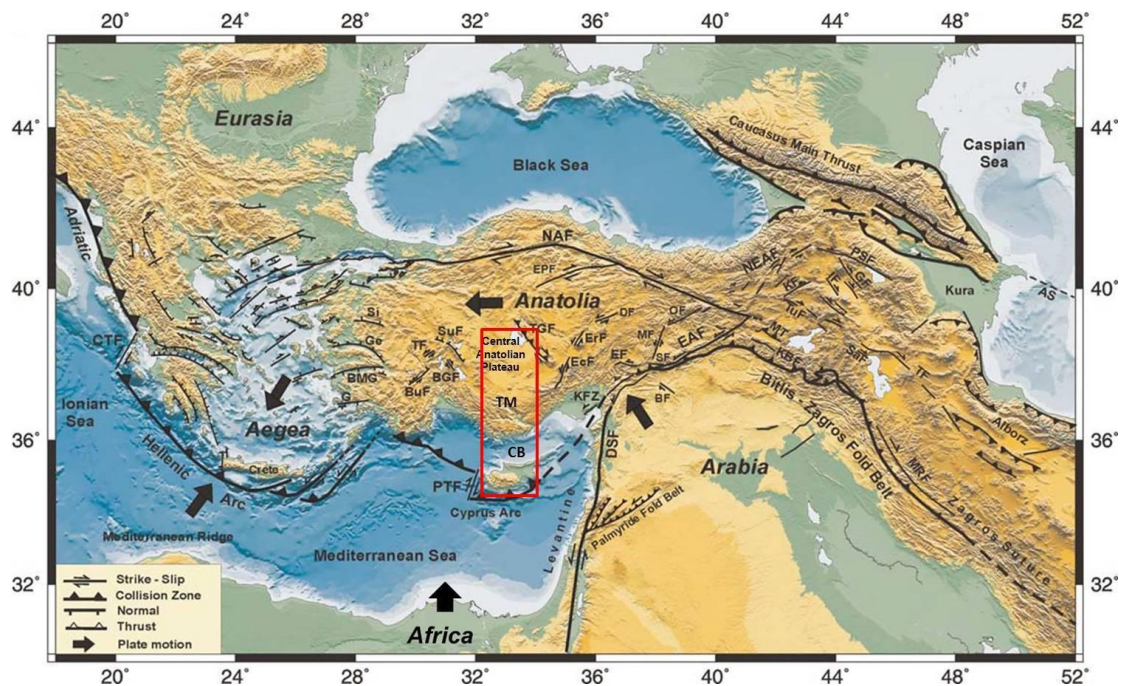


Figure 2.1. Tectonic map of Turkey (modified from Taymaz *et al.*, 2007). Red rectangle shows study area. NAF, North Anatolian Fault; EAF, East Anatolian Fault; DSF, Dead Sea Fault; NEAF, North East Anatolian Fault; EPF, Ezinepazarı Fault; PTF, Paphos Transform Fault; CTF, Cephalonia Transform Fault; PSF, Pampak–Sevan Fault; AS, Apsheron Sill; GF, Garni Fault; OF, Ovacık Fault; MT, Mus, Thrust Zone; TUF, Tutak Fault; TF, Tebriz Fault; KBF, Kavakbası Fault; MRF, Main Recent Fault; KF, Kagızman Fault; IF, Iğdır Fault; BF, Bozova Fault; EF, Elbistan Fault; SaF, Salmas Fault; SuF, Surgu Fault; G, Gokova; BMG, Büyük Menderes Graben; Ge, Gediz Graben; Si, Simav Graben; BuF, Burdur Fault; BGF, Beyşehir Golu Fault; TF, Tatarlı Fault; SuF, Sultandag Fault; TGF, Tuz Golu Fault; EcF, Ecemis Fault; ErF, Erciyes Fault; DF, Deliler Fault; MF, Malatya Fault; KFZ, Karatas,–Osmaniye Fault Zone; TM, Taurus Mountain; CB, Cilicia Basin.

Tectonic plate movement between Arabia and Eurasia becomes complicated in the Eastern Mediterranean, due to free movement of smaller blocks or subplates. The Anatolian block escapes the convergence between Eurasia and Arabia by moving

southwestwards through the Hellenic and Cyprian Arcs (Jackson and McKenzie, 1984; Wdiwonski *et al.*, 2006). The main boundary conditions of the tectonics of the eastern Mediterranean are the northward motion of the Arabian Plate in the SE, the Hellenic subduction in the SW and stationary Eurasia in the north (Figure 2.1). Central Anatolia internally deforms very little and rotates counter-clockwise with respect to stable Eurasia (Platzman *et al.*, 1998; McClusky *et al.*, 2000; Özeren and Holt, 2010).

The Central Taurus Mountains (Ozgul, 1983) are a major neotectonic feature of South-Central Anatolia which is parallel to Cyprus arc. During the early-middle Miocene time Central Anatolia was covered by a large lake whilst the Taurus Mountains were under sea level where extensive carbonate deposition occurred (Şaroglu *et al.*, 1983). Since the mid-late Miocene the Taurus Mountains have been uplifted at least 1000 m relative to the Central Anatolia Plateau. The uplift has been interpreted as a wide anticlinal fold by Şaroglu *et al.* (1983). Barka and Reilinger (1997) suggest that Central Anatolia is under approximately N-S or NE-SW shortening while it is rotating anticlockwise along the North Anatolian Fault (NAF). This shortening probably related to the collisional processes along the Cyprus arc between Africa and Anatolia. Schildgen *et al.* (2012a) emphasize that the Central Taurides, which specify the plateau's southern margin (Figure 2.1), were accreted to crustal blocks to the north starting in the Eocene (Jaffey and Robertson, 2005; Pourceau *et al.*, 2010; Robertson *et al.*, 1996; Şengör and Yılmaz, 1981; Şengör *et al.*, 1984, 1985; Yılmaz *et al.*, 1997), while closure of the Neotethys Ocean to the south and associated Arabia-Eurasia collision (Ballato *et al.*, 2011; Hüsing *et al.*, 2009; Kelling *et al.*, 1987; Robertson, 2000; Şengör *et al.*, 1985; Williams *et al.*, 1995) concluded in westward "escape" of the Anatolian microplate along the North and East Anatolian faults (Dewey and Şengör, 1979; Şengör *et al.*, 1985). Some uplift of Central Anatolia likely resulted from this plate-scale deformation, both along the southern margin prior to the Middle Miocene (Clark and Robertson, 2002, 2005; Jaffey and Robertson, 2005) and at the northern margin due to strain accumulation along the broad constraining bend of the NAF (Yıldırım *et al.*, 2011).

Cilicia basin, between Cyprus and south Turkey, is an intra-mountain basin, presently settled in a fore-arc setting, north of the Cyprus Arc, which compose the convergent boundary between the Africa and Aegean-Anatolian Plates. The morphology of

the sea-floor is largely controlled by major Cyprus Arc and by sediment input from extensive rivers that flow into the basin. The deposition of the basin succession is attributed to the development of a foredeep in front of the evolving Tauride fold-thrust belt (Aksu *et al.*, 2005). The westward pull-out of the Tauride block is associated with the overall westward escape of the Anatolian microplate during the latest Miocene to Pliocene (Dewey *et al.*, 1986). The ongoing contraction south of the basin complex across Cyprus is originated from the evolving collision and under-plating of the Eratosthenes continental micro-fragment (Robertson, 1998). Within this kinematics configuration, the southern main fault of the Cilicia basin principally functions as a boundary, separating a contractional microplate area to the south from a transtensional microplate area to the north (Aksu *et al.*, 2005).

Cyprus was started with the subduction of the African Plate beneath the Eurasian Plate and the composition of the Troodos Ophiolite (Upper Cretaceous, 90 Ma) and ongoing with its segregation, a sinistral rotation of 90° and the collision to its southern and western portion of older rocks. A duration of relative tectonic inaction followed, including in time from almost 75 to 10 Ma, was specified by the deposition of carbonate sediments and gradual shallowing of the sedimentary basin (Circum Troodos areas). The location of the Keryneia Terrane in the northern portion of the Troodos Terrane and the uplift of the island to almost its actual location (Miocene, 10-15 Ma) constitutes a crucial tectonic occurrence (Figure 2.4)([http://www.moa.gov.cy/Tectonic Evolution](http://www.moa.gov.cy/Tectonic%20Evolution)). Shortening and strike-slip faulting have predominated since the late Miocene in the north (Robertson and Woodcock, 1986; Harrison *et al.*, 2004; Calon *et al.*, 2005) and the southwest (Wdowinski *et al.*, 2006), while normal faults and related grabens have formed in other parts of the island (Robertson, 2000; Payne and Robertson, 2000). Shortening is usually seen in seismicity along the collision zone in the south of Cyprus (Imprescia *et al.*, 2012), and also to a lesser degree by the deep earthquakes beneath the Antalya basin related with the subducting “Western Cyprus slab” (Kalyoncuoğlu *et al.*, 2011; Imprescia *et al.*, 2012; Schildgen *et al.*, 2012b).

The boundary between the African plate and the Aegean/Anatolia microplate is in the process of transition from subduction to collision along the Cyprus Arc (Ergün *et al.*, 2005). Arvidsson *et al.* (1998) observed and interpreted the Cyprus Arc as a fragment of

the plate boundary between Eurasia and Africa (McKenzie, 1970). Nevertheless, according to Ben-Avraham (1989), Cyprus may now be observed as a portion of the Anatolian block which is bordered by Arabia along the EAF in the southeast, Africa along the Cyprus and Hellenic arcs in the south and Eurasia along the NAF in the north. The convergence in the west of Cyprus is accommodated by oceanic-continental subduction, whereas south of Cyprus it has been defined as a continental collision between Cyprus and the Eratosthenes seamount. The seamount is of continental origin and is embedded in the African plate (Makris *et al.*, 1983). Tectonic collapse of the Eratosthenes Seamount was approximately synchronous with fast surface uplift of the over-riding plate, the Troodos Ophiolite of southern Cyprus. This uplift is expressed in terms of incipient collision of an Eratosthenes continental segment with a subduction trench, coupled with the impacts of diapiric protrusion of serpentine located within the core of the Troodos Ophiolite (Robertson, 1998).

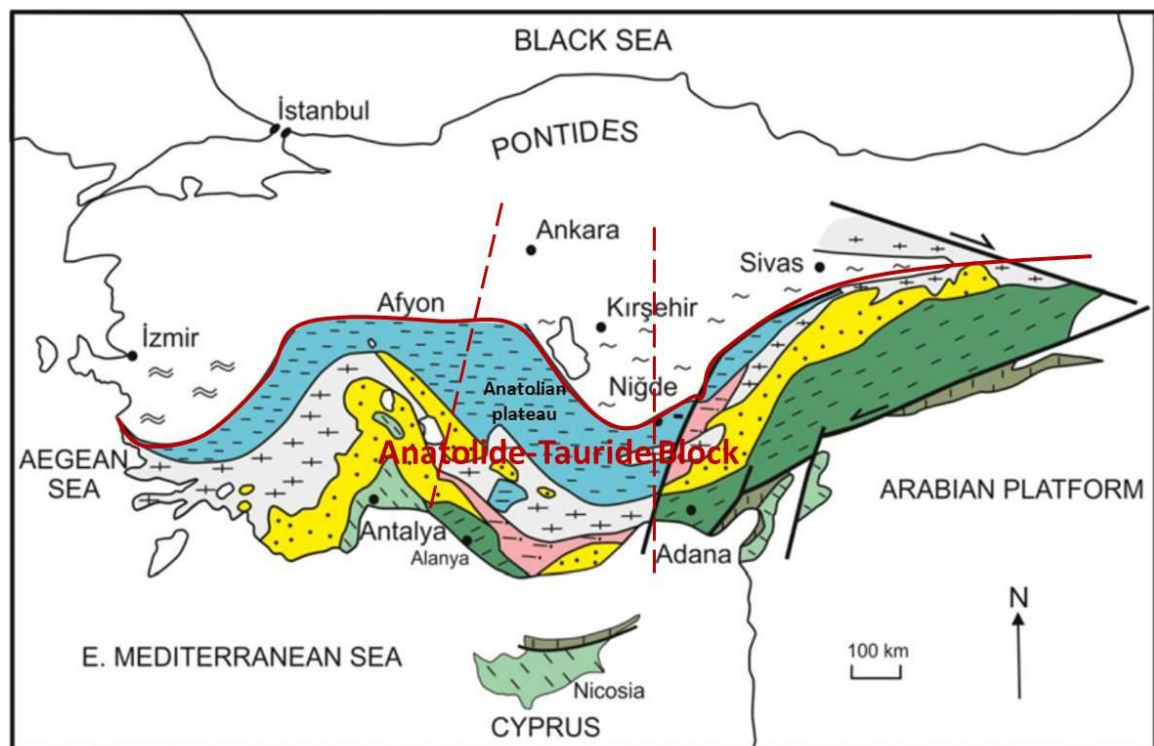
2.2. Geology in the region

The distributions of the main crustal units of southern Turkey and the easternmost Mediterranean region as a whole are nowadays quite well documented (Ketin 1966; Ozgul 1976, 1984a; Figure 2.2). This information forms the basis of all paleogeographical and paleotectonic reconstructions (e.g. Şengör & Yılmaz, 1981; Robertson and Dixon, 1984; Dercourt *et al.*, 1986; Robertson *et al.*, 1991, 2012b; Görür, 1998a, b; Robertson, 2007). Southern and central Turkey is made up of a number of continental blocks covered by carbonate platforms of mainly Mesozoic age. Some of these platforms are separated by outcrops of ophiolites and melanges, or by younger cover (Robertson *et al.*, 2013).

The Anatolide-Tauride (A-T) block shapes the major portion of the southern Turkey. This unit has a Paleozoic stratigraphy like the Arabian platform and Gondwana. There is a solid ophiolite and accretionary complex backlogging over this block. The A-T block can be defined by considering our study area as follows:

- All of the units in a low structural position, in which the sedimentation extends to the Eocene, were correlated as regionally extensive autochthonous continental basement, termed as the Geyik Dağ (Figure 2.2).

- Two units of tectonically transported Mesozoic platform carbonates, one variably metamorphosed (Bolkar Nappe) and the other unmetamorphosed (Aladağ nappe).
- Mainly deeper-water basinal units, exposed to the north of the autochthonous Geyik Dağ, were correlated and named as the Bozkır nappe.
- Metamorphic units in southern and eastern Turkey were correlated as parts of the Alanya nappes (Robertson *et al.*, 2013).



KEY	
<p>≈ Menderes Massif, mainly metamorphic</p> <p>~ Kırşehir Massif, mainly metamorphic</p> <p>+ Bozkır Nappes, slope/basin sediments, rift & oceanic units</p> <p>--- Bolkar Nappe (~Afyon Zone), northerly platform unit</p> <p>--- Aladağ (~Hadim) Nappe, southerly platform unit</p>	<p>••• Geyik Dağ, autochthonous carbonate platform</p> <p>--- Antalya Nappes (~Antalya Complex), slope/basin, rift & oceanic units</p> <p>--- Alanya Nappes, mainly low-to high-grade metamorphic</p> <p>--- Misis Nappes, mainly platform sediments & melange (olistostromes)</p>

Figure 2.2. Previous tectonic classifications of some of the main continental and continental margin units exposed in southern Turkey (modified from Özgül 1984a, b).

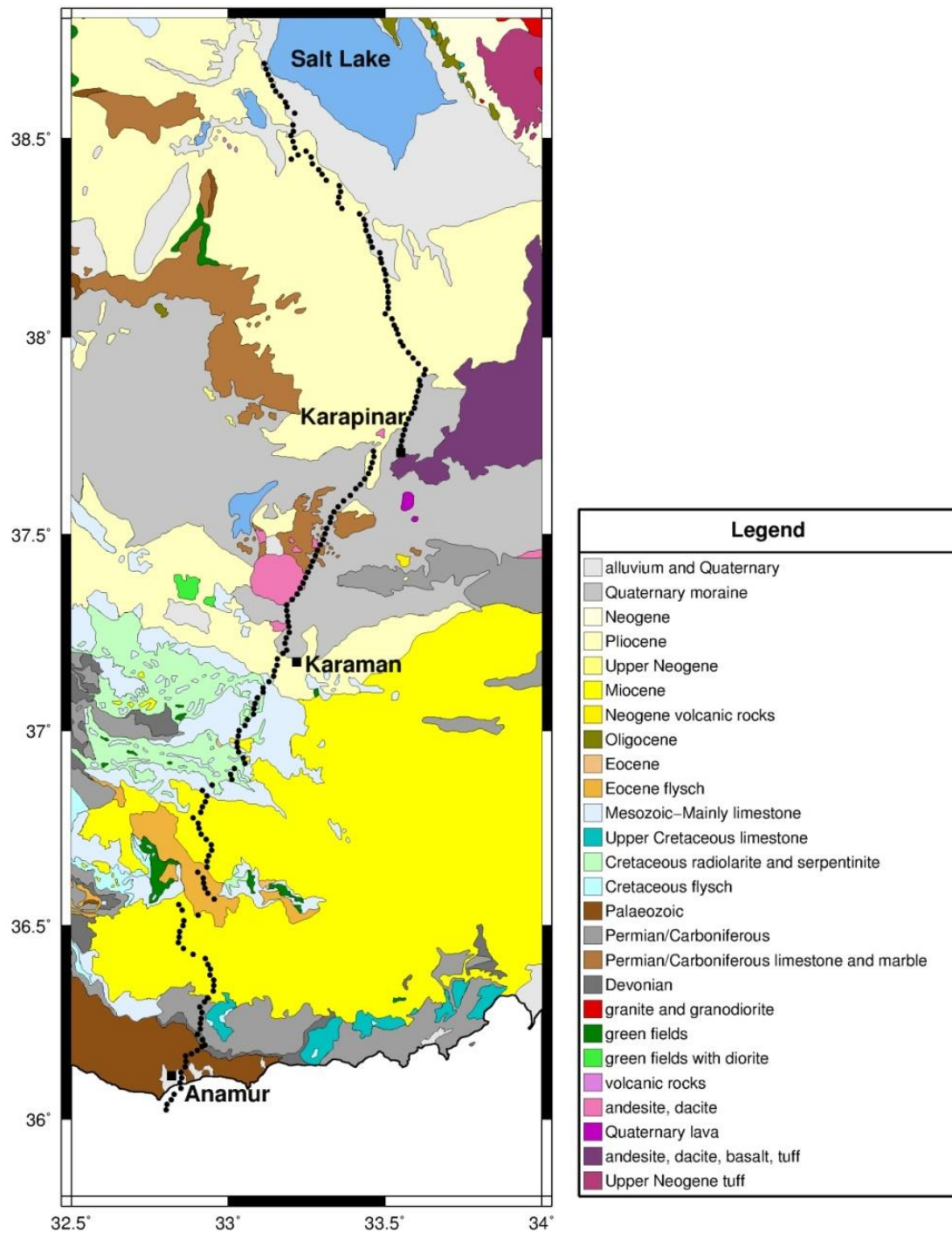


Figure 2.3. Geological map of the Central Anatolia and the Eastern Mediterranean regions along the seismic profile (Geological Map of Turkey, Konya sheet, 1:800000, 1944. Ankara. Black dots show seismic stations along wide-angle reflection/refraction (WRR) profile).

The Central Taurides (our study area) between red dotted lines (Figure 2.2) are cored by the autochthonous Geyik Dağ platform. This unit is overlain, structurally, by the Aladağ, Bolkar and Bozkır nappes (Monod, 1977; Özgül, 1976, 1984a, 1997; Andrew and Robertson, 2002; Mackintosh and Robertson, 2012). These units generally restore as different parts of the Tauride continent and its northern margin. Robertson *et al.* (2013) preferred interpretation is that the Tauride thrust sheets were deposited from a single oceanic basin to the north, presumably the Inner Tauride ocean. This emplacement involved latest Cretaceous and Early-Mid Eocene phases of southward thrusting (Mackintosh and Robertson, 2012). The Eocene event resulted in large-scale out of sequence thrusting (i.e. re-thrusting), which re-organized the initial latest Cretaceous stacking order.

Cilicia basin between Cyprus and south Turkey has distinct mound-shaped structures, stratigraphically. These deposits are tentatively reconciled with the Messinian-bedded pebblestone, sandstone, gypsiferous, and fossiliferous limestone successions (Aksu *et al.*, 2005).

Cyprus island is located on the northeast portion of the eastern Mediterranean with a length of 225 km in the east-west direction (340E-360E) and a width of 95 km in the north-south direction (320N-350N) (Galanopoulos and Delibasis, 1965; Papazachos and Papaioannou, 1999). Cyprus is separated into four geological Terranes: (a) the Keryneia Terrane (b) the Troodos Terrane or Troodos Ophiolite complex (c) the Mamonia Terrane and (d) the Circum Troodos Sedimentary Succession. Our profile crosses Troodos Ophiolite and the Circum Troodos Sedimentary succession (Figure 2.4). The Troodos Terrane or the Troodos Ophiolite complex majorly viewed the central portion of the island and composes the geological core of Cyprus. It was formed in the Upper Cretaceous (90 Ma) on the Tethys sea floor, which then extended from the Pyrenees through the Alps to the Himalayas. It is took an attention as the most complete and studied ophiolite in the world. It is a segment of a fully developed oceanic crust, composing of plutonic, intrusive and volcanic rocks and chemical sediments. The stratigraphic completeness of the ophiolite makes it original. It was composed during the complicated process of sea-floor spreading and formation of oceanic crust and was emerged and settled in its present location through complex tectonic processes associated to the collision of the Eurasian plate to the north and

the African plate to the south. The stratigraphy of the ophiolite indicates a topographic inversion, with the stratigraphically lower suites of rocks outcropping in the highest points of the range, while the higher units appear on the periphery of the ophiolite. This apparent inversion is related to the way the ophiolite was uplifted (diapirically) and later eroded. The uplift of the island took place during episodes of abrupt uplift up to the Pleistocene (2 Ma) (www.moa.gov.cy/Troodos). The Troodos Ophiolite is exceptional for the completeness of the section of oceanic lithosphere. The crust is consisted of sheeted dykes, pillow basalts and marine sediments. The sediments are composed of deep-water shales and radiolarite. The mantle parts of the lithosphere are made of harzburgite and dunite (both peridotites), with about 50 to 80% of the minerals now transformed into serpentinite (Figure 2.4) (www.wikipedia.org). The Troodos Ophiolite has a very important role for the water budget of the island. Most of the rocks, particularly the gabbros and the sheeted dykes are good aquifers due to fracturing. The perennial rivers running radially are feeding the main aquifers in the periphery of the Troodos and the plains (<http://www.moa.gov.cy/Troodos>). The central portion of the ophiolite was uplifted rapidly, presumably due to the upward movement of a deep serpentinite diapir, now exposed at the surface. He adds that the impingement of the Eratosthenes seamount on the Cyprus trench during continuing subduction to the south of the island, was also significant in the upwarping of the Troodos ophiolite (Mackenzie *et al.*, 2006).

The Zone of the autochthonous sedimentary rocks (circum troodos sedimentary cover), ranging in age from the Upper Cretaceous to the Pleistocene (70 Ma to recent), encloses the area between the Keryneia Terrane and Troodos Terrane (Mesaoria) as well as the southern portion of the Cyprus. It composes of bentonitic clays, volcanoclastics, melange, marls, chalks, cherts, limestones, calcarenites, evaporites and clastic sediments (Figure 2.4). Carbonate sedimentation initiates in the Palaeocene (65 Ma) with the deposition of the Lefkara Formation, which comprises pelagic marls and chalks with specified white colour, with or without cherts. The classic development of the Formation is exemplified by four members: Lower Marls, Chalks with layers of chert, solid Chalks and Upper Marls (<http://www.moa.gov.cy/Sediments>).

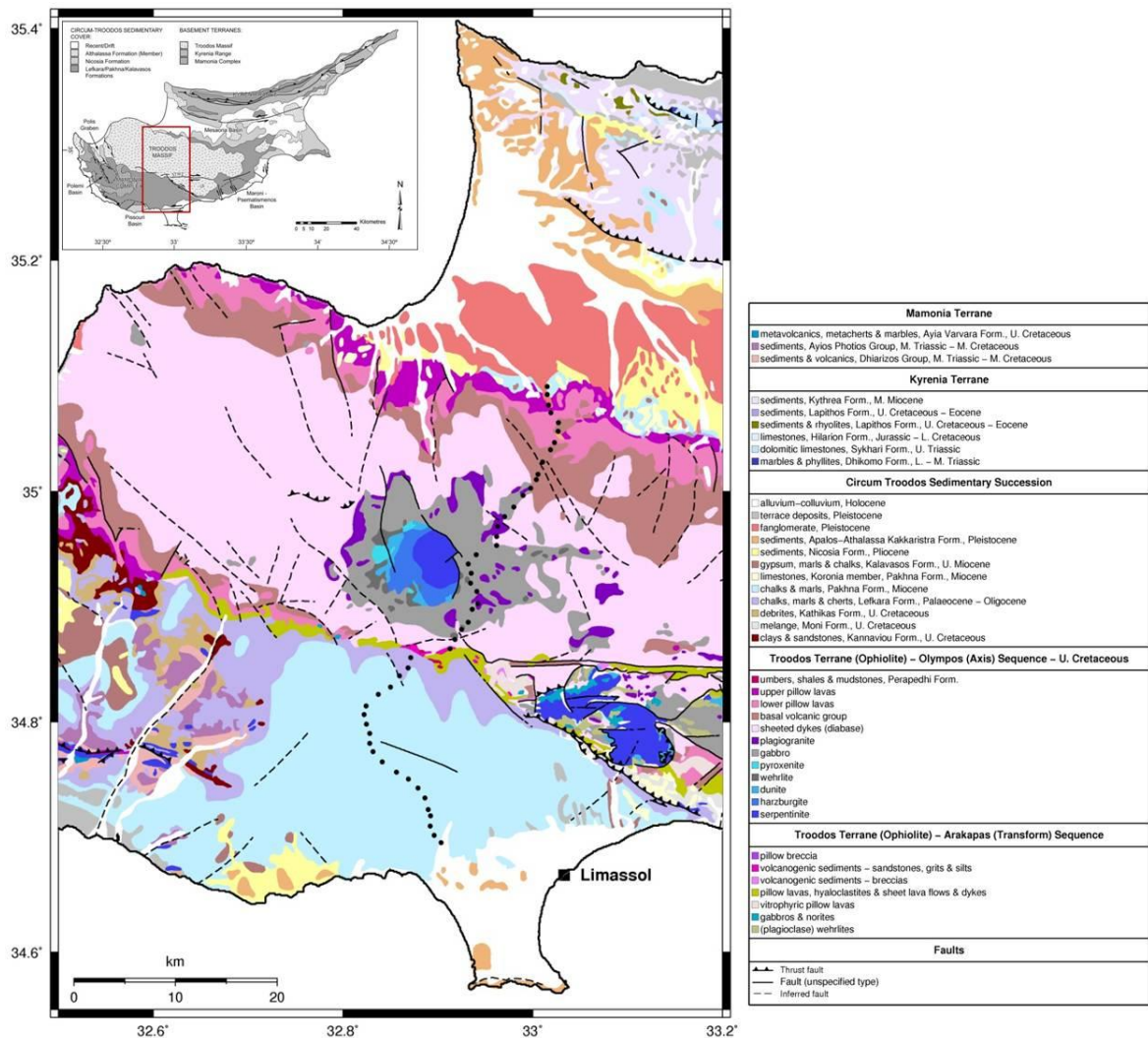


Figure 2.4. Geological map of Cyprus (Geological Map of Cyprus, 1:250000, 1995.

Geological Survey Department, Ministry of Agriculture, Natural Resources and Environment, Government of Cyprus). Black dots show seismic stations along profile. Red triangle show study area (top left, modified from Kinnaird *et al.*, 2011).

2.3. Seismicity in the region

Central Turkey, bounded by the North and East Anatolian strike-slip faults, has a westwards movement from the eastern Anatolia and overrides the eastern Mediterranean at two intermediate seismic domains: one extending between Antalya Bay and southern Cyprus, and the other further west in the Hellenic Trench (Jackson and Mackenzie, 1984). The Tuz gölü fault (Arpat and Şaroğlu, 1975) or Aksaray-Şereflikoçhisar fault (Şengör *et al.*, 1985) is a one of the more prominent active feature in Central Anatolia (Barka and

Reilinger, 1997). According to Yıldırım (2014), in this setting, Central Anatolia is usually defined by normal faults with some strike-slip components (Dhont *et al.*, 1998; Emre *et al.*, 2011; Genç and Yürür, 2010; Özsayın and Dirik, 2007; Şengör *et al.*, 1985; Taymaz *et al.*, 2007, 2007b). Historical (0-1900 A.D.) and instrumental earthquake records show that seismic activity in Central Anatolia has been low relatively to Western Anatolia (Ambraseys, 1970, 1975, 1988; Ambraseys and Finkel, 1987). The 1938 Kırşehir earthquake, $M=6.8$, is the only large earthquake that occurred during this century in this region (Parejas and Pamir, 1939; Ketin, 1969). Especially a noteworthy event is the Kırşehir shock of 1938, which was related with a surface fault break 15 km long indicating approximately 60 cm of right lateral movement trending NW (Arni 1938; Parejas & Pamir 1939; Richter 1958). The 1717 and 1835 Ecemiş earthquakes happened near Kayseri (Öztin and Bayülke, 1990) can be listed as other important events in Central Anatolia (Barka and Reilinger, 1997).

Jackson and McKenzie (1984) observed some earthquakes in Antalya Bay, southern Turkey, have hypocentres actually deeper than 50 km (Jackson 1980b). It was observed that there is a real zone of intermediate depth seismicity dipping north or NE in Antalya Bay (Rotstein and Kafka 1982). Four fault plane solutions (predominantly low-angle thrusts) are determined by Jackson and McKenzie (1984). Within Antalya Bay earthquakes occur at depths of 50–100 km and beneath Antalya itself at >100 km. Fault-plane solutions are unavailable for earthquakes shallower than 50 km. The deep events are correlated with the subducting slab of the Cyprus arc and thus are accounted to be decoupled from the surface neotectonic regime (Glover and Robertson, 1998).

Harrison *et al.* (2004) made a research about the seismicity history of Cyprus and observed that seven strong earthquakes ($M>6.0$) have occurred on or near the since 1900 and presumably at least another 15 devastating earthquakes have affected the island since about 26 BC (Papazachos and Papaioannou, 1999). According to Jackson and McKenzie (1984, 1988), the level of seismicity along the Cyprian Arc is rather low compared with the Hellenic Arc. Luccio and Pasyanos (2007) took the seismicity of the Cyprus when interpreting the crustal and mantle structure beneath Mediterranean region. The seismicity of Cyprus show a dispersed distribution along the arc; the Eastern fragment where shallow and intermediate events (magnitude can be larger than 6) were observed. The western part

includes deep and low magnitude earthquakes. The seismicity of the Hellenic trench has a regular distribution along the arc with hypocentral depths reaching down to 300 km, contrarily. The discrepancy in the seismicity trend along the two arcs demonstrates the different plate motion in the two regions. Subduction is active beneath the whole length of the Hellenic trench whereas the Cyprian arc is undergoing subduction along its north-western margin, collision in the southeastern portion and transcurrence along its Eastern fragment (Wdowinski *et al.*, 2006).

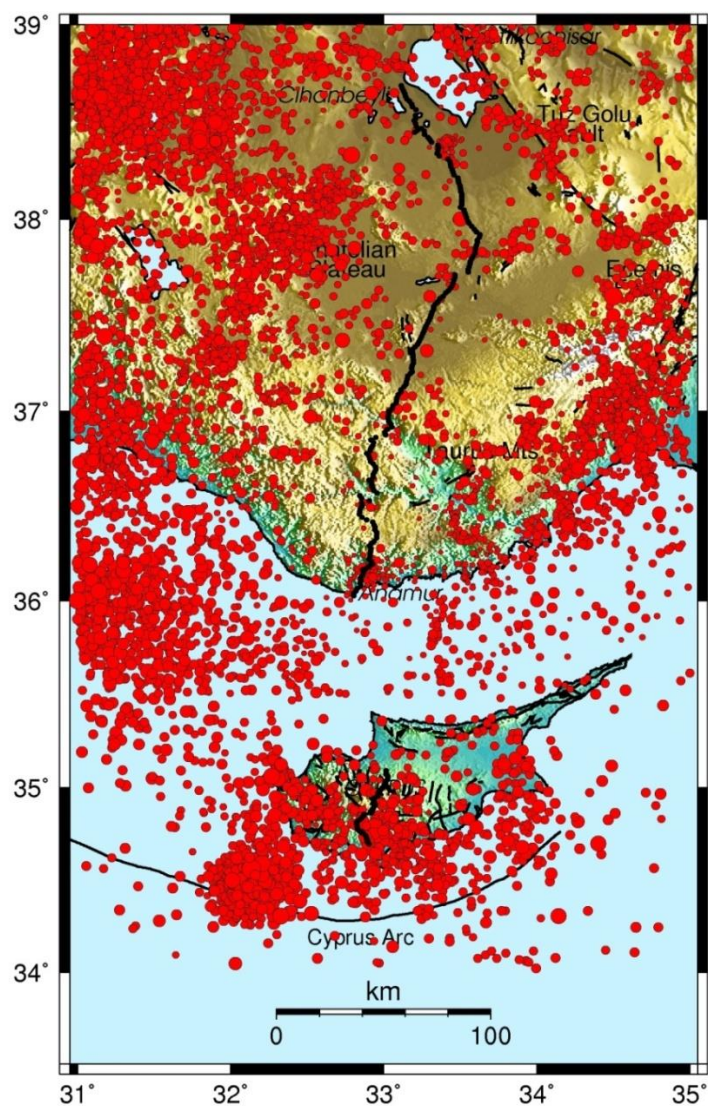


Figure 2.5. Distribution of seismicity for the study area from 1900 to 2015 (KOERI and USGS catalogs). Black dots show seismic stations along wide-angle reflection/refraction (WRR) profile.

Figure 2.5 shows epicenter distribution in the study area. Main clusters are observed along outer border of Isparta angle in west, Antalya bay in southwest, Cyprus arc in south, Tuz Gölü and Ecemiş Faults in east. Epicenter of the shallow earthquakes ($h < 50$ km) are clustered along three major regions, one linear and the other two curved, which describe the northern boundary of the African lithospheric plate in this easternmost portion of the Mediterranean. The linear seismic region is located near the southwest coast of the Cyprus and fault plane solutions were a strike slip fault (Paphos Transform Fault which defines the western boundary of the Cyprean area). The first arcuated zone is close to the southern coast of Cyprus. This zone keeps going to the northeast to join the EAF. It is a compressional region up to southeastern Cyprus at least. The third zone (located northwest of Cyprus) has low seismicity (Papazachos and Papaioannou, 1999).

2.4. Previous studies in the region

The study area is surrounded with tectonically active structures. Northern part of the study area is bounded with the NAF, southwestern part is bounded outer Isparta angle, eastern part is bounded with the EAF and Cyprus arc located southern part of the study area. Many geophysical studies have done in surrounding areas in local and regional scales due to a very high seismic activity level. Such studies are very limited for the study area when compared with geophysical studies in global scale.

The determination of moho thickness has aimed by numerous published papers in which a range of geophysical techniques have been implemented. In 1970, the Turkish Petroleum Company experimented a seismic refraction work on the Tuz Golu (Salt Lake) basin of central Turkey. Gürbüz and Evans (1991) presented their interpretation, using time-term analysis and ray tracing, of data from many shot points along one profile. A P wave velocity was determined as 4.0-4.2 km/s at the sedimentary layer which denotes that the principal sedimentary layer was formed by evaporites. The lowermost layer of the model has a P wave velocity of 6.15 km/s which is correlated with the basement layers being composes of either by Cretaceous metamorphic basement or by lavas of andesitic type. The wide inclusion assured by this data set has enabled the building of a detailed 2-D model which indicates the topography complexity of the subsurface layers. Gürbüz and Evans (1991) defined two main faults and one minor fault impressing both the basement

and overlying layers. The character of these properties and the related layer displacement conducts to speculate that these may be growth faults related to the Aksaray-Sereflikochisar and Karapinar-Cihanbeyli-Haymana hinge compositions which have controlled by the development of the Tuz Golu basin (Gürbüz and Evans, 1991).

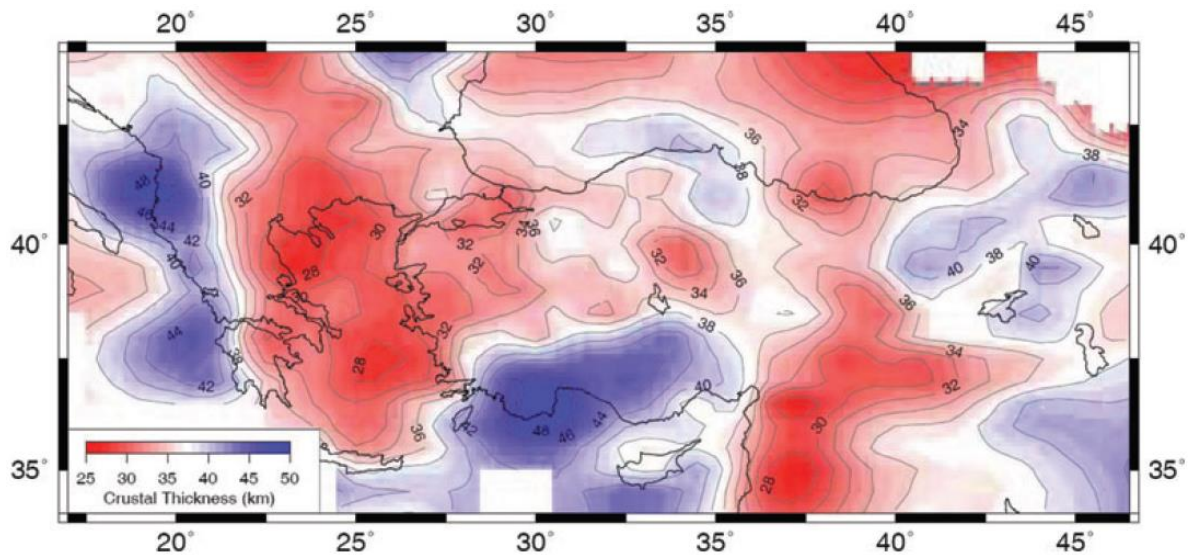


Figure 2.6. Crustal thickness map obtained from station delays (Mutlu and Karabulut, 2011)

A significant study to reveal crustal structure of the Anatolian plate from receiver function method was conducted by Vanacore *et al.* (2013). Crustal thickness in Central Anatolia of about to 37-47 km and a thinned Moho in Cyprus of about to 30 km in this study. Another determination about Moho depth beneath Cyprus was revealed by Mechie *et al.* (2013). Three new maps of crustal thickness under the Arabian plate and margins were revealed. The first map is based on the combined gravity model, EIGEN 06C, which have data from satellite missions and ground-based studies. The second map derived from seismological and ground-based gravity data while the third map is based on just seismological data. All these maps denote relatively anomalously thin continental crust beneath Cyprus. The median value of the crustal thickness is about 30 km (Mechie *et al.*, 2013). Another previous investigations by performing Pn tomography (Gans *et al.*, 2009) and anisotropic Pn tomography (Mutlu and Karabulut, 2011) show crustal thickening from Central Anatolia to Eastern Mediterranean.

Some geologic and tectonic formations like Troodos Massif, Cyprus Arc, Eratosthenes Seamount, Florence rise and Latakia Ridge in Levantine basin make Cyprus concern as a field of study for scientists.

Seismic refraction experiment which was conducted by Makris *et al.* (1983) takes interest in many scientific studies. A long seismic refraction profile was deployed between Cyprus and southern Israel. 33 sea shots each of 0.8 ton blasts were recorded by land stations in Israel and Cyprus by ocean bottom seismographs installed along the profile. The conclusions indicated that Cyprus is underlain by a 35 km thick Moho depth thinning southwards and extending to Eratosthenes Seamount (Makris *et al.*, 1983).

While there have been several seismic studies offshore Cyprus (e.g. Makris *et al.*, 1983; Ben-Avraham *et al.*, 1995), onshore geophysical studies of the Troodos Ophiolite have been primarily relied on gravity experiments. Gass and Masson-Smith (1963) interpreted such applications performed in 1946 and 1958 and suggested a diapirically emplaced serpentine structure to express a localized circular negative anomaly. A detailed gravity investigation of the region was experimented by Shelton (1993). The results were explained in terms of a fully serpentized mantle structure of less than 10 km in diameter reaching to an average depth of 15 km within modified depleted mantle. Shelton (1993) modelled a crustal thickness thinning beneath the southern coast of Cyprus (Mackenzie *et al.*, 2006). The boundary between the African plate and the Aegean/Anatolian microplate is in the process of transition from subduction to collision along the Cyprus Arc. In the west, north of the oceanic Herodotus Basin, subduction may be ongoing; in the east, microcontinental blocks such as the Eratosthenes Seamount are already colliding with Cyprus to the north of the suture. The modifications in crustal composition along and across this convergent zone are not known except by inference from bathymetry, and from a couple of deep-penetrating wide-angle seismic transects on the African plate margin (Ergün *et al.*, 2005). In this contribution Bouger gravity profiles across the Cyprus Arc were modelled by Ergün *et al.* (2005). Models are likely indicating a gravity low over the plate boundary suture with Bouger highs over oceanic or transitional crust and over ophiolites (Ergün *et al.*, 2005).

A noteworthy project which is called IANGASS (Investigations Around North Troodos using Gravity and Seismic Surveys) was performed to reveal the internal composition of the Troodos crust as well as to model the immediate upper mantle by using a combined 160 km seismic wide-angle reflection/refraction and gravity profile located across the sheeted dykes, lavas and sediments of the northern portion of the Troodos ophiolite, Cyprus. The P wave seismic velocity and density model is determined to a depth about to 10 km indicates the ophiolite sequence dipping to the east under the central. The upper layer (average velocity 2.83 km/s; density 2.21 g/cm³) was interpreted as consisting of sediments and the upper extrusive group (Mackenzie *et al.*, 2006).

3. METHODOLOGY

3.1. Forward Modelling

Forward modelling uses a mathematical intercourse, such as the wave equation, to synthesize the earth's response for a given set of model parameters. These parameters would usually imply rock features and the geometry of rock layer interfaces. In the case of seismic modelling, a potential model is the elastic wave equation which uses the parameters of rock density and wave speed to yield a synthetic seismogram as the model response. In geophysical processes, it is very significant to select a forward modelling procedure which will adequately describe the observations. In addition to the selection of a proper mathematical model, it is also crucial to know how many model parameters should be used and which parameters are important. The relevance of modelling selections will depend on the exploration problem at hand and on the geological area of interest (Lines and Newrick, 2004).

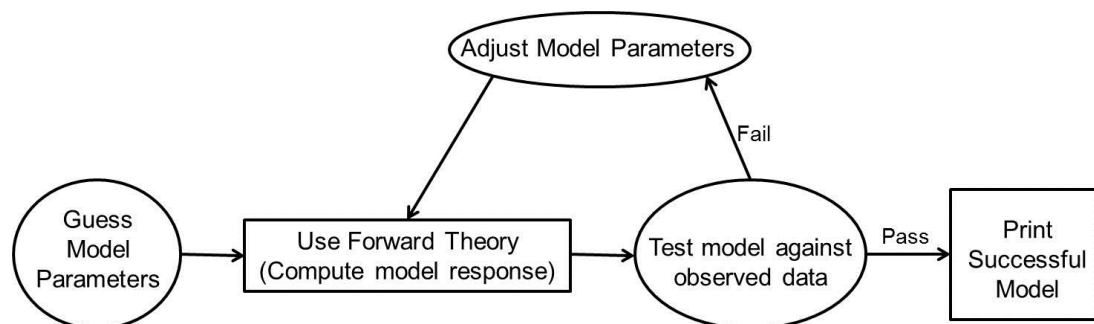


Figure 3.1. Flow diagrams of forward modelling (Sharma, 1997).

3.2. Ray Tracing

The fundamental principles of the ray method have been known for a long time. Ray tracing is depended on the idea that seismic energy of extremely high frequency traces a path identified by the ray tracing equations. Physically, these equations define how energy keeps on the same direction until it is refracted by velocity changes (Vidale, 1988). The

historical development of the ray method is closely linked with the investigation into the nature and behavior of light. In seismological implementations, the ray method used mainly to search the inner structure of the Earth from travel time curves of seismic body waves, and to compute rays and theoretical travel times of seismic waves in various types of media, for final comparison with observed data. The ray theory was first applied to appreciate the amplitudes of seismic body waves propagating in the solid Earth probably by Sir H. Jeffreys during 1920-1930. The ray series solution of the elastodynamic equations of motion was first written by Babich & Alekseyev (1958) and by Karal & Keller (1959) (Cerveny *et al.*, 1977). Another important improvement of the analysis of seismic data was the development of 2-D (two dimensional) ray-tracing schemes (Cerveny *et al.*, 1977). These permitted the forward modelling of seismic travel times for 2-D structures. One of the first applications of these was for experiments conducted over the mid-ocean ridges by McClain and Lewis (1980) (McClain and Caress, 1993).

Ray tracing methods can be classified broadly as either exact or approximate, and the computational strategy involved usually can be categorized as either shooting, bending, approximate, or finite difference. In “shooting” techniques of ray tracing, a fan of rays is shot from one point in the general direction of the other. The accurate path and travel time to link the two points may then be approached with successively more correct estimations. Such results for two and three dimensional bodies were taken out more than 10 years ago (e.g., Julian and Gubbins, 1977 and Cerveny *et al.*, 1977). “Bending” techniques of ray tracing begin with an initial, presumably false prediction for the ray path. The ray path is bent by a perturbation technique until it satisfies a minimum travel time criterion. Complicated conditions in with ray tracing divide into three categories. First, strongly varying velocity fields, there can be numerous paths linking two points of interest. When there are numerous trajectories, it is not difficult to miss the one with minimum travel time. Second, if many travel paths to numerous points are needed, computer costs make the technique unpractical. Third, even in a smooth medium, there may be a shadow zone, where pairs of points will be linked just by rays that have very small geometric amplitude because a small change in the take-off angle results in a large modification in the ray path. Bending techniques of ray tracing do give a respond in shadow zones. However, in both bending and shooting techniques it is feasible that the respond is just a local minimum, and

the global minimum travel time and corresponding ray path remain unknown. Finite-difference is a fast and robust technique to compute a field of travel times. It may be used in many implementations, and has several benefits over ray tracing methods. Arbitrarily complex velocity structure could be used. The first arrival is automatically followed and later, multipathed arrivals are ignored. The method naturally follows diffractions if they are the first arrivals, even through shadow zones (Vidale, 1988).

3.2.1. Calculation of Ray Paths and Travel times for Reflected Phases

Classical ray tracing technique was used to compute the rays and travel times for the reflected phases. The shooting technique was used to specify of source coordinates and take-off angle of the ray.

3.2.1.1. Classical Ray Tracing Technique

Classical ray tracing is a traditional approach is to numerically integrate a set of first order differential ray equations such as proposed Cerveny *et al.* (1977). The basic equation for the computation of rays and travel times is the eikonal equation. For the sake of brevity, the symbol $\vec{\rho}$ is used for the slowness vector with components ρ_1, ρ_2, ρ_3 instead of $\nabla\tau$ (*i. e.*, $\rho_i = \partial\tau/\partial x_i$) where τ represents the point of intersection of the ray with the interface . Then the eikonal equation reads

$$\rho_i \rho_i = v^{-2} \quad (3.1)$$

As the eikonal equations are essentially the same for both P and S waves, the resulting formula will apply to both P waves (with $v = \alpha$) and S waves (with $v = \beta$). The characteristics of the eikonal equation are specified by the system of six ordinary differential equations of the first order,

$$\frac{dx_i}{d\tau} = v^2 \rho_i, \quad (3.2)$$

$$\frac{d\rho_i}{d\tau} = -\frac{\partial \ln v}{\partial x_i},$$

$$i = 1,2,3.$$

If we determine a chosen ray by its initial values for

$$\begin{aligned} \tau &= \tau_0, \\ x_i &= (x_i)_0, \\ \rho_i &= (\rho_i)_0, \\ i &= 1,2,3. \end{aligned} \tag{3.3}$$

We can calculate the coordinates of points along the ray ($x_i = x_i(\tau)$) and the components of the slowness vector along the ray ($\rho_i = \rho_i(\tau)$). The initial values $(p_i)_0$ as well as the values of ρ_i along the ray are not arbitrary. They must satisfy the eikonal equation (3.1) at corresponding points $(x_i)_0$ resp. $x_i(\tau)$. It may be advantageous to write equations (3.2) in an alternative form. The direction of the ray can be specified, e.g. by the polar angles φ and δ ($0 \leq \varphi \leq 2\pi$ and $0 < \delta < \pi$), such as

$$\begin{aligned} \rho_1 &= v^{-1} \cos \varphi \sin \delta, \\ \rho_2 &= v^{-1} \sin \varphi \sin \delta, \\ \rho_3 &= v^{-1} \cos \delta \end{aligned} \tag{3.4}$$

The eikonal equation (3.1) is then automatically satisfied and the ray tracing system reads

$$\begin{aligned}
dx_1/d\tau &= v \cos \varphi \sin \delta \\
dx_2/d\tau &= v \sin \varphi \sin \delta \\
dx_3/d\tau &= v \cos \delta
\end{aligned} \tag{3.5}$$

$$d\varphi/d\tau = (v_1 \sin \varphi - v_2 \cos \varphi) / \sin \delta$$

$$d\delta/d\tau = -(v_1 \cos \varphi + v_2 \sin \varphi) \cos \delta / v_3 \sin \delta$$

where $v_1 = \partial v / \partial x_1$. We can see that the ray tracing system (3.5) consists of five equations of the first order. The initial conditions for the system (3.5) are very simple for

$$\begin{aligned}
\tau &= \tau_0, \\
x_i &= (x_i)_0, \\
\varphi &= \varphi_0, \\
\delta &= \delta_0
\end{aligned} \tag{3.6}$$

The values of $(x_i)_0$ specify the initial point of the ray, φ_0 and δ_0 the initial direction of the ray at $(x_i)_0$.

The number of equations in the ray tracing system can be decreased when v depends on two coordinates only, say x and z (the notation x, y, z (instead of x_1, x_2, x_3) is used), $v = v(x, z)$. For initial conditions such that $y_0 = \text{const}$ and $(\rho_2)_0 = 0$ or $\varphi_0 = 0$, we have $y = y_0 = \text{const}$ and $\rho_2 = (\rho_2)_0 = 0$ or $\varphi = \varphi_0 = 0$ along the whole ray. The ray tracing system (3.5) is reduced to three equations

$$\begin{aligned}\frac{dx}{d\tau} &= v \sin \delta \\ \frac{dz}{d\tau} &= v \cos \delta \\ \frac{d\delta}{d\tau} &= -v_x \cos \delta + v_z \sin \delta\end{aligned}\tag{3.7}$$

where $v_x = \partial x / \partial \tau$, $v_z = \partial v / \partial z$, $-\pi \ll \delta \ll \pi$. The initial conditions are as follows:

$$\begin{aligned}\tau &= \tau_0, \\ x &= x_0, \\ z &= z_0, \\ \delta &= \delta_0\end{aligned}\tag{3.8}$$

There is no singularity connected with $\delta = 0$ and $\delta = \pm\pi$ in this system. Ray tracing system (3.7) decreased by one when we use any of the spatial coordinates as a new integration variable instead of τ . System (3.7) consisting of three equations can be written in a simpler form

$$\begin{aligned}\frac{dx}{dz} &= \tan \delta, \\ \frac{d\delta}{dz} &= -v^{-1}(v_x - v_z \tan \delta)\end{aligned}\tag{3.9}$$

where $v_x = \partial v / \partial x$ and $v_z = \partial v / \partial z$. The travel time τ along the ray can be easily determined by numerical integration along the ray. The system is very convenient for ray tracing when the prevailing direction of rays is along the z axis (e.g., in the reflection prospecting). The system cannot be used when the ray is parallel to x axis, as then $\delta \rightarrow \infty$. Generally, for rays with prevailing direction along the x axis the error of computation may be high. It is, however, possible to replace the integration variable z by x in this case. Then we have

$$\begin{aligned}\frac{dz}{dx} &= \cot \delta, \\ \frac{d\delta}{dx} &= -v^{-1}(v_x \cot \delta - v_z)\end{aligned}\tag{3.10}$$

Thus, during the computation of the ray using (3.9) and (3.10) we must check the direction of the ray with respect to the x and z axis and use the proper system at any particular point. Numerical solutions for the system of ordinary differential equations of the first order (3.7) with the initial conditions (3.8), Runge-Kutta method is used (Cerveny *et al.*, 1977).

3.2.1.2. Shooting Method

By nature, ray tracing is two-point boundary value problem (BVP): the end points are specified (the source and receiver positions), and the propagation path and time must be specified. Shooting methods solve the two point BVP by iteratively solving initial value problem with one fixed end point and the initial ray trajectory varied (Thurber, 1993). The shooting method has been successfully used mainly in 2-D models, in situations in which we need to find rays shot from a point source to a series of receivers distributed regularly or irregularly in some region along the surface of the Earth. We start shooting rays that hit the Earth's surface outside the region with receivers. We then regularly vary the take-off angle to come closer to the receiver region. As soon as we overshoot a receiver, we return and determine the ray passing through the point using standard numerical interpolation techniques (Cerveny, 2001).

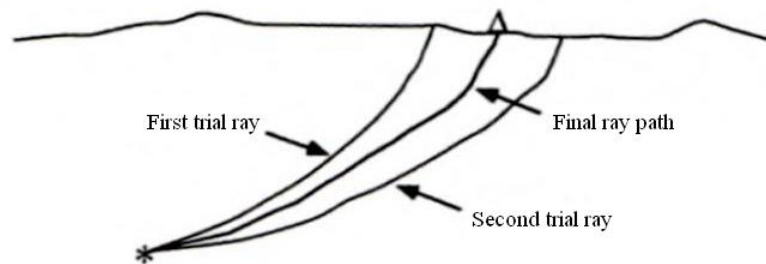


Figure 3.2. Schematic representation of shooting approach. The trajectory of the initial ray at the source is perturbed until the receiver is reached (Thurber, 1993).

3.2.2. Calculation of Ray Paths and Travel times for Refracted Phases

The original opinion was to get travel times by calculating the eikonal equation using finite difference methods, as first defined by Reshef & Kosloff (1986), and extended by Vidale (1988,1990) in 2-D and 3-D models for any source point in the medium. New finite difference schemes were also suggested to increase robustness (Van Trier & Symes 1991, Podvin & Lecomte, 1991 and Schneider *et al.*, 1992) because the pure finite difference approaches fail in contrasted velocity field with first-order discontinuities of arbitrary shapes (Lecomte, 1993).

Vidale (1988) has presented a similar travel time computation approach, except he implemented a finite-difference solution to the eikonal equation. He described an algorithm that models plane waves and one that models circular wavefronts. Unfortunately, the more accurate circular wavefront method can become unstable. His mapping scheme computes travel times on concentrically expanding squares about the source location, where times are mapped to the outermost square in a model-dependent order. This special ordering ensures that causality is usually not violated; however, it also makes the code nonvectorizable (Schneider *et al.*, 1992). Van Trier & Symes (1991) and Podvin & Lecomte (1991) modified Vidale's algorithm, also using a finite-difference solution to the eikonal equation.

Van Trier & Symes' approach avoids the model dependent mapping order, which allows it to fully vectorize at the cost of less certainty, thus making it the most efficient travel time computation scheme. However, their algorithm is only stable for smooth velocity distributions (Schneider *et al.*, 1992). Podvin & Lecomte (1991) suggested method which depends on a systematic implementation of Huygens' Principle in the finite-difference approximation. Local discontinuities of the time gradient in the first arrival time field are constructed as intersections of locally free wavefronts. A plain finite difference approximation of the eikonal equation implicitly occurs in mathematically propagating a single wavefront in the model, whereas a few locally independent wavefronts may in fact reach any point. As a result, the algorithm silently combines information related to these wavefronts, which may cause to mathematically contradictory conditions. For this reason, the suggested algorithm is not, as Vidale's method, a basic finite difference approximation

of the eikonal equation in the sense that multiple arrivals at any point are steadily considered. A first arrival criterion is then used for picking the first one. An important improvement is supplied by the suggested technique, in comparison with Vidale's approach, i.e., accurateness with respect to very sharp velocity contrasts is warranted (Podvin and Lecomte, 1991). Alternatively, a 2-D dynamic programming technique was suggested by Schneider *et al* (1992). The method, depend on Fermat's principle, uses basic calculus methods and a systematic mapping scheme to define first-arrival times on a uniform grid, given an arbitrary, discrete velocity distribution. First arrival seismic energy can propagate either as transmitted waves, diffracted waves, or headwaves and this technique models all types. The travel time calculations begin with starting values computed near the source location. Then, mapping systematically steps through the grid, where each new arrival time is calculated using two previously calculated "neighbor" travel times. Schneider *et al* (1992) presented mapping procedure, a brute force approach that advances across the grid one column at a time and a more natural approach that calculates times along expanding rectangles. In this finite-difference type, a brute force mapping approach was preferred and this approach uses a model-independent mapping order. This algorithm is easy to code, and it accurately handles all difficulties but the most complicated velocity models (Schneider *et al.*, 1992).

The finite-difference ray tracing based on the eikonal equation was used for refracted phases. The travel time field in the medium is calculated first based on the source coordinates. Then the ray path is calculated by back-tracking from the receiver to the source along the path of the steepest gradient in the travel time field. Travel times were calculated by using Schneider *et al.*'s approach (1992), the brute force mapping. As suggested by Vidale (1988) and Moser (1989), rays may be 'backtracked' from any grid-point (receiver) to the source, with the operate of the time field obtained by finite-difference. The ray connecting a given receiver to the source is the steepest path that may be found in the time field between these two points. Starting from the receiver, the ray is iteratively traced with increments opposite to the time gradient. For any point reached by the ray, the local time gradient is appraised by a simple finite-difference scheme at the closest grid-point or, if closer, at the centre of the mesh (Podvin and Lecomte, 1991).

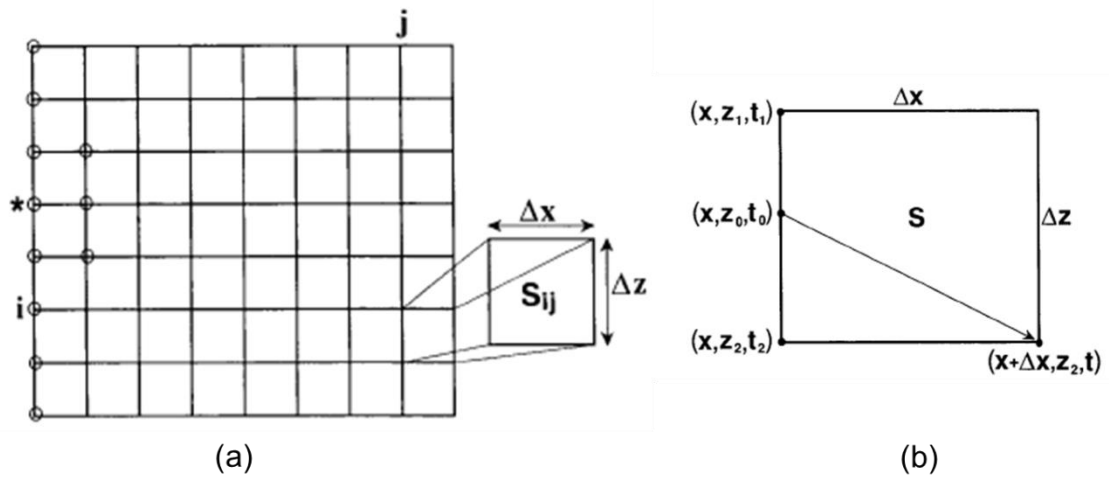


Figure 3.3 (a). Grid layout for the brute force mapping approach. The star denotes the source location. (b). One constant slowness grid cell with minimum time raypath impinging upon the node where t is to be computed (Schneider *et al.*, 1992).

Initially, since slowness (the inverse of velocity) is constant in each cell, straight ray path travel times are computed to all nodes on the left edge of the grid and to three nodes in the second column of the grid that are nearest neighbors to the source location. These special nodes are circled in Figure 3.3 (a). The source node receives an arrival time of zero, and the node directly above the source node receives arrival time $S \cdot \Delta z$, where S is the slowness of the cell between these two nodes. Direct arrival times are analogously computed to the rest of the circled nodes. A calculation scheme based upon Figure 3.3 (b) will not compute the first arrival time t if $t_1 > t_2$ simply because the straight raypath segment shown in the Figure 3.3 (b) could not be orthogonal to any physical wavefront (for isotropic media). The brute force mapping procedure described next uses several possible arrangements of t_1 and t_2 to compute several possible t values for each grid node. It does not check as to whether $t_1 > t_2$ (for efficiency reasons); however, the smallest t is always retained at each grid node, thus ensuring that true first arrivals are mapped. The mapping order also proceeds in a manner that prevents causality from being violated (Schneider *et al.*, 1992).

The mapping begins in the top-left corner of the grid, where some t_1 and t_2 are known (starting values). They are used to compute a time t , using the configuration shown (Figure 3.4 (a) shows that this t is not minimum time for this particular source location.

The mapping will soon correctly place the minimum time at this node). The configuration is then moved down one cell. This process repeats until the bottom of the grid is reached. Then t_1 and t_2 are reconfigured as shown in the bottom-left corner of Figure 3.4 (a). Now, a new t is computed using illustrated configuration and this time is compared to the previously computed value. The smallest time is retained for that grid node. The configuration slides up the grid, repeating this process until it reaches the top. Two runs have now been made through the second column of the time grid. Two more will be similarly performed, and their reconfigured as shown in the bottom-left corner of Figure 3.4 (a). Now, a new t is computed using illustrated configuration and this time is compared to the previously computed value. The smallest time is retained for that grid node. The configuration slides up the grid, repeating this process until it reaches the top. Two runs have now been made through the second column of the time grid. Two more will be similarly performed, and their reconfigured as shown in the bottom-left corner of Figure 3.4 (a).

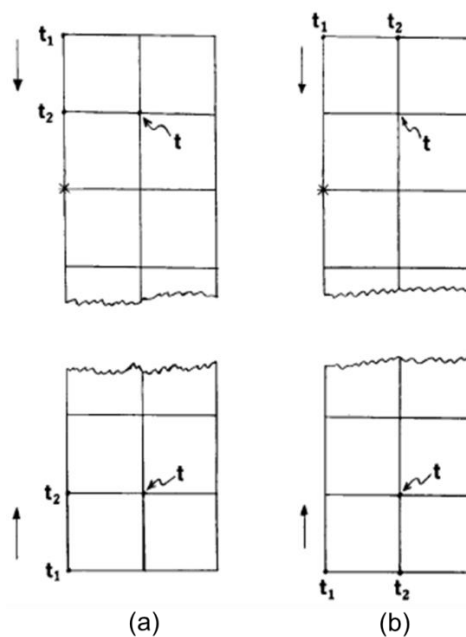


Figure 3.4. The three left-most columns of the grid are shown in (a) and repeated again in (b). The centers of the columns have been “cut away” for clarity. The four configuration types that are used to compute a new time t , on column 2, from a pair of known times t_1 and t_2 , on columns 1 and 2 are illustrated. A star denotes the source point (Schneider *et al.*, 1992).

Now, a new t is computed using illustrated configuration and this time is compared to the previously computed value. The smallest time is retained for that grid node. The configuration slides up the grid, repeating this process until it reaches the top. Two runs have now been made through the second column of the time grid. Two more will be similarly performed, and their configurations are shown in Figure 3.4 (b), which represents the same piece of grid illustrated in Figure 3.4 (a) (Figure 3.3 (b) applies to these configurations after interchanging all x and z variables). Again, minimum times are retained in all comparisons. A special case is also handled during each of the four runs illustrated in Figure 3.4. The configurations shown in Figure 3.4 (b) will be used to describe it, although an analogous case is also handled for those of Figure 3.4 (a). Let the cell bounded by t_1 , t_2 , and t have slowness S , and the cell directly to the right of this cell have slowness S_r . If $S_r < S$, then $t = t_2 + S_r \cdot \Delta z$ could be the true minimum time (This corresponds to a true minimum time raypath that travels along the boundary of the two cells). After completing the four runs through the second column and their special cases, the procedure steps to the right one column, and the times on column two are considered known. Times on the third column are similarly computed, and the procedure repeats until times have been mapped to the right edge of the grid. The configuration illustrated in Figure 3.4 (a) produce travel times for those ray paths that are more nearly vertical. This is because the true first arrival ray path, which travels from the source to the node where t is defined, must pass between the nodes defining t_1 and t_2 for any calculation to give a true minimum time. The procedure just described, which moves across the grid away from the source location, maps travel times onto the grid that correspond to a disturbance expanding outward from a point source. This will be called the forward pass. The travel time field after the forward pass has the property $\nabla_x t \geq 0$ (the x -component of the travel time gradient is directed away from the source point). Wavefronts with raypaths that have turned back toward the left edge of the grid (such as diffracted events and headwaves) are not computed by the forward pass. Travel times corresponding to turned rays would have the property $\nabla_x t < 0$. These times are determined from the forward pass results by subsequently running a reverse pass through the grid. It uses the times computed at the right edge of the grid as starting values, and it moves from right to left, using the four configuration types of Figure 3.4 and the special cases, analogously to the way that the forward pass uses them. The reverse pass only alters times in the grid to map first arrivals corresponding to wavefronts that move in a general direction that is toward the source

location. Thus, the two pass algorithm is capable of determining first arrivals for slowness distributions where raypaths turn a full 180° within the grid (the two passes together allow $\nabla_x t$ to change sign once, from positive to negative, along any ray conceptual raypath). Additional passes would allow the algorithm to determine travel time fields for more complicated slowness distributions. This completes the mapping procedures (Schneider *et al.*, 1992). For travel time calculation, nonlinear interpolation scheme, which is based on modelling curved wavefronts, was used with the brute force mapping procedure (Schneider *et al.*, 1992).

Referencing Figure 3.3 (b), a local plane wave assumption is that travel time changes linearly with distance in any direction. Thus, the linear interpolation in z_0 is written,

$$t_0 = \left[(t_2 - t_1) / \Delta z \right] \cdot (z_0 - z_1) + t_1 \quad (3.11)$$

The first arrival travel time t at $(x + \Delta x, z_2)$ is then obtained by minimizing

$$t = t_0 + S \cdot [(z_2 - z_0)^2 + \Delta x^2]^{1/2} \quad (3.12)$$

with respect to z_0 . Consider a 2-D medium with a uniform slowness, which implies that wavefronts generated by a point source are circular. Let z refer to depth and x_a refer to lateral distance from a point source. Then,

$$t^2 = S_a^2 \cdot (x_a^2 + z^2) \quad (3.13)$$

is the time-distance relationship. If x_a is held constant, then t^2 behaves linearly with respect to z^2 . Let t_1 and t_2 be known travel times at points (x_a, z_1) and (x_a, z_2) , respectively. These two points define a line that parallels the z -axis. Equation 3.13 can be written for each of these two points, and then two outcomes can be extracted yielding

$$W = (t_2^2 - t_1^2) / (z_2^2 - z_1^2) = S_a^2 \quad (3.14)$$

using a simple linear interpolation formula in squared quantities, the travel time t_0 at any point (x_a, z_0) along this line satisfies

$$t_0^2 = W(z_0^2 - z_1^2) + t_1^2 \quad (3.15)$$

Since the calculation is performed along a line that parallels the z -axis, the lateral distance x_a is not referenced in the calculation, hence it is implied. When the medium slowness is variable equation 3.15 becomes an interpolation formula that is nonlinear in the unsquared distance z_0 . For example, let a real point source be placed at $x = z = 0$ within a variable velocity medium, and let t_1 and t_2 be known arrival times recorded at (x, z_1) and (x, z_2) , respectively. These data generate an “apparent” slowness value S_a as given by equation (3.14). This can then be used in equation (3.15) to estimate a t_0 value at (x, z_0) , for z_0 lying between z_1 and z_2 . This z_0, t_0 pair implies, through equation (3.13), that $t_0^2 = S_a^2 \cdot (x_a^2 + z_0^2)$. Thus, the lateral position of the “apparent” point source differs from that of the real point source by distance $x - x_a$. This ensures that circular wavefronts from a best fit constant slowness “experiment” interpolate the known times at (x, z_1) and (x, z_2) . Consider a special case, where $t_2 = t_1$ and $z_2 > z_1 > 0$, which implies that locally, the wavefronts are vertical. Equation (3.14) says that $W = 0$ and equation (3.13) implies that $x_a \rightarrow \infty$. Circular wavefronts from an apparent source at $x_a = \infty$ are vertical and equation (3.15) correctly gives $t_0 = t_1$. Referencing Figure 3.3 (b), consider x, z_1, z_2, t_1 and t_2 to be known, and the coordinate system origin will coincide with the real point source location (star on Figure 3.3 (a)). With equation (3.15) providing the $t_0(z_0)$ interpolation, equation (3.12) is minimized to obtain the minimum arrival time t in a medium where wavefronts are curved. Differentiating with respect to z_0 gives

$$dt/dz_0 = z_0 W / t_0 - S \cdot (z_2 - z_0) \cdot [(z_2 - z_1)^2 + \Delta x^2]^{-\frac{1}{2}} \quad (3.16)$$

The minimization problem of $dt/dz_0 = 0$ easily reduces to Snell's law at the grid cell boundary. Conceptually, the raypath from the apparent source location, through the apparent slowness medium, bends at cell boundary and then travels to the corner when t is defined (see Figure 3.3(b)). When t_1 and t_2 represent true constant slowness arrival times, then S_a , as calculated from equation (3.14), is the true slowness, and the minimization problem is exact. Otherwise S_a is a best fit apparent slowness, and the minimization problem is locally accurate (on grid cell scales). Thus, the nonlinear interpolation scheme is used to perform a more precise brute force mapping (Schneider *et al.*, 1992).

3.3. Synthetic Seismograms: A Finite-Difference Approach

The synthetic seismogram has seen many years of extensive and accomplished implementation in geophysical exploration. It found early use as a means to simulate the normal incidence reflectivity of a horizontally stratified medium and has been employed more recently to get the responses of subsurface structural and stratigraphic configurations (geologic models) of ever-increasing complexity (Kelly *et al.*, 1976), and also it found many applications in the interpretation of seismic data, especially in the researches of the structure of the Earth's crust and the uppermost mantle. It is basic to compare them with observed seismograms; they clearly verify the differences between the real model of the medium and the theoretical model used for the computation. Synthetic seismograms can be used to improve successively the model of medium. Their greatest advantage consists in giving a proper description of various interference wave effects. It is often complicated to investigate seismic body waves of the interference character (formed by the superposition of many elementary waves corresponding to various rays) in complex media by other methods. Synthetic seismograms are very suitable for this purpose (Cerveny *et al.*, 1977).

Among the many methods available for this aim, the technique of finite differences is especially changeable. The 2-D partial differential equations of motion defining the propagation stress waves in an elastic medium are approximated by proper finite-difference equations, which can be solved on a discrete spatial grid by strictly numerical procedures. Since the finite-difference scheme is relied on the elastic wave equation without physical assumptions, the technique accounts not merely for direct waves, primary reflected waves, and multiply reflected waves, but also for surface waves, head waves,

converted reflected waves, diffracted waves, critically refracted waves, and waves observed in ray theoretical shadow zones (Kelly *et al.*, 1977).

For stability condition, a physically meaningful numerical computation requires that the finite-difference algorithm be stable, i.e., the difference between the precise and the numerical solutions of a finite-difference equation must remain bounded by time increment (Δt). Alterman and Loewenthal (1970) have shown that the system of equations is stable provided that

$$\Delta x \leq \frac{\alpha}{f_d} / 10 \text{ or } 15$$

$$\Delta t \leq \Delta x / \sqrt{\alpha^2 + \beta^2} \quad (3.17)$$

f_d : Dominant frequency

which indicates that the time increment (Δt) cannot be selected arbitrarily but rather must obey a constraint imposed by the choice of a distance increment (grid interval) (Δx) as well as the values of the P and S wave velocities (α and β , respectively) in the layer (Kelly *et al.*, 1976).

Various finite-difference schemes in use for producing synthetic seismograms generate unwanted reflections from the edges of the model. Transparent boundary condition, which greatly reduce edge reflection, was developed by Reynolds (1978). In 2-D case, the normal factorization of the differential operator,

$$\frac{1}{c^2} \frac{\partial}{\partial t^2} - \frac{\partial^2}{\partial x^2} - \frac{\partial^2}{\partial z^2} = \left[\frac{1}{c} \frac{\partial}{\partial t} - \left(\frac{\partial^2}{\partial x^2} + \frac{\partial^2}{\partial x^2} \right)^{1/2} \right] \cdot \left[\frac{1}{c} \frac{\partial}{\partial t} - \left(\frac{\partial^2}{\partial x^2} + \frac{\partial^2}{\partial z^2} \right)^{1/2} \right] \quad (3.18)$$

If $L_1 = \frac{\partial}{\partial x} \left(I + \left(\frac{\partial}{\partial x^2} + \frac{\partial}{\partial x^2} \right) \right)^{1/2} = \left(\frac{\partial^2}{\partial x^2} + \frac{\partial^2}{\partial z^2} \right)^{1/2}$ where I is the identity operator, then (3.18) can be written as

$$\frac{1}{c^2} \frac{\partial}{\partial t^2} - \frac{\partial^2}{\partial x^2} - \frac{\partial^2}{\partial z^2} = \left[\frac{1}{c} \frac{\partial}{\partial t} - L_1 \right] \cdot \left[\frac{1}{c} \frac{\partial}{\partial t} + L_1 \right] \quad (3.19)$$

L_1 was defined as the set of all functions represented by plane waves or sums of plane waves as follows. If $u = e^{i(\omega t \pm kx \cos \theta \pm kz \sin \theta)}$ then $L_1 u$ was defined by

$$L_1 = \pm ik \cos \theta [1 + (\sin^2 \theta / \cos^2 \theta)]^{1/2} u = iku \quad (3.20)$$

The factorization (3.19) suggests the boundary conditions

$$\left(\frac{1}{c} \frac{\partial}{\partial t} - \frac{\partial}{\partial x} L_1 \right) u = 0, x = -a \quad (3.21)$$

$$\left(\frac{1}{c} \frac{\partial}{\partial t} - \frac{\partial}{\partial x} L_1 \right) u = 0, x = a \quad (3.22)$$

Although the boundary conditions (3.21) and (3.22) yield a reflection coefficient of zero for all incidence angles θ , these conditions depend explicitly on the wavenumber (k) and cannot be applied in practice. If f is defined by $f(k_z) = \sqrt{1 + (k_z^2/k_x^2)}$, the Maclaurin series expansion of f through second derivative terms gives $f(k_z) = 1 + \frac{1}{2} (k_z^2/k_x^2)$, which suggests that (3.21) and (3.22) was replaced by

$$\left[\frac{1}{c} \frac{\partial}{\partial t} \pm \frac{\partial}{\partial x} \left(1 + \frac{1}{2} \frac{\partial^2}{\partial z^2} / \frac{\partial^2}{\partial x^2} \right) \right] \cdot u = 0 \quad (3.23)$$

or the operator $\partial/\partial x$ was applied to (3.23), the boundary conditions

$$\frac{\partial}{\partial x} \left(\frac{1}{c} \frac{\partial u}{\partial t} \right) - \frac{\partial^2 u}{\partial x^2} - \frac{1}{2} \frac{\partial^2 u}{\partial z^2} = 0, x = -a \quad (3.24)$$

and

$$\frac{\partial}{\partial x} \left(\frac{1}{c} \frac{\partial u}{\partial t} \right) - \frac{\partial^2 u}{\partial x^2} + \frac{1}{2} \frac{\partial^2 u}{\partial z^2} = 0, x = a \quad (3.25)$$

obtained. The boundary conditions (3.24) and (3.25) yield low reflection coefficients. Moreover, a boundary condition, which yields on the average lower reflection coefficients than boundary conditions (3.24) and (3.25), is derived. Note that (3.25) is equivalent to

$$\frac{1}{c} \frac{\partial^2 u}{\partial x \partial t} + \frac{\partial^2 u}{\partial x^2} + \left(\frac{p}{1+p} \right) \frac{\partial^2 u}{\partial x^2} = 0 \quad (3.26)$$

The boundary condition (3.26) is easier to implement in an explicit, finite-difference program if the $\partial^2 u / \partial z^2$ term is transformed. In 2-D case, the acoustic wave equation is given by

$$\frac{\partial^2 u}{\partial z^2} = \frac{1}{c^2} \frac{\partial^2 u}{\partial t^2} - \frac{\partial^2 u}{\partial x^2} \quad (3.27)$$

Substituting (3.27) into (3.26) and multiplying the result by $1 + p$ gives

$$\frac{1}{c} \frac{\partial^2 u}{\partial x \partial t} + \frac{\partial^2 u}{\partial x^2} + p \left(\frac{1}{c} \frac{\partial^2 u}{\partial x \partial t} + \frac{1}{c^2} \frac{\partial^2 u}{\partial x \partial t} \right) = 0, x = a \quad (3.28)$$

when interfaces become inclined or otherwise more geometrically complex, it becomes increasingly difficult to cope with the associated boundary conditions. This difficulty can be overcome by developing a finite-difference scheme for general heterogeneous wave equation, which allows for spatial variations in the material properties. This approach makes it feasible to associate different density and elastic parameter values with every grid point. Such a formulation provides the flexibility required to simulate a variety of complex subsurface geometries. This scheme was applied by Boore (1972) to a scalar SH-wave propagation problem. The present treatment deals with a coupled, vector wave appropriate to P-SV wave propagation in a heterogeneous elastic medium. In more general formulation, the Lamé parameters $\lambda(x, z)$ and $\mu(x, z)$ need no longer be constant in a particular medium but may vary from grid point to grid point. The scheme automatically accounts for the spatial variation in the elastic parameters across an interface whose

geometrical complexity is limited only by the choice of the grid intervals Δx and Δz (Kelly *et al.*, 1976).

The second-order partial differential equations defining P-SV wave propagation in a 2-D medium in the rectangular coordinated x and z can be written (Kolsky, 1963, p. 11; Karal and Keller, 1959)

$$\rho \frac{\partial^2 u}{\partial t^2} = \frac{\partial}{\partial x} \left[\lambda \left(\frac{\partial u}{\partial x} + \frac{\partial w}{\partial z} \right) + 2\mu \frac{\partial u}{\partial x} \right] + \frac{\partial}{\partial z} \left[\mu \left(\frac{\partial w}{\partial x} + \frac{\partial u}{\partial z} \right) \right] \quad (3.29)$$

$$\rho \frac{\partial^2 w}{\partial t^2} = \frac{\partial}{\partial z} \left[\lambda \left(\frac{\partial u}{\partial x} + \frac{\partial w}{\partial z} \right) + 2\mu \frac{\partial w}{\partial z} \right] + \frac{\partial}{\partial x} \left[\mu \left(\frac{\partial w}{\partial x} + \frac{\partial u}{\partial z} \right) \right]$$

The assumption that the density ρ is constant throughout the model enables us to write the above equations as function of the spatially varying P and SV wave velocities, i.e., λ and μ (Lame parameters) can be replaced by expressions in $\alpha(x, z)$ and $\beta(x, z)$. This assumption admittedly reduces the generality of model. A finite-difference scheme was developed to approximate equations (3.29). The time differentials on the left-hand sides can be represented by the same centered differences. On the right-hand side, however, the complication of differentiating terms which contain the spatially dependent elastic velocities is faced. Two types of terms are considered in equation (3.29), specifically, those having partial derivatives with respect to both spatial variables (i.e., mixed derivatives). Consider a term typical of the first type,

$$\frac{\partial}{\partial x} \left[\alpha^2(x, z) \frac{\partial u}{\partial x} \right] \quad (3.30)$$

Let $\alpha^2(x, z)$ be replaced by its discrete value $\alpha^2(m, n)$ at the grid point (m, n) . $\alpha^2(m, n)$ is defined as the average value of $\alpha^2(x, z)$ over a rectangle, of sides Δx and Δz , centered at the grid point $(m\Delta x, n\Delta z)$. Mitchell (1969, p.22-25) and Boore (1972) discuss various approximations to (3.30). Experience thus far appears to indicate that many of these formulas yield comparable results. An approximation which has been found to perform satisfactorily is

$$\frac{\alpha^2\left(m + \frac{1}{2}, n\right) [u(m + 1, n, l) - u(m, n, l)] - \alpha^2\left(m - \frac{1}{2}, n\right) [u(m, n, l) - u(m - 1, n, l)]}{(\Delta x)^2} \quad (3.31)$$

where the averages $\alpha^2\left(m + \frac{1}{2}, n\right)$ and $\alpha^2\left(m - \frac{1}{2}, n\right)$ are defined in the form,

$$\alpha^2\left(m \pm \frac{1}{2}, n\right) = \frac{\alpha^2(m \pm 1, n) + \alpha^2(m, n)}{2} \quad (3.32)$$

Consider a term typical of a mixed derivative,

$$\frac{\partial}{\partial z} \left[\alpha^2(x, z) \frac{\partial}{\partial x} u(x, z, t) \right] \equiv \frac{\partial}{\partial z} [c(x, z, t)] \quad (3.33)$$

where the function $c(x, z, t)$ has been introduced for convenience. The right member (3.33) may be approximated by the centered first-order difference,

$$\frac{\partial}{\partial z} [c(x, z, t)] \cong \frac{c(m, n + 1, l) - c(m, n - 1, l)}{2\Delta z} \quad (3.34)$$

Let $c(x, z, t) = \alpha^2(x, z) \frac{\partial}{\partial x} u(x, z, t)$ be approximated by the centered first-order difference,

$$c(m, n, l) \cong \alpha^2(m, n) \cdot \frac{u(m + 1, n, l) - u(m - 1, n, l)}{2\Delta x} \quad (3.35)$$

substitution of (3.35) into (3.34) yields the expression

$$\begin{aligned} & \frac{\partial}{\partial z} \left[\alpha^2(x, z) \frac{\partial}{\partial x} u(x, z, t) \right] \\ & \cong \frac{1}{4\Delta x \Delta z} \{ \alpha^2(m, n + 1) \cdot [u(m + 1, n + 1, l) - u(m - 1, n + 1, l)] \\ & \quad - \alpha^2(m, n - 1) \cdot [u(m + 1, n - 1, l) - u(m - 1, n - 1, l)] \} \end{aligned} \quad (3.36)$$

The other terms of (3.30) are treated in a likely manner. One finally obtains the two coupled finite-difference equations, hence detailed derivation of these formulas is beyond the scope of this dissertation. Further information about these equations can be found in Kelly *et al.*, (1976).

3.4. Theoretic Gravity Computation

In the quantitative interpretation of gravity surveys, 2-D calculations along profiles perpendicular to the axis of an infinitely long prismatic body have been popular (Talwani *et al.*, 1959; Talwani and Heirtzler, 1964). Reasons for this popularity are that structures which approach two dimensionality are common in geology. An equation is extracted for the vertical gravity field due to a homogeneous medium with polygonal cross-section and finite strike-length. The equation can be divided into the 2-D terms of Talwani *et al* (1959) and precise terms for the contributions of the ends of the prism. This approach permits gravity calculation for multiple bodies, along profiles with variable field point elevation (Cady, 1980).

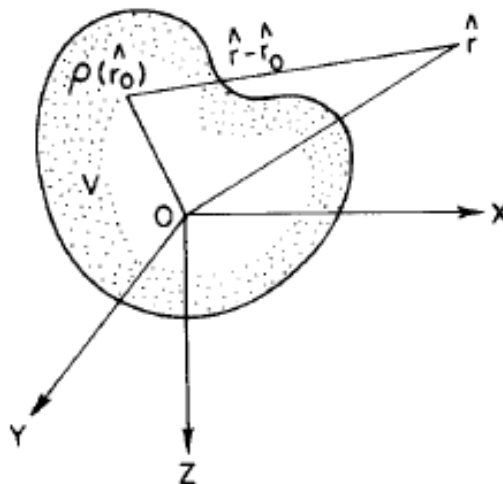


Figure 3.5. Density distribution $\rho(\hat{r}_0)$ within volume V as seen from field point \hat{r} (Cady, 1980).

The gravitational field at a point \hat{r} external to a continuous mass distribution $\rho(\hat{r}_0)$ contained within a volume V (Figure 3.5) is given by

$$\hat{F}(\hat{r}) = -\nabla U(\hat{r}) \quad (3.38)$$

where the gravitational potential is

$$U(\hat{r}) = -G \int_V \rho(\hat{r}_0) \frac{d^3r_0}{|\hat{r} - \hat{r}_0|} \quad (3.39)$$

(Grant and West, 1965, p.211). G is the universal gravitational constant.

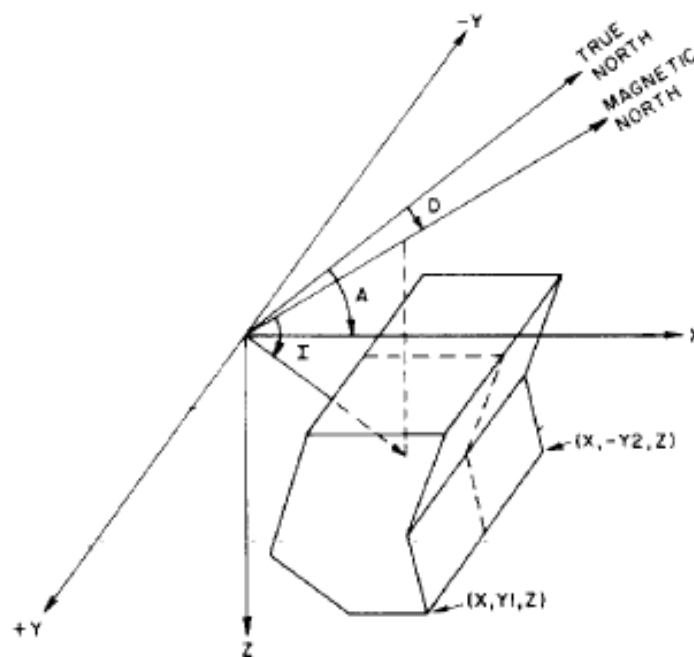


Figure 3.6. Geometry of 2.5-D body, z-axis is positive down, y-axis is along strike, and traverse is along x-axis. A is the angle between the x-axis and true north, and D is the declination of the earth's magnetic field, both positive clockwise. I is the inclination of the earth's magnetic field (Cady, 1980).

Figure 3.6 defines the right-handed coordinate system and shows the body over which is integrated. The y-axis is parallel to the strike of the body, and observations lie along a profile contained within the x-z plane. Equations (3.38) and (3.39) expand to

$$F_x = -2G\rho \partial U/\partial x \quad (3.40)$$

$$F_y = -2G\rho \partial U/\partial y \quad (3.41)$$

$$F_z = -2G\rho \partial U/\partial z \quad (3.42)$$

these expressions have the form of first partial derivatives of volume integrals. Without loss of generality, the coordinate origin at the observation point \hat{r} is placed and the subscript from the body point \hat{r}_0 is dropped. Assuming uniform density ρ , equation (3.42) becomes

$$F_z = -G\rho \iiint \frac{\partial}{\partial z} (x^2 + y^2 + z^2)^{-\frac{1}{2}} dx dy dz \quad (3.43)$$

F_z is chosen for detailed integration because the total gravity field, which is measured, is vertical by definition. In the gravity case, the body can be allowed to have different partial strike lengths Y_1 and Y_2 . In order to avoid ambiguities of sign, Y_1 and Y_2 are defined, for the purposes of this derivation, as positive distances from the x-z plane (Y_1 positive in the +Y direction, Y_2 positive in the -Y direction). Integrating equation (3.43) from $-Y_2$ to 0 and 0 to Y_1 yields

$$F_z = -G\rho \frac{\partial}{\partial z} \iint [-\ln(x^2 + z^2) + \ln(Y_1 + R_1) + \ln(Y_2 + R_2)] dx dz \quad (3.44)$$

where $R_1 = \sqrt{x^2 + y_1^2 + z^2}$ and $R_2 = \sqrt{x^2 + y_2^2 + z^2}$.

Integration of equation (3.44) over z yields

$$F_z = -G\rho \int_{x_1}^{x_2} [-\ln(x^2 + z^2) + \ln(Y_1 + R_1) + \ln(Y_2 + R_2)]_{z_1}^{z_2} dx \quad (3.45)$$

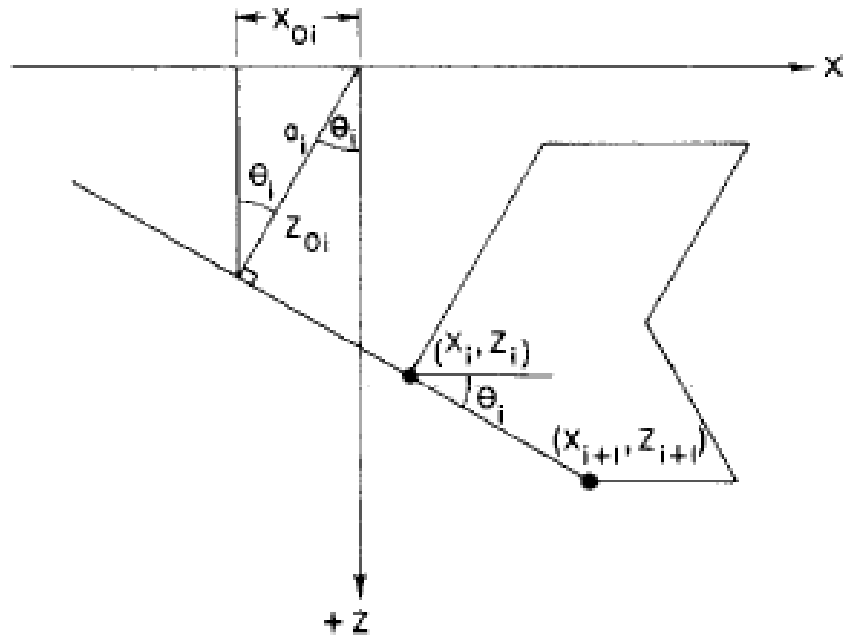


Figure 3.7. The x - z relationship along one side of the polygonal cross-section (Cady, 1980).

The integral over the area of the polygon can be converted to a line integral around the polygon by expressing z as a function of x along each side. For each side in turn (Figure 3.7), let

$$z = m_i x + z_{0i} \quad (3.46)$$

where

$$m_i = \tan \theta_i = \frac{z_{i+1} - z_i}{x_{i+1} - x_i} \quad (3.47)$$

and z_{0i} is the intercept of the extension of the i th side. Equation (3.45) becomes

$$F_z = +G\rho(I_0 - I_1 - I_2) \quad (3.48)$$

where

$$I_0 = \oint \ln[x^2 + (mx + z_0)^2] dx$$

$$I_n = \oint \ln\left(Y_n + \sqrt{Y_n^2 + x^2 + (mx + z_0)^2}\right) dx \quad (3.49)$$

for $n = 1, 2$ (Cady, 1980).

4. DATA ACQUISITION

4.1. Field Experiment

As a part of the CyprusArc project, a seismic wide-angle reflection/refraction experiment was carried out in March 2010. The 300 km and 45 km long north – south trending profiles extended from Cihanbeyli in Central Anatolia to Anamur in eastern Mediterranean and in southern Cyprus, respectively (Figure 4.1). This project was planned for collecting data in the sea using an airgun on a German research vessel which is called RV Maria S. Merian cooperated by Hamburg University and explosions in boreholes on land with a support by Geophysical Deep Sounding department of Deutches GeoForschungsZentrum (GFZ). Profiles cross Central Anatolian plateau and Taurus Mountains in Turkey and Troodos ophiolite in southern Cyprus. There is a sharp topography along the profile in Turkey and the elevation difference between north and south is approximately 850 m increasing from north to south. The seismic experiment was comprised of two explosions of 1125 kg explosives onshore and 98 cubic liters airguns offshore. The purpose of the explosions was to obtain arrivals from the whole crust including Moho refraction (Pn waves). Totally 245 stations were installed on land. 76 three-component sensors and 119 vertical-component sensors were installed along ~300 km distances between Cihanbeyli and Anamur with an average spacing of 1.25 km. 25 three-component sensors and 25 vertical component sensors were deployed along 45 km distances on land at southern Cyprus with an average spacing of 1.25 km. The data were recorded continuously with 100 Hz sampling rate for a period of two days in Turkey and two weeks in Cyprus.

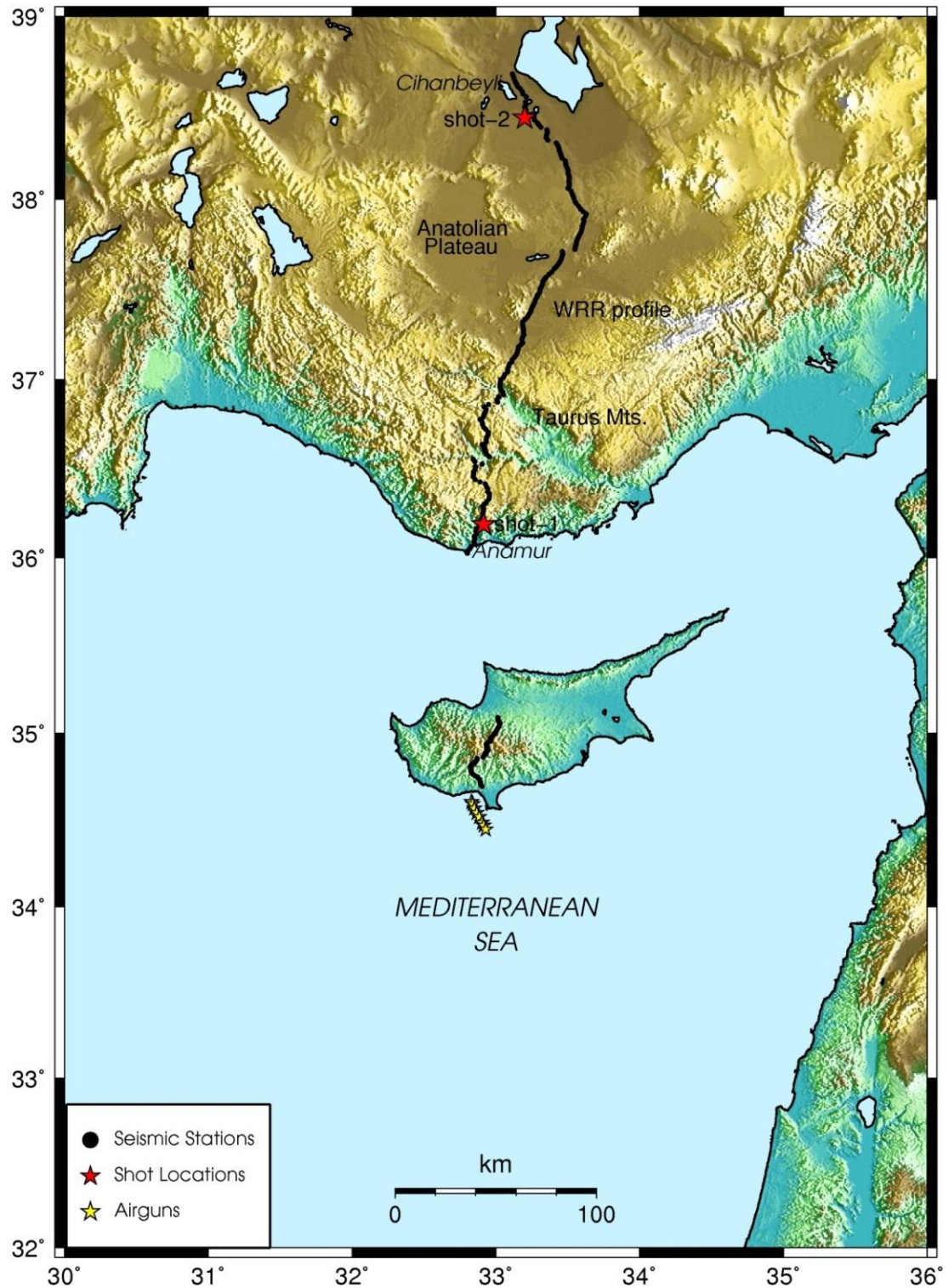


Figure 4.1. Seismic experiments in Turkey and southern Cyprus. The 300 km long wide angle reflection/refraction profile in Turkey and the 45 km long profile in southern Cyprus (black dots). Red stars show explosions. Yellow stars show airguns.

4.2. Instrumentation

Seismic recording units called Texan Reftek-125A-01, EDL PR6-24 and DSS-cube (Figure 4.2) have been used during the 2010 spring seismic experiment. They are characterized by a small and light-weight design and extremely low power consumption instruments. These recording units are being widely used in seismic reflection-refraction surveys, microtremor and aftershock studies. Recording instruments can take continuous records with a different sampling rate such as 1000, 500, 250, 200,125, 100, 50, 40, 25, 10, 8, 5, 4, 2 and 1 sample/second. They have responsive timing units: an external GPS with timing accuracy approximately ± 5 msec relative to the shot time. The control of the time information in the recording units and the errors in an acceptable range is the most important factor while collecting the data. Seismic recorders equipped with vertical component sensors (SM-6, GS-30CT, L-22) and three component sensors (PE-6/B and Mark-L4C3D). All sensors are with a response of ground velocity of 4.5 Hz to 150Hz, approximately. Three component geophones were used to detect potential ghost waves which originates from a short-path multiple, or a spurious reflection and trapped waves where rock types changes.



Figure 4.2. Seismic recorders (top), vertical component sensors (middle) and three component sensors (bottom).

5. DATA PROCESSING

5.1. Creating Shot Gathers

The data continuously recorded by REFTEK, CUBE and EDL instruments at different formats were converted into first SEG-Y and later SAC formats for each receiver, respectively. The origin times of the sources were recorded during the experiment using a hand GPS. We also used a geophone close to shot locations to determine origin times more accurately. The continuous SAC data for each receiver were cut into 15.542 second length files from the origin time as a start time for each explosion. Then shot gathers were formed by merging 15.542 second sac files and sorting as a function of distance. We created 390 shot gathers for explosions along the 300 km long profile in Turkey and 63 shot gathers for the explosion at Anamur and eight airguns along 180 km long profile between southern Turkey and southern Cyprus. The offsets of the traces are split into the south (positive value) and the north (negative value) directions. Seismic traces are plotted after applying DC removal to the data. The amplitudes were normalized by the maximum of each trace and geometric spreading effect was alleviated.

5.2. Seismic Data and Phase Correlations

After creating the shot gathers in SAC format, we used an interactive plotting and picking software called SAC (Seismic Analysis Code), previously SAC2000 (<http://www.iris.edu/hq/>). The program is designed for the study of sequential data, particularly time-series data. Analysis capabilities include general arithmetic operations, Fourier transforms, three spectral estimation methods, IIR and FIR filtering, signal stacking, decimation, interpolation, correlation and seismic phase picking. SAC also contains an extensive graphic capability (Helffrich *et al.*, 2013).

An uncertainty is calculated by using the signal to noise ratio (S/N ratio) for each pick from the onshore recordings. An empirical relationship is defined for the calculation of uncertainties:

$$\begin{aligned}
\frac{S}{N} \leq 1 &\Rightarrow \text{error} \cong 0.3 \text{ s} \\
4 > \frac{S}{N} > 1 &\Rightarrow \text{error} \cong \frac{0.3}{S/N} \text{ s} \\
\frac{S}{N} \geq 4 &\Rightarrow \text{error} \cong 0.06 \text{ s}
\end{aligned}
\tag{5.1}$$

For each pick from the onshore recordings at two land shots an uncertainty of approximately 0.3 s was assigned except for the first arrivals, obtained distances less than 60 km (for southern shot point in Turkey) and 40 km (for northern shot point in Turkey), for which an uncertainty of 0.1 was assigned. At these distances the first arrivals were clearly picked without any filter. A frequency analysis was performed to reveal the dominant frequency content of the main signal. The frequency content of all stations was analyzed by an interactive spectral analysis, which uses the Fourier Transform. For the southern shot-point in Turkey, at short distances (less than 60 km), first arrivals are clearly picked without any filter. Distances between 60 and 130 km through north 1-20 Hz band pass filter and at long distances beyond 130 km 3-10 Hz band pass filters were applied before picking the arrival times. For the northern shot-point in Turkey, at short distances (less than 40 km), first arrivals were clearly picked without any filter. Distances between 40 and 110 km through the south 1-20 Hz band pass filter and at long distances greater than 110 km 3-10 Hz band pass filter were applied before picking the arrival times. For explosions, the delay of 0.542 second due to the firing system has been taken into account. For each receiver at the southern Cyprus, first arrivals were picked by applying 4-8 Hz band pass filter to the airgun recordings.

All refracted and reflected P waves, particularly the refracted phases through the crust (Pg) and uppermost mantle (Pn) and the reflected phase from the crust-mantle boundary (PmP), were potentially picked phases in the data set. The recordings of both land shots (shot-1 and shot-2) and airguns show a good data quality. All seismic traces received from airgun shots have a clear onset of the first arrivals (Figures 5.4 – 5.11). The southern land shot has a good S/N ratio till about 200 km to the north and Pg was observed as the first arrival at this distance. Second arrivals could not be efficiently picked to the north from the shot point due to the ringing nature of the seismograms for this shot (Figure 5.1). The northern land shot has a good data quality through the end point of the profile, the south coast of Turkey at about 270 km distance. Pg was clearly picked till about 230

km distance and Pn overtakes Pg as the first arrival after that distance. Additionally, the Moho reflection (PmP) was picked between 60 and 220 km distances (Figure 5.2). The southern land shot was recorded at the Cyprus stations. Pg was picked till approximately the first 20 km distance from starting point of the profile at south Cyprus. Beyond 20 km distance, the other arrivals (the first arrival and some reflected phases) could not be picked effectively due to a high noise level (Figure 5.3). Pg was clearly picked along whole record sections along southern Cyprus for each airgun recordings.

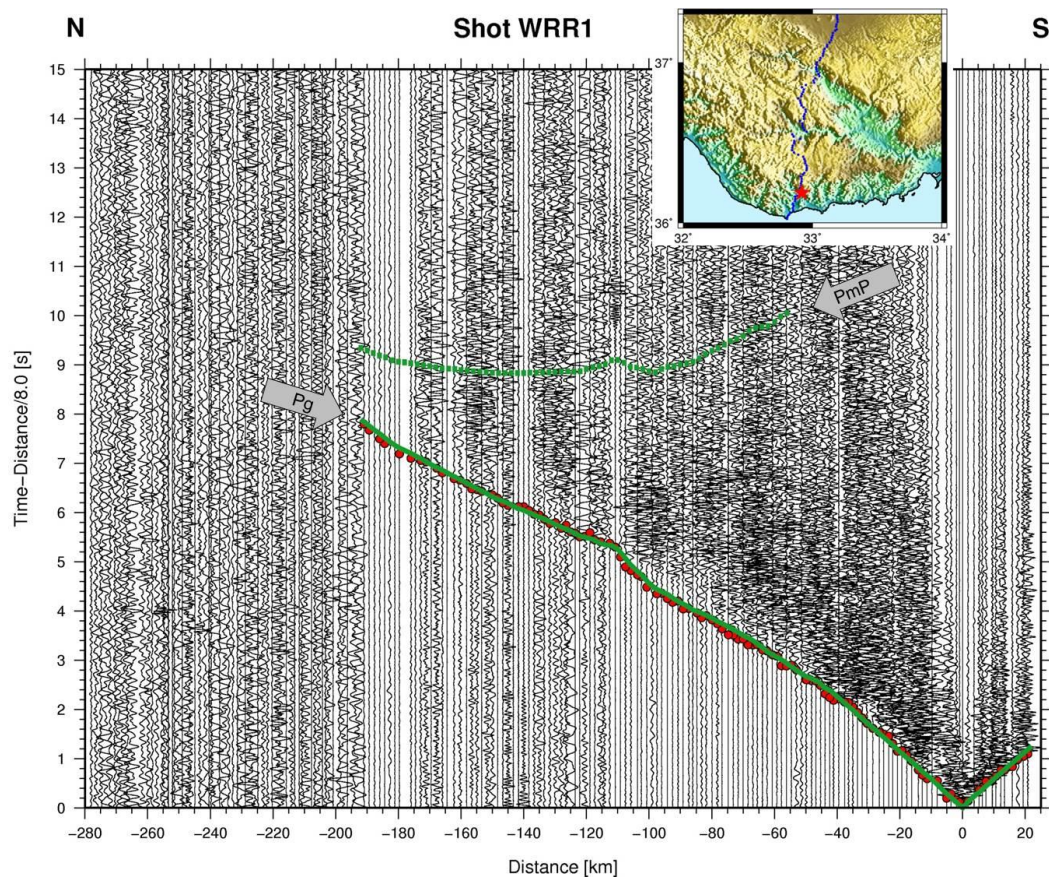


Figure 5.1. Seismic record section of southern land shot of Turkey. Red dots show picked first arrival times. Green solid lines show calculated first arrival times (Pg) and green dashed lines show calculated travel times from reflected phases from the Moho (PmP), based on the final 2-D P wave velocity model. Seismic traces are plotted after DC removal. The amplitudes were normalized by the maximum of each trace and geometric spreading effect was alleviated. The trace at 0 m shows the seismic signal recorded close to shot locations.

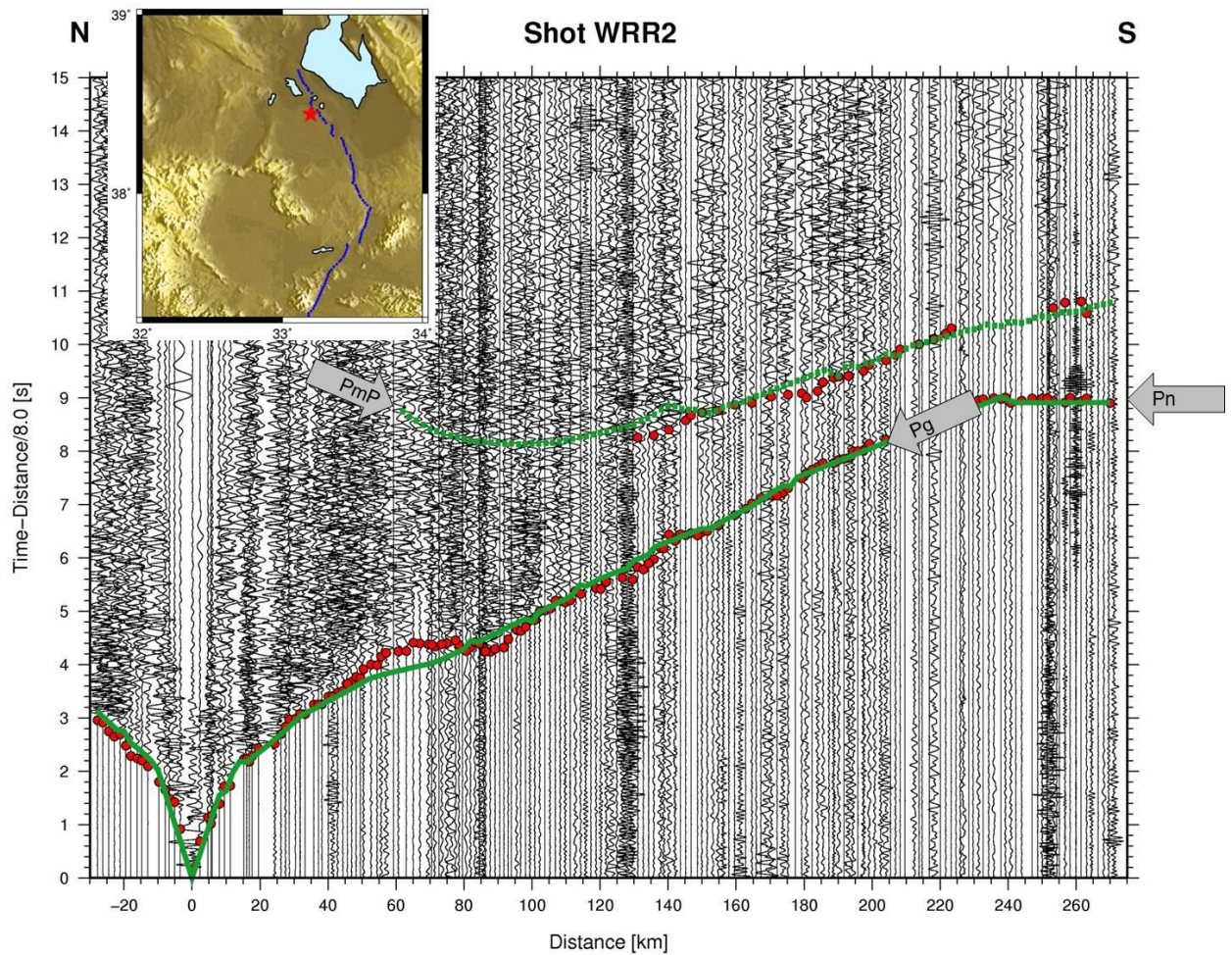


Figure 5.2. Seismic record section of northern land shot of Turkey. Red dots show picked first arrival times and reflected phases. Green solid lines show calculated first arrival times (Pg) and Pn and green dashed lines show calculated travel times from reflected phases from the Moho (PmP), based on the final 2-D P wave velocity model. Seismic traces are plotted after DC removal. The amplitudes were normalized by the maximum of each trace and geometric spreading effect was alleviated. The trace at 0 m shows the seismic signal recorded close to shot locations.

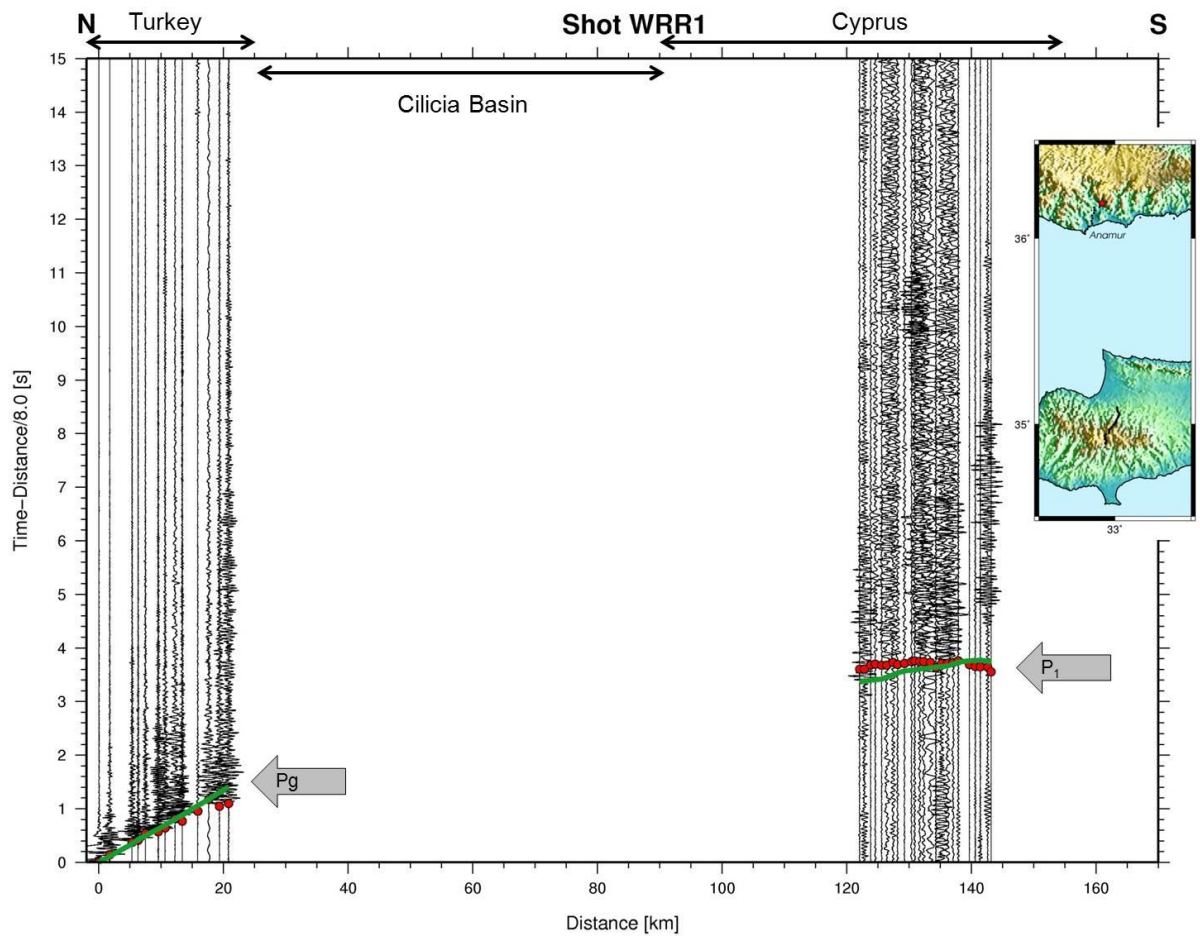


Figure 5.3. Seismic record section of southern land shot of Turkey. Red dots show picked first arrival times. Green solid lines show calculated first arrival times (P_g and P_1) based on the final 2-D P wave velocity model. Seismic traces are plotted after DC removal. The amplitudes were normalized by the maximum of each trace and geometric spreading effect was alleviated. The trace at 0 m shows the seismic signal recorded close to shot locations.

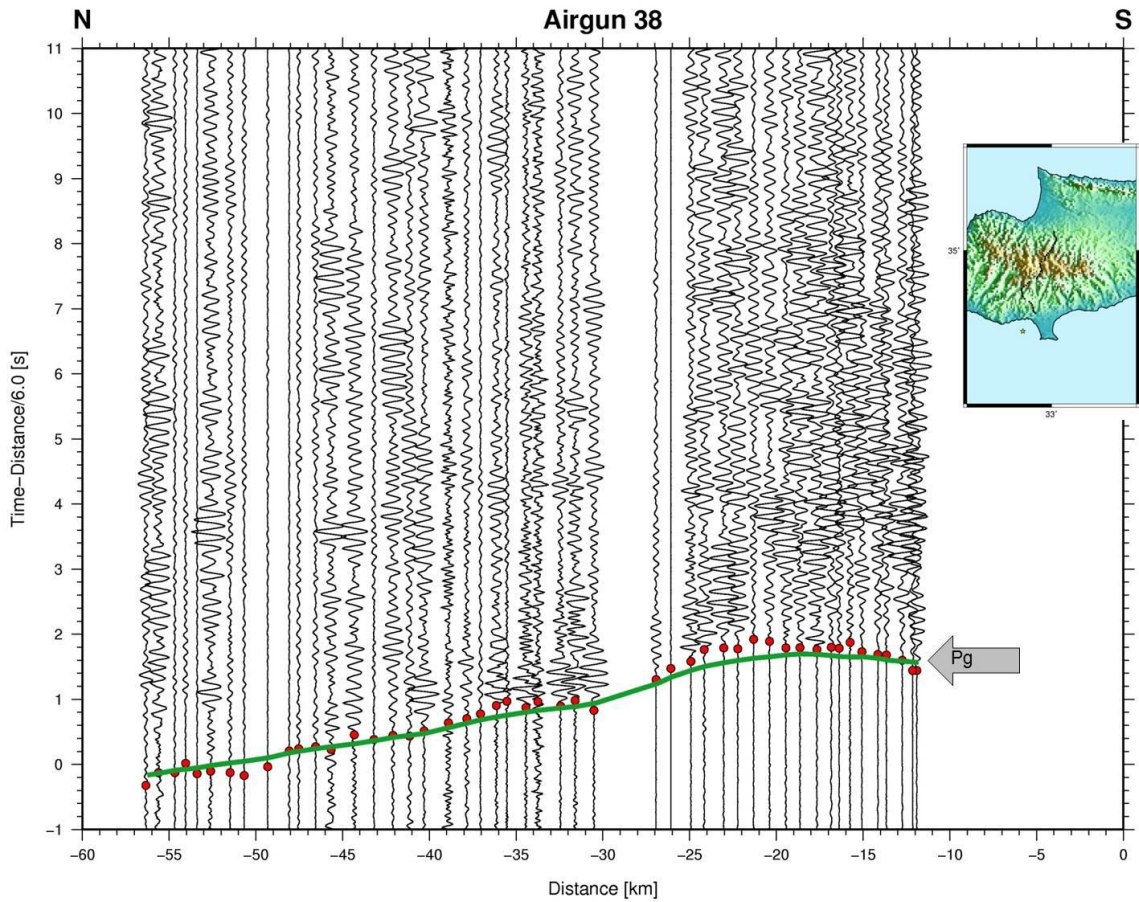


Figure 5.4. Seismic record section of Airgun 38. Red dots show picked first arrival times. Green solid lines show calculated first arrival times (P_g) based on the final 2-D P wave velocity model. Seismic traces are plotted after DC removal. The amplitudes were normalized by the maximum of each trace and geometric spreading effect was alleviated.

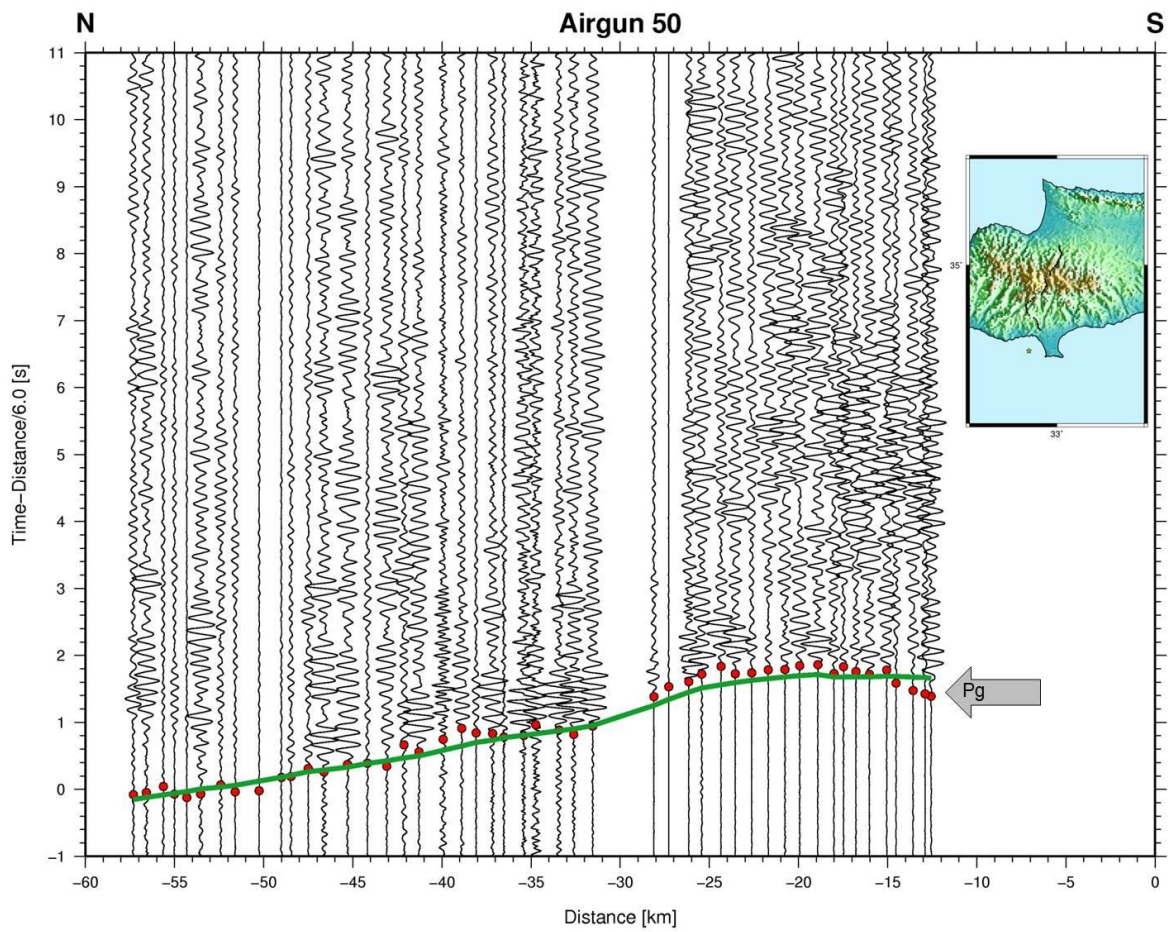


Figure 5.5. Seismic record section of Airgun 50. Red dots show picked first arrival times. Green solid lines show calculated first arrival times (P_g) based on the final 2-D P wave velocity model. Seismic traces are plotted after DC removal. The amplitudes were normalized by the maximum of each trace and geometric spreading effect was alleviated.

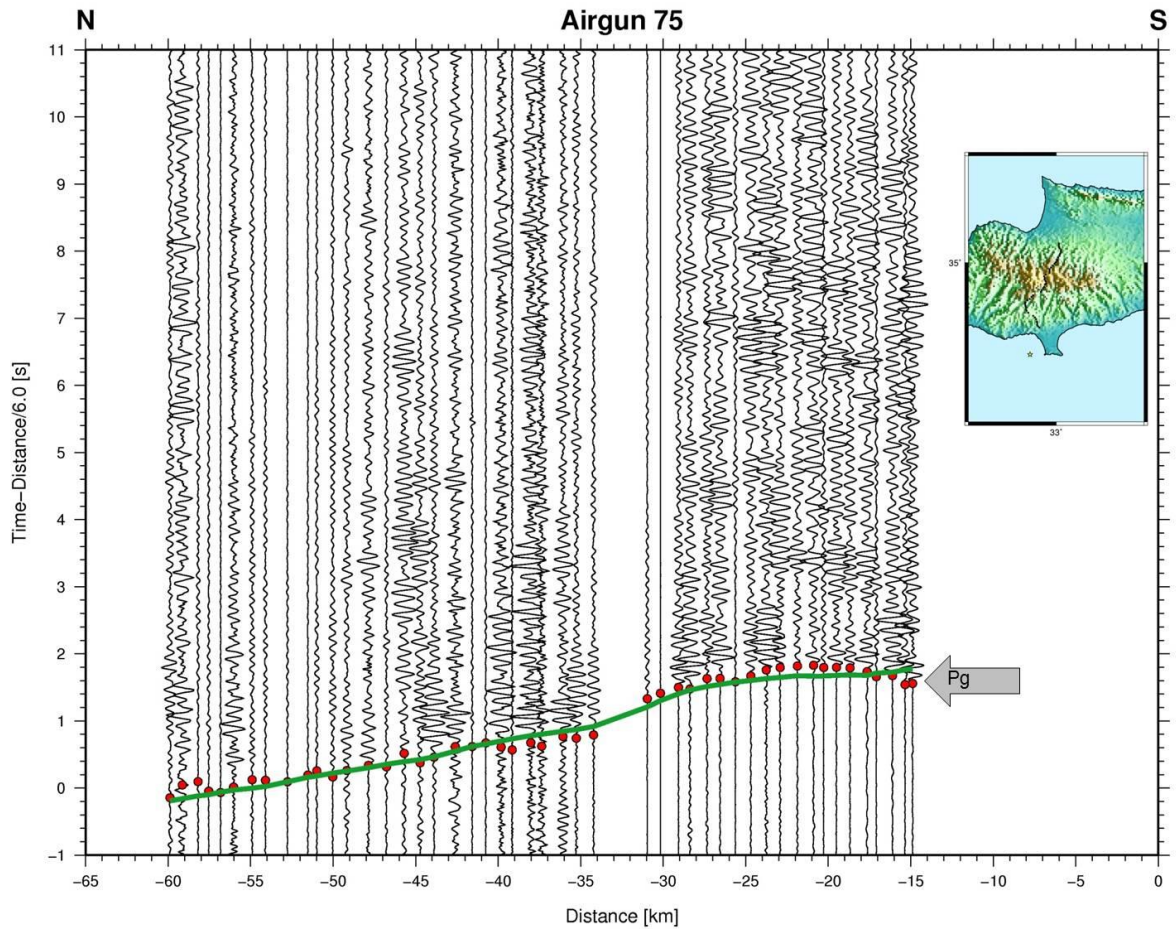


Figure 5.6. Seismic record section of Airgun 75. Red dots show picked first arrival times. Green solid lines show calculated first arrival times (Pg) based on the final 2-D P wave velocity model. Seismic traces are plotted after DC removal. The amplitudes were normalized by the maximum of each trace and geometric spreading effect was alleviated.

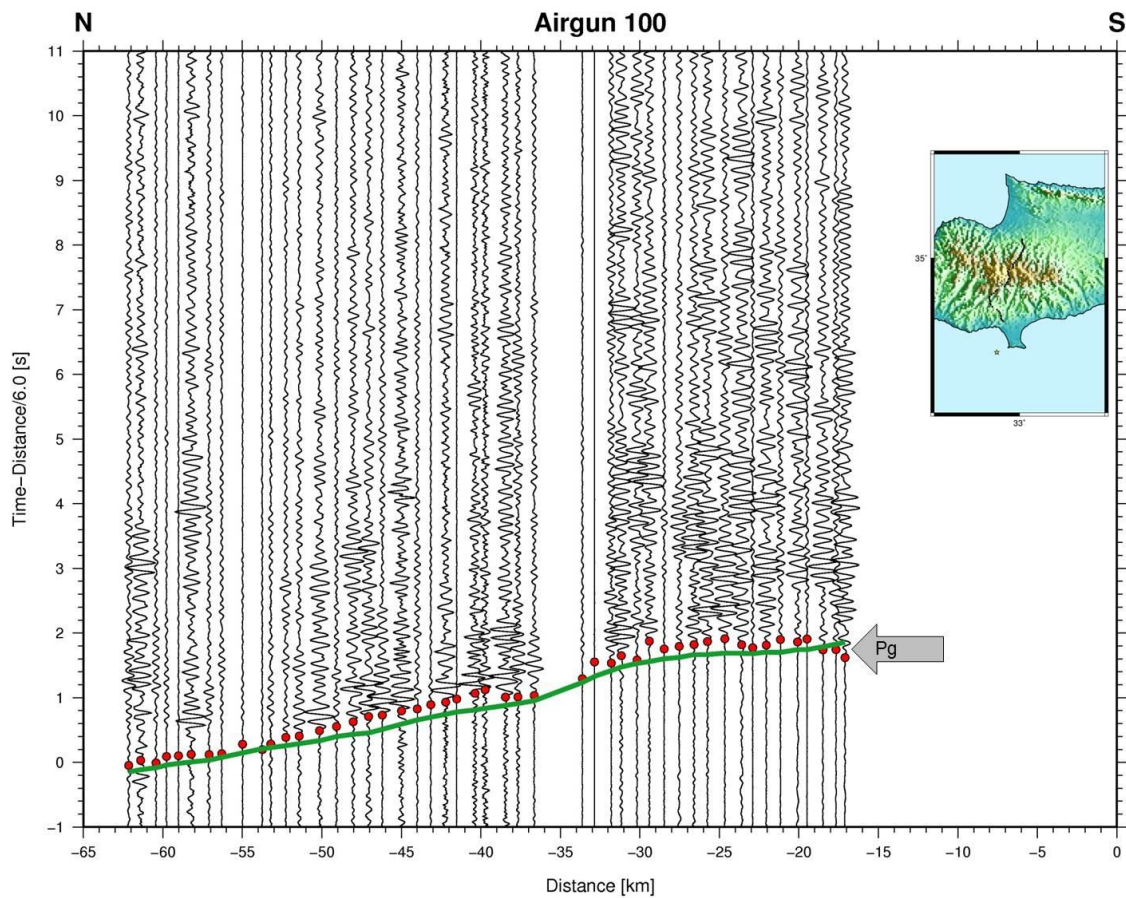


Figure 5.7. Seismic record section of Airgun 100. Red dots show picked first arrival times.

Green solid lines show calculated first arrival times (P_g) based on the final 2-D P wave velocity model. Seismic traces are plotted after DC removal. The amplitudes were normalized by the maximum of each trace and geometric spreading effect was alleviated.

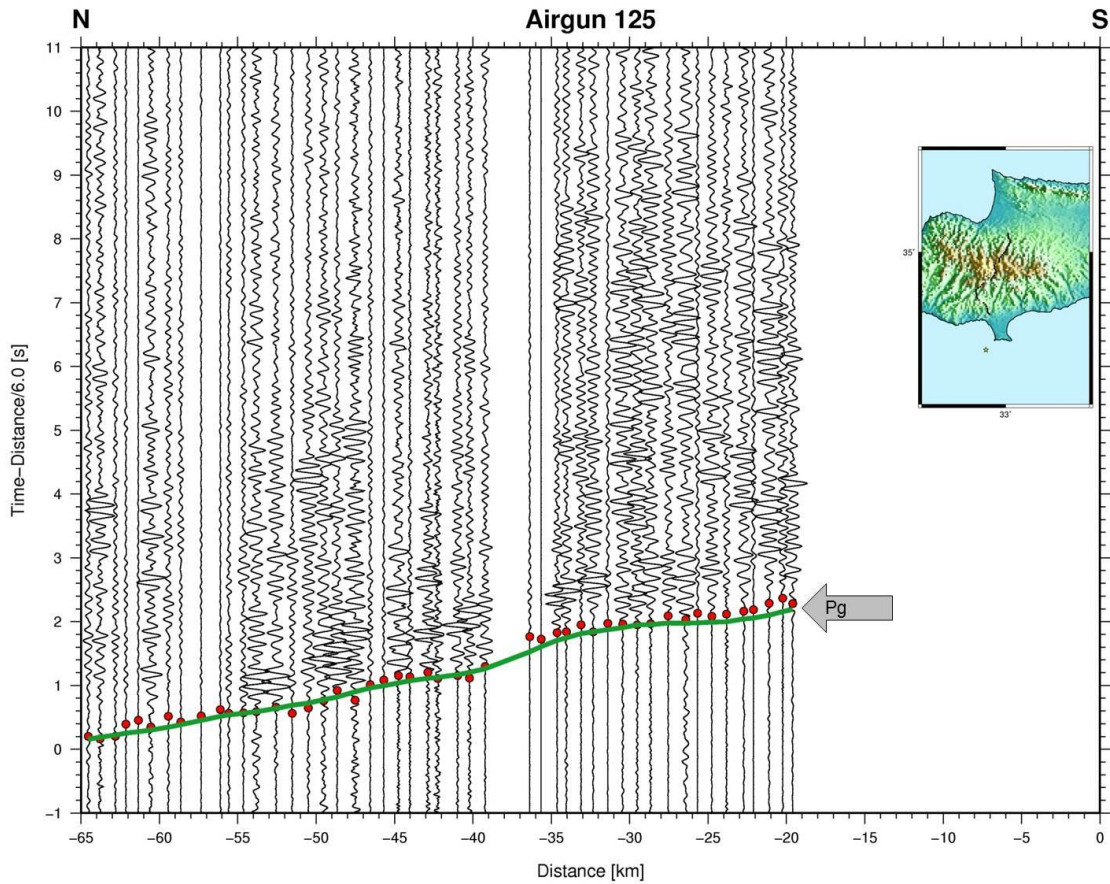


Figure 5.8. Seismic record section of Airgun 125. Red dots show picked first arrival times. Green solid lines show calculated first arrival times (P_g) based on the final 2-D P wave velocity model. Seismic traces are plotted after DC removal. The amplitudes were normalized by the maximum of each trace and geometric spreading effect was alleviated.

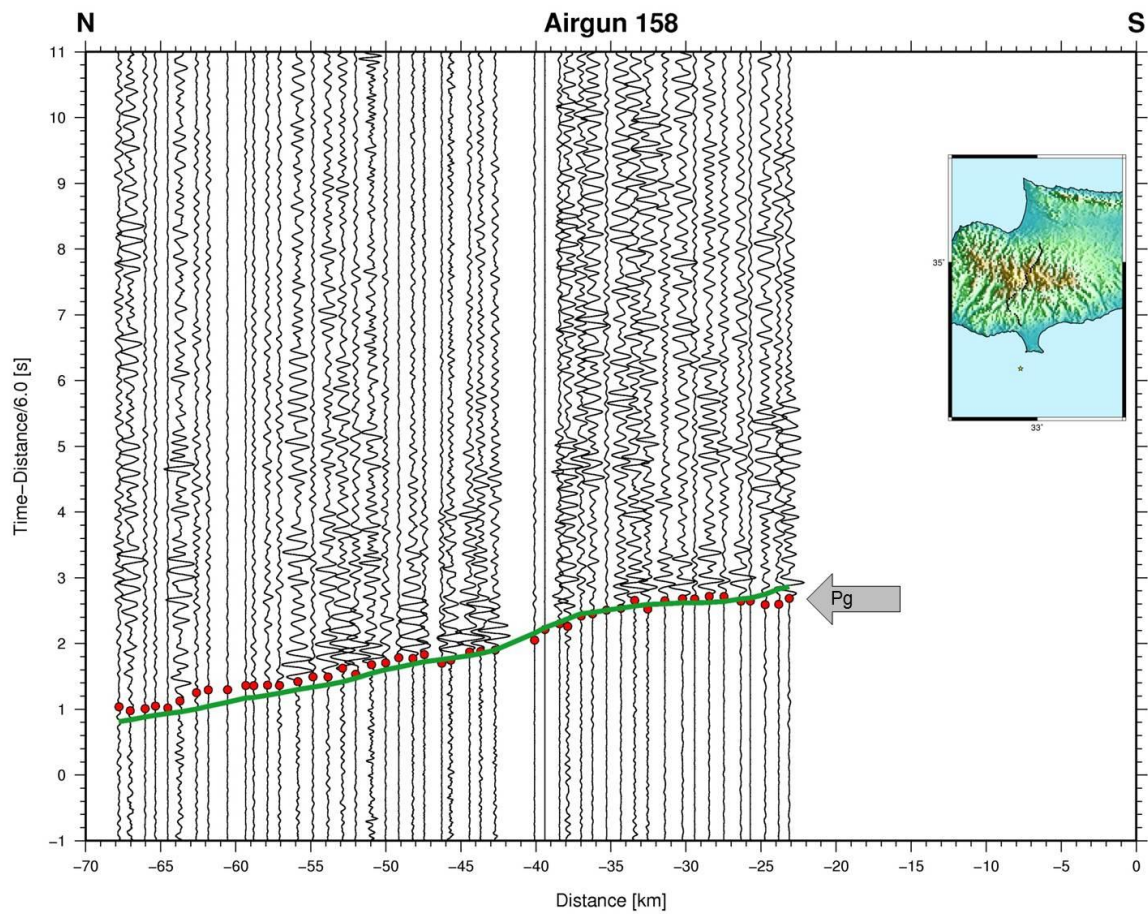


Figure 5.9. Seismic record section of Airgun 158. Red dots show picked first arrival times. Green solid lines show calculated first arrival times (Pg) based on the final 2-D P wave velocity model. Seismic traces are plotted after DC removal. The amplitudes were normalized by the maximum of each trace and geometric spreading effect was alleviated.

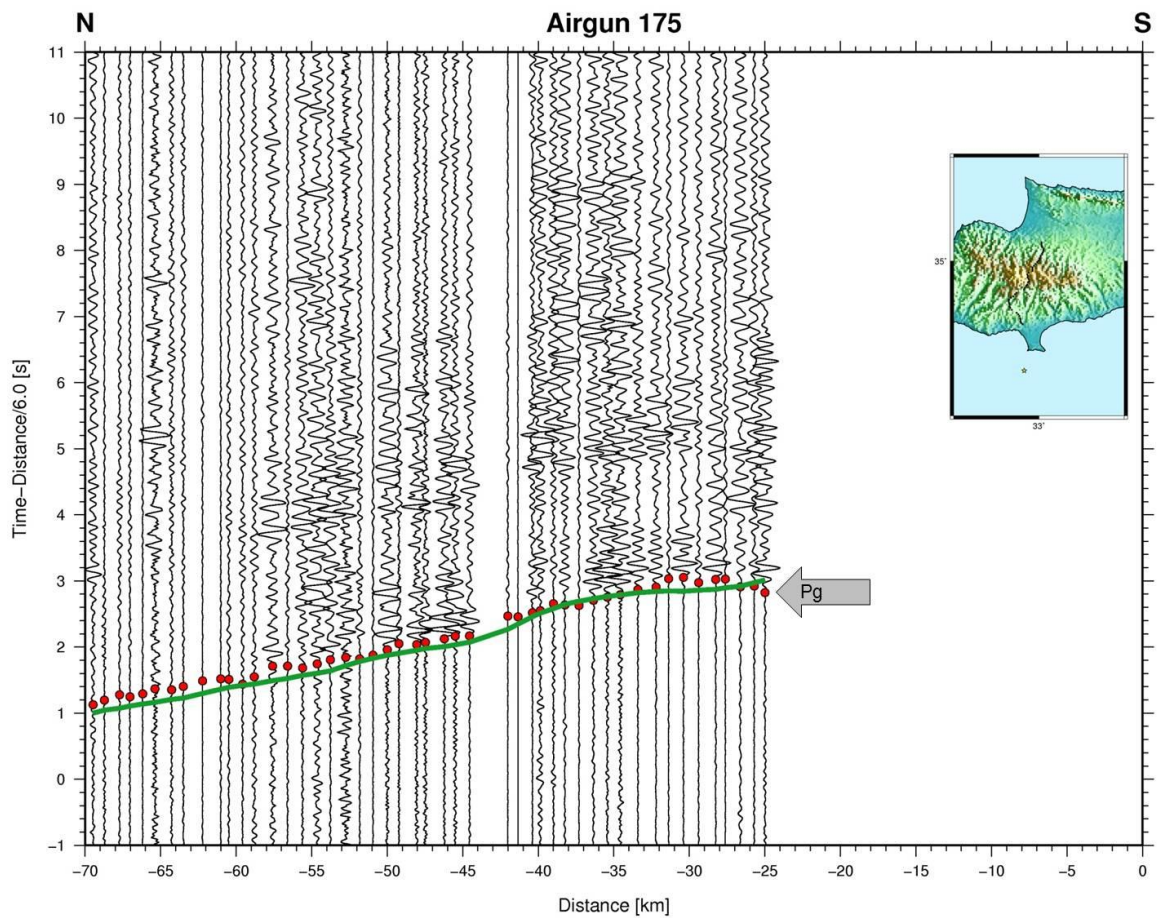


Figure 5.10. Seismic record section of Airgun 175. Red dots show picked first arrival times. Green solid lines show calculated first arrival times (P_g) based on the final 2-D P wave velocity model. Seismic traces are plotted after DC removal. The amplitudes were normalized by the maximum of each trace and geometric spreading effect was alleviated.

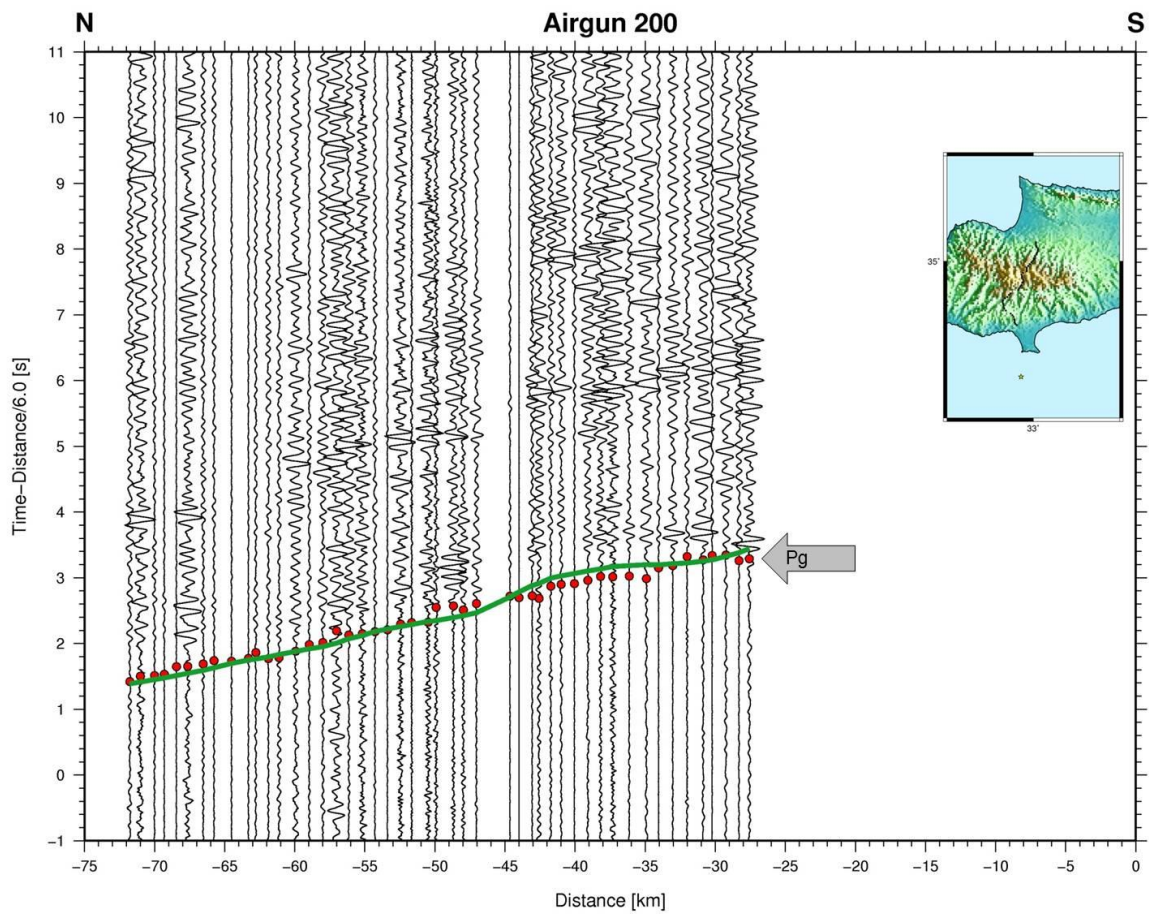


Figure 5.11. Seismic record section of Airgun 200. Red dots show picked first arrival times. Green solid lines show calculated first arrival times (Pg) based on the final 2-D P wave velocity model. Seismic traces are plotted after DC removal. The amplitudes were normalized by the maximum of each trace and geometric spreading effect was alleviated.

6. 2-D TRAVEL TIME MODELLING RESULTS

The Earth's crust displays a heterogeneous composition on a wide range of spatial scales, containing discontinuities, faults, layering, intrusions and partial melt. Imaging this complex structure mainly depends on the density of ray sampling, proportional to the minimum wavelength of the recorded seismic wave energy (Thurber, 1993). Ray tracing methods provide numerical modelling of seismic wave field in 2-D laterally varying structures. For the travel time modelling, the forward problem to determine the rays and travel times was solved by classical ray tracing techniques (Cerveny *et al.* 1977) for the reflected phases, and finite-difference ray tracing based on the eikonal equation (Vidale 1988; Podvin & Lecomte 1991; Schneider *et al.* 1992) for the refracted phases.

The program based on SEIS81, first written by Vlatislav Cerveny and Ivan Psencik then developed by Pascal Podvin - Isabel Lecomte and James Mechie, was used for forward modelling. The program is designed for a two point ray tracing and computation of seismic rays which arrive at a system of receivers distributed regularly or irregularly along the earth's surface. Corresponding travel times, amplitudes and phase shifts are also evaluated. The model is 2-D laterally inhomogeneous with curved interfaces, block structures, isolated bodies, fractures, vanishing interfaces, etc. The velocity in any layer may change both in vertical and horizontal direction. The source may be located at any point of the model. All the direct and primary reflected P and S waves, including the converted waves at the point of reflection, can be produced automatically. Multiple reflections of arbitrary type are optionally generated manually by input data. The ray diagrams are calculated as an initial value problem, they are specified by a system of initial angles from the source. The program uses a 2-D model which is specified in a right-handed Cartesian coordinate system x, y, z . The x and y axes are horizontal, the z axis is vertical, positive downwards. The model is situated in the (x, z) plane so that x coordinate increases from the left to the right. The model is bounded by two vertical boundaries on its left-hand and right-hand side and by the first and the last interface at the top and the bottom of the model. The top interface corresponds to the earth's surface (www.sw3d.mff.cz).

Initial velocity model parameters were determined by using constructed travel time – distance graphs for the profiles. Initial velocity values were determined from the slopes of travel time curves and also layer thickness was calculated by intercept time. For the profile between Anamur and south Cyprus : a detailed research was also conducted to determine the initial velocity model parameters such as P wave velocity values at every layer and thickness of the layers along the profile by using previous investigations due to the gap of seismic stations along Cilicia basin. A seismic refraction profile between Cyprus and Israel (Makris *et al.*,1983) and a stratigraphic cross section between Turkey and Cyprus in the Mediterranean Sea for very shallow subsurface which was obtained from Aksu *et al.* (2005) were inserted to initial velocity model. Additionally, chi-square value was calculated after obtaining theoretical arrival times for each 2-D model. Chi-square is a statistical test widely used to compare observed data with the calculated data. The null hypothesis, which states that there is no significant difference between the observed and theoretical or calculated result, is tested by using the chi-square test. The chi-square statistics

$$\chi^2 = \sum_i \frac{(N_i - n_i)^2}{n_i} \quad (6.1)$$

where i is station number, N_i is picked travel time and n_i is theoretical travel time. A large value of χ^2 denotes that the null hypothesis is rather unlikely. The number of events in each station is large (≥ 1), then the chi-square probability function is a good approximation to the distribution of (6.1) in the case of null hypothesis (Press *et al.*, 1986).

Figures 6.1 – 6.3 show first trials for the profile between Cihanbeyli and Anamur. Inserting a sediment layer for Tuz Golu basin reduces the residual between the observed and calculated arrival times for the northern land shot. Average χ^2 values for the Figure 6.1c and Figure 6.3c are approximately 27 and 12. Figure 6.4 show the first trial for the profile between Anamur and south Cyprus. The most important factor is to insert relatively high P-wave velocities shallow layers beneath Troodos ophiolite complex (for comparison see Figures 6.6 – 6.13) to decrease residual between observed and calculated travel times. Average χ^2 values for the Figure 6.4c is approximately 25. Forward modelling, a trial and

error process was performed for the profiles. The comparison between picked and calculated travel times was observed.

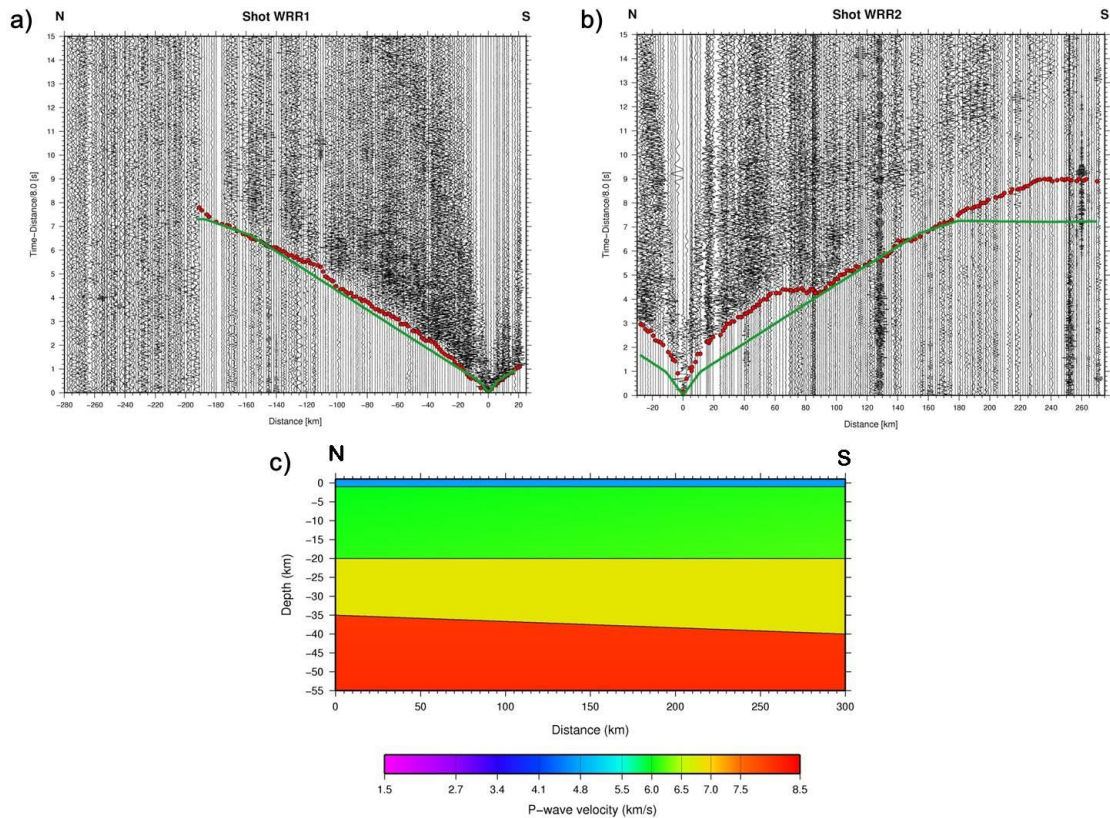


Figure 6.1. a) Seismic record section of southern land shot of Turkey b) Seismic record section of northern land shot of Turkey. Red dots show picked first arrival times. Green solid lines show calculated first arrival times based on the 2-D P wave velocity model c) 2-D P-wave velocity model.

The P wave velocity and geometry of the layer boundaries were modified to minimize differences between the observed and calculated travel times and some modifications were conducted during the modelling P wave velocity and the geometry of the subsurface topographies. The observed travel times and the calculated travel times were plotted on to the seismic traces to make a comparison (Figure 5.1 – 5.11). Figures 5.1 and 5.2 are reduced travel time-distance graphs of both land shots in Turkey and the theoretical first arrivals (green solid lines) on plots show a good fitting to the picked arrival times, with a RMS residual between observed and theoretical data of 0.25 sec. and a χ^2 value of 1.65. Moho reflections (PmP) were observed in the plot of the northern land shot

(Figure 5.2). For these reflections a RMS residual of 0.27 sec. and a χ^2 value of 1.52 were obtained. For the southern land shot, the calculated travel times for the moho reflection (PmP) sometimes fall close to larger amplitude signals between 100 – 180 km distances (Figure 5.1). For the profile at southern Cyprus, obtained using both the southern land shot in Turkey and airguns in the Mediterranean sea, south of the Cyprus, were used for forward modelling. Airgun recordings were selected according to the observation of first arrival at the last station of the northern part of the profile (Figure 4.1). The theoretical first arrival times (green solid lines) show a good fitting to the picked arrival times, with a RMS residual between observed and theoretical data of 0.23 sec. and a χ^2 value of 1.45 in average for the southern land shot in Turkey and airguns (Figures 5.3 – 5.11).

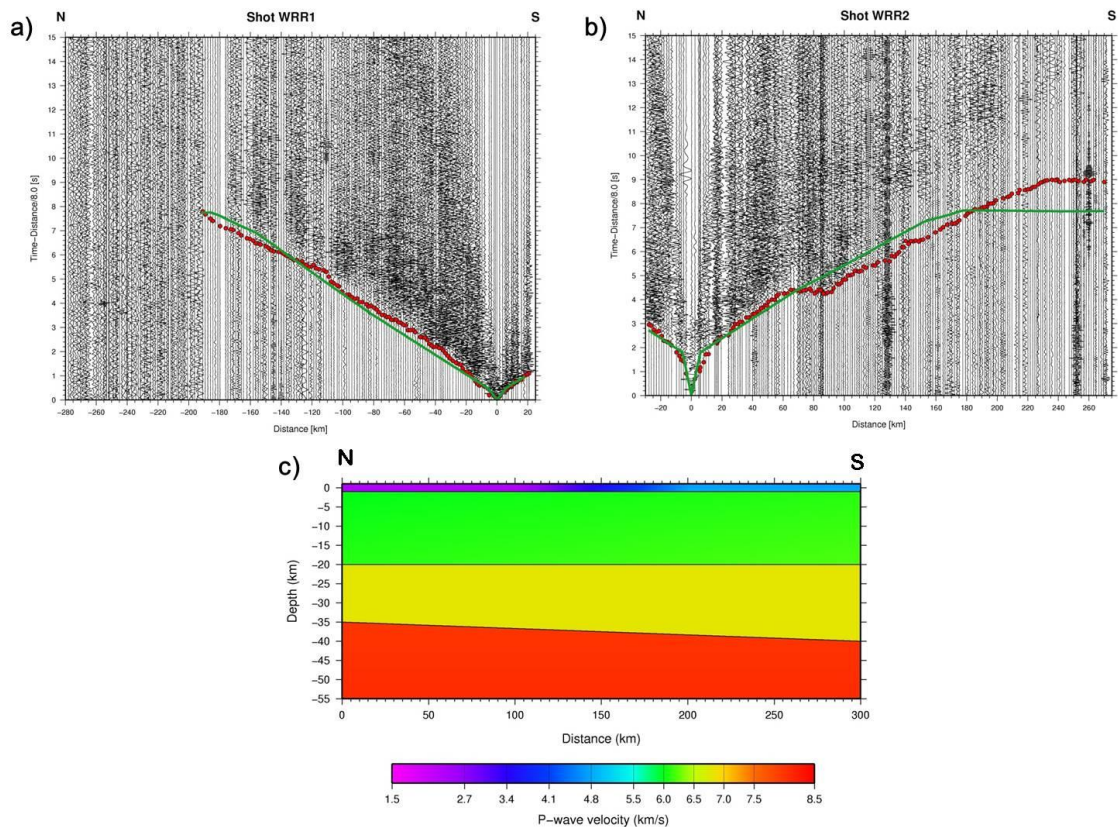


Figure 6.2. a) Seismic record section of southern land shot of Turkey b) Seismic record section of northern land shot of Turkey. Red dots show picked first arrival times. Green solid lines show calculated first arrival times based on the 2-D P wave velocity model c) 2-D P-wave velocity model.

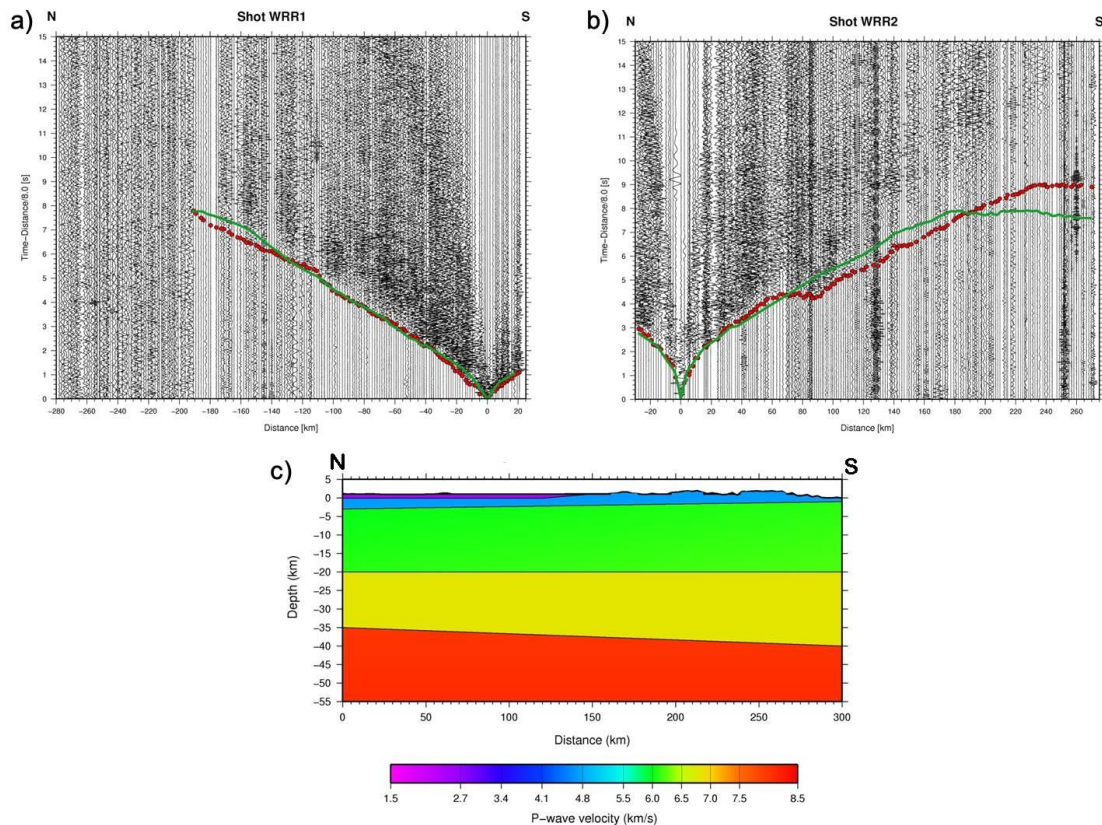


Figure 6.3. a) Seismic record section of southern land shot of Turkey b) Seismic record section of northern land shot of Turkey. Red dots show picked first arrival times. Green solid lines show calculated first arrival times based on the 2-D P wave velocity model c) 2-D P-wave velocity model.

Final 2-D crustal P wave velocity structure model shows lateral changes in velocity structure and thickness along sedimentary layer about 185 km offset and thickness along the sedimentary layer and the lower crust (Figure 6.1c). The highest lateral velocity change, from 2.8 km/s to 3.5 km/s at about 40 km offset, observed at sedimentary layer beneath the northern land shot. The sediment layer thickness decreases from 3 to 1.5 km through south and it disappears at a distance of 185 km. This marks the boundary between Tuz Golu basin (sediment filled basin) of central Anatolia and Taurus Mountains which extend parallel to the southern coast of Turkey. P wave velocity of some rock materials which brought into the sight by Taurus Mountains is 5.5 – 5.6 km/s till 5 km thickness (Figure 6.5c).

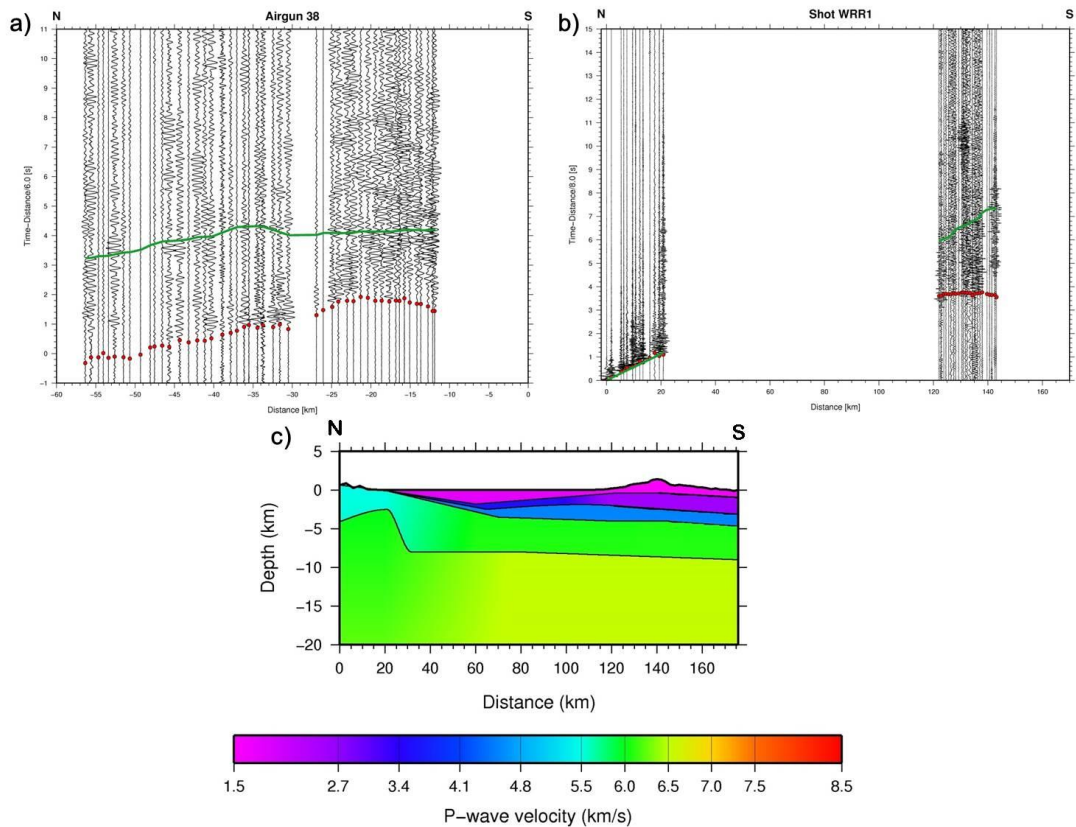


Figure 6.4. a) Seismic record section of airgun 38 b) Seismic record section of southern land shot of Turkey. Red dots show picked first arrival times. Green solid lines show calculated first arrival times based on the 2-D P wave velocity model c) 2-D P-wave velocity model.

The same velocity trend continues to the north beneath the Tuz Golu basin along the layer till 7 km thickness. P wave velocities are modelled as 6.0 – 7.1 km/s predominantly along a layer with a thickness of 38 km at the northern end of profile or beneath the Tuz Golu basin which is described as a lower crust. Along the lower crust, P wave velocities increase at the lower boundary of the layer compared to the upper boundary of this layer. P wave velocities are 6.3 km/s at the upper boundary and 7.1 km/s at the lower boundary between 100 and 150 km distances. Simultaneously, the layer thickness increases from 38 km to 45 km. The seismic rays (reflected phases) are fitted with a Moho depth of 38 km at the northern end of the profile which increases to 45 km towards to the southern end of the profile in an integration with an upper mantle P wave velocity of 7.8 km/s. Additionally, the PmP phase is observed and picked from the northern land shot at an offset of 190 – 270 km. An average P wave velocity is 6.5 km/s beneath Tuz Golu basin till 23 km depth.

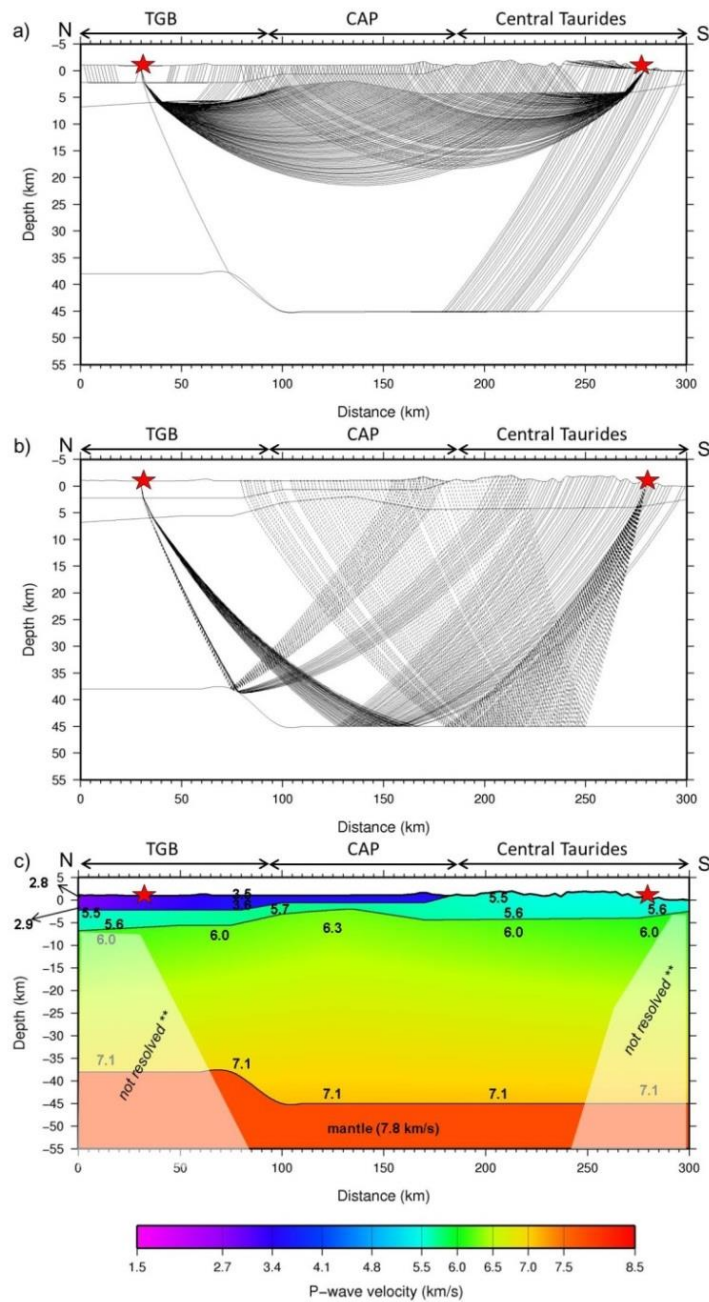


Figure 6.5. a) Ray diagram for refractions, b) Ray diagram for reflections, c) Final 2-D crustal P wave velocity model was produced after travel time modelling by using refractions and reflections are shown. Numbers denote P wave velocity, thick black line shows subsurface layers in the model and red stars indicate locations of land shots. Raypath with picked travel time is plotted with a thin solid line, raypath without picked travel time is plotted with a thin dashed line. ** = indicate shaded areas which are not resolved by seismic phases, but resolved by gravity modelling. TGB: Tuz Golu Basin, CAP: Central Anatolian Plateau.

P wave velocities show lateral changes from 6 km/s to 7.2 km/s at the upper boundary along the lower crust. A high velocity block (average P wave velocity is 6 km/s) between 120 -150 km offset, till 8 km thickness probably corresponds to ophiolite complex belong to Troodos Massif (Figures 6.6 – 6.13). Southward thickening of the sedimentary layer can be observed at an area between Cyprus and north of the Eratosthenes Sea Mount (ESM), 170 – 190 km offset (Figure 6.13). A final 2-D layered model for southern Cyprus resolved till a limited thickness due to lack of seismic stations between southern Turkey and Cyprus, along Mediterranean sea and no picking of reflected phases for the southern land shot of Turkey and airguns. Robustness of the unresolved area on the model was checked by gravity modelling (in chapter 8).

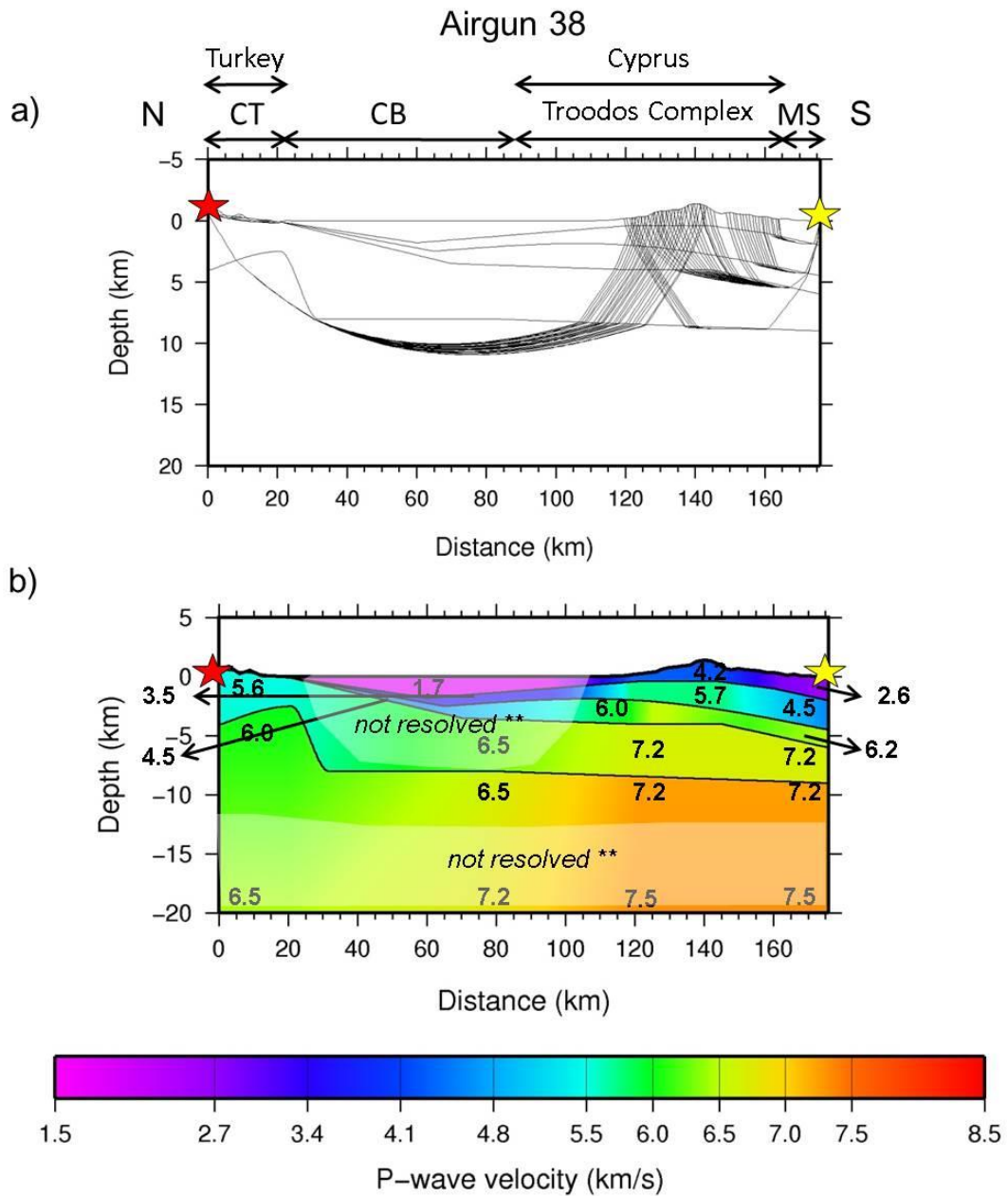


Figure 6.6. a) Ray diagram for refractions, b) Final 2-D crustal P wave velocity model between southern land shot and airgun shot 38 in the sea was produced after travel time modelling by using refractions. Numbers denote P wave velocity, thick black line shows subsurface layers in the model. Red and yellow stars indicate locations of land shot and airgun, respectively. Raypath with picked travel time is plotted with a thin solid line. ** = shaded areas not resolved by seismic phases, but resolved by gravity modelling. CT: Central Taurides, CB: Cilicia Basin.

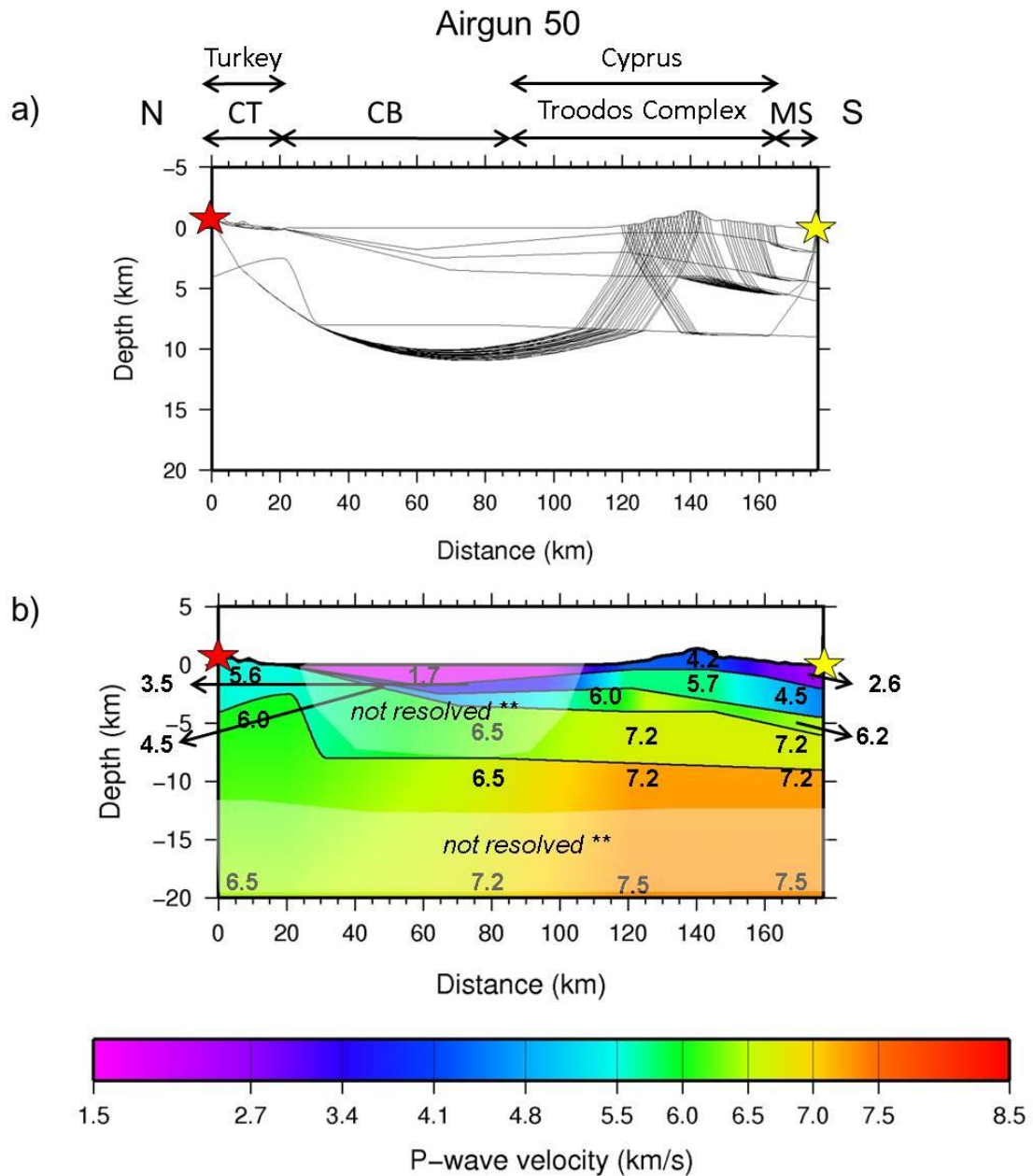


Figure 6.7. a) Ray diagram for refractions, b) Final 2-D crustal P wave velocity model between southern land shot and airgun shot 50 in the sea was produced after travel time modelling by using refractions. Numbers denote P wave velocity, thick black line shows subsurface layers in the model. Red and yellow stars indicate locations of land shot and airgun, respectively. Raypath with picked travel time is plotted with a thin solid line. ** = shaded areas not resolved by seismic phases, but resolved by gravity modelling. CT: Central Taurides, CB: Cilicia Basin.

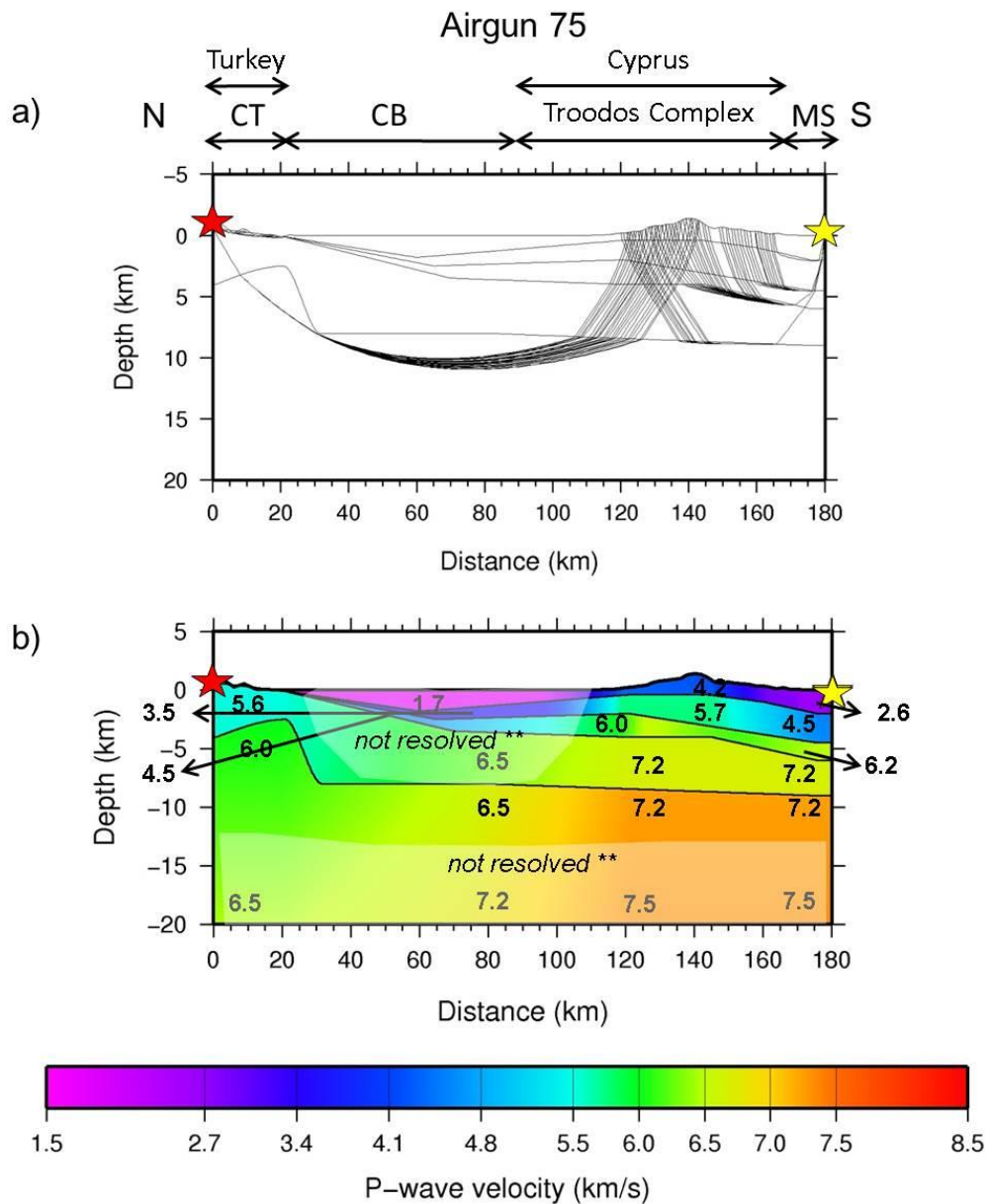


Figure 6.8. a) Ray diagram for refractions, b) Final 2-D crustal P wave velocity model between southern land shot and airgun shot 75 in the sea was produced after travel time modelling by using refractions. Numbers denote P wave velocity, thick black line shows subsurface layers in the model. Red and yellow stars indicate locations of land shot and airgun, respectively. Raypath with picked travel time is plotted with a thin solid line. ** = shaded areas not resolved by seismic phases, but resolved by gravity modelling. CT: Central Taurides, CB: Cilicia Basin.

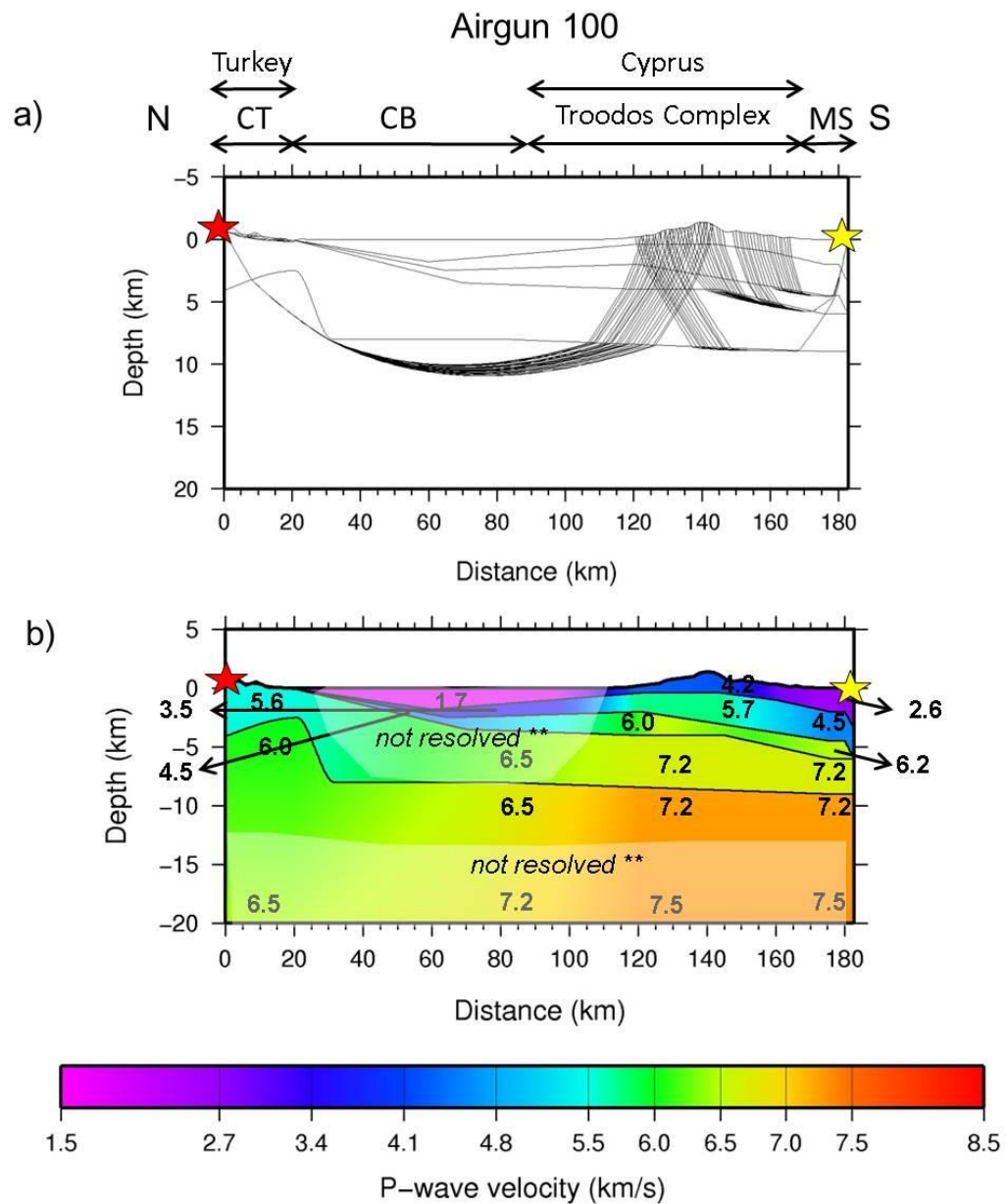


Figure 6.9. a) Ray diagram for refractions, b) Final 2-D crustal P wave velocity model between southern land shot and airgun shot 100 in the sea was produced after travel time modelling by using refractions. Numbers denote P wave velocity, thick black line shows subsurface layers in the model. Red and yellow stars indicate locations of land shot and airgun, respectively. Raypath with picked travel time is plotted with a thin solid line. ** = shaded areas not resolved by seismic phases, but resolved by gravity modelling. CT: Central Taurides, CB: Cilicia Basin.

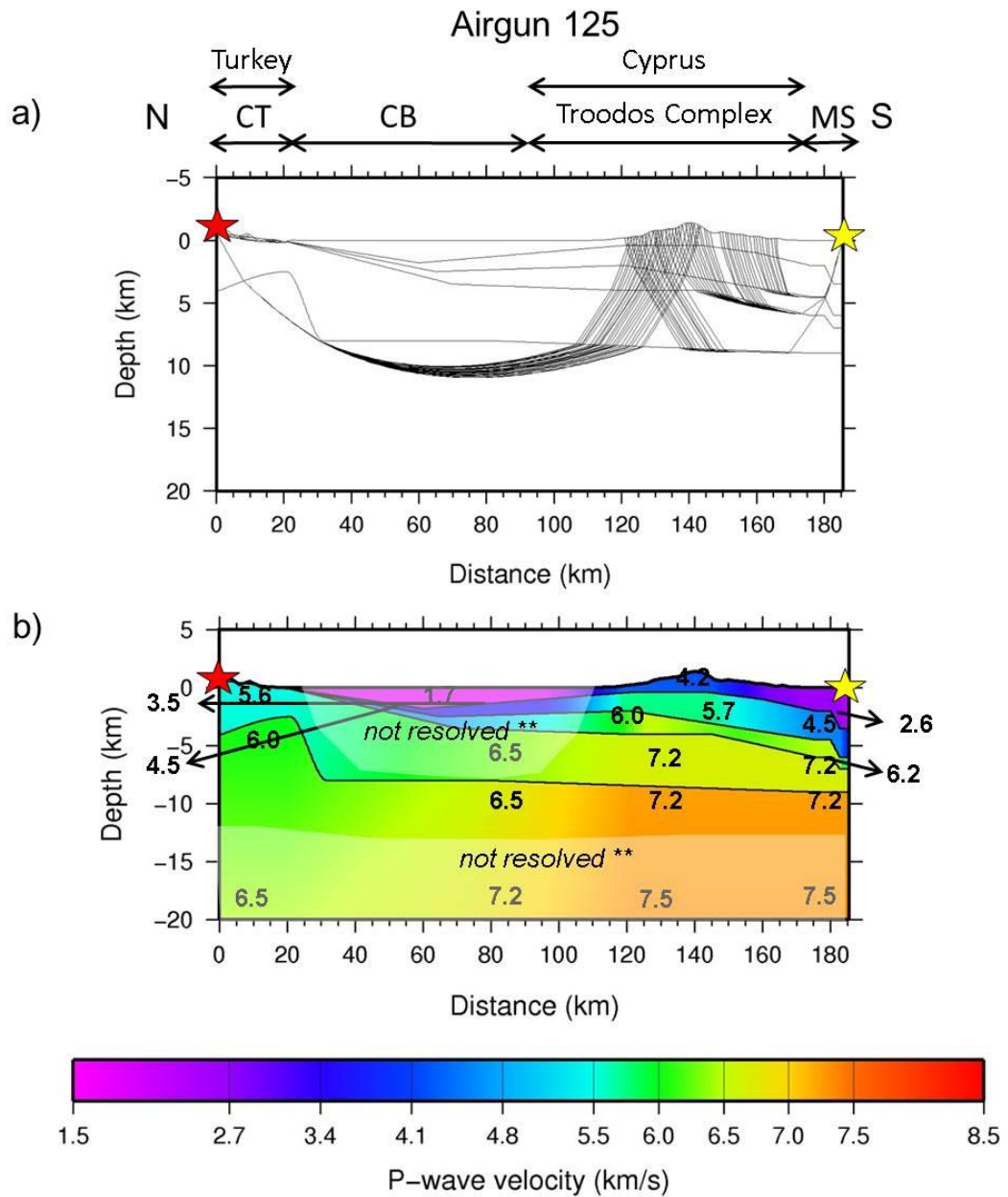


Figure 6.10. a) Ray diagram for refractions, b) Final 2-D crustal P wave velocity model between southern land shot and airgun shot 125 in the sea was produced after travel time modelling by using refractions. Numbers denote P wave velocity, thick black line shows subsurface layers in the model. Red and yellow stars indicate locations of land shot and airgun, respectively. Raypath with picked travel time is plotted with a thin solid line. ** = shaded areas not resolved by seismic phases, but resolved by gravity modelling. CT: Central Taurides, CB: Cilicia Basin.

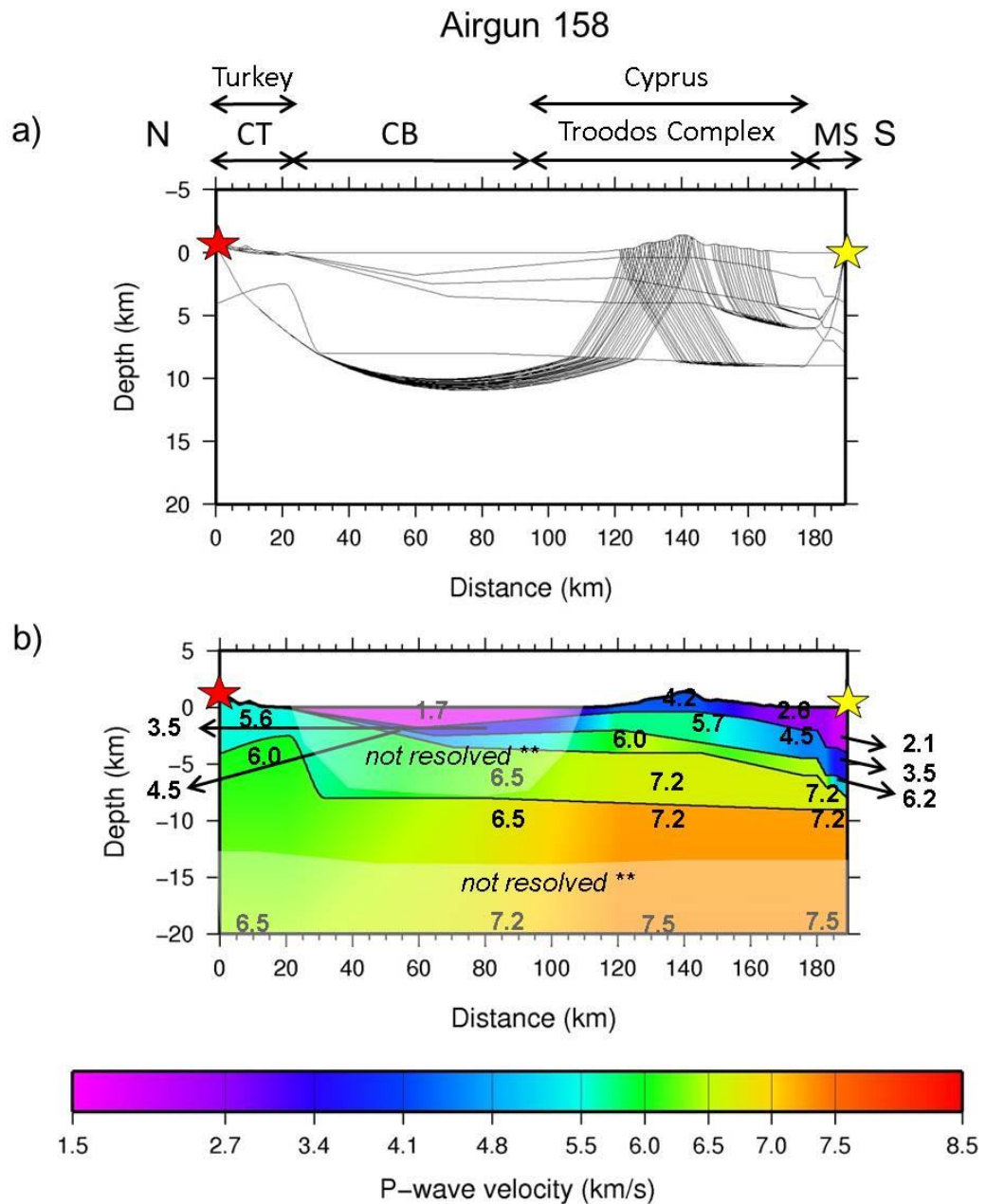


Figure 6.11. a) Ray diagram for refractions, b) Final 2-D crustal P wave velocity model between southern land shot and airgun shot 158 in the sea was produced after travel time modelling by using refractions. Numbers denote P wave velocity, thick black line shows subsurface layers in the model. Red and yellow stars indicate locations of land shot and airgun, respectively. Raypath with picked travel time is plotted with a thin solid line. ** = shaded areas not resolved by seismic phases, but resolved by gravity modelling. CT: Central Taurides, CB: Cilicia Basin.

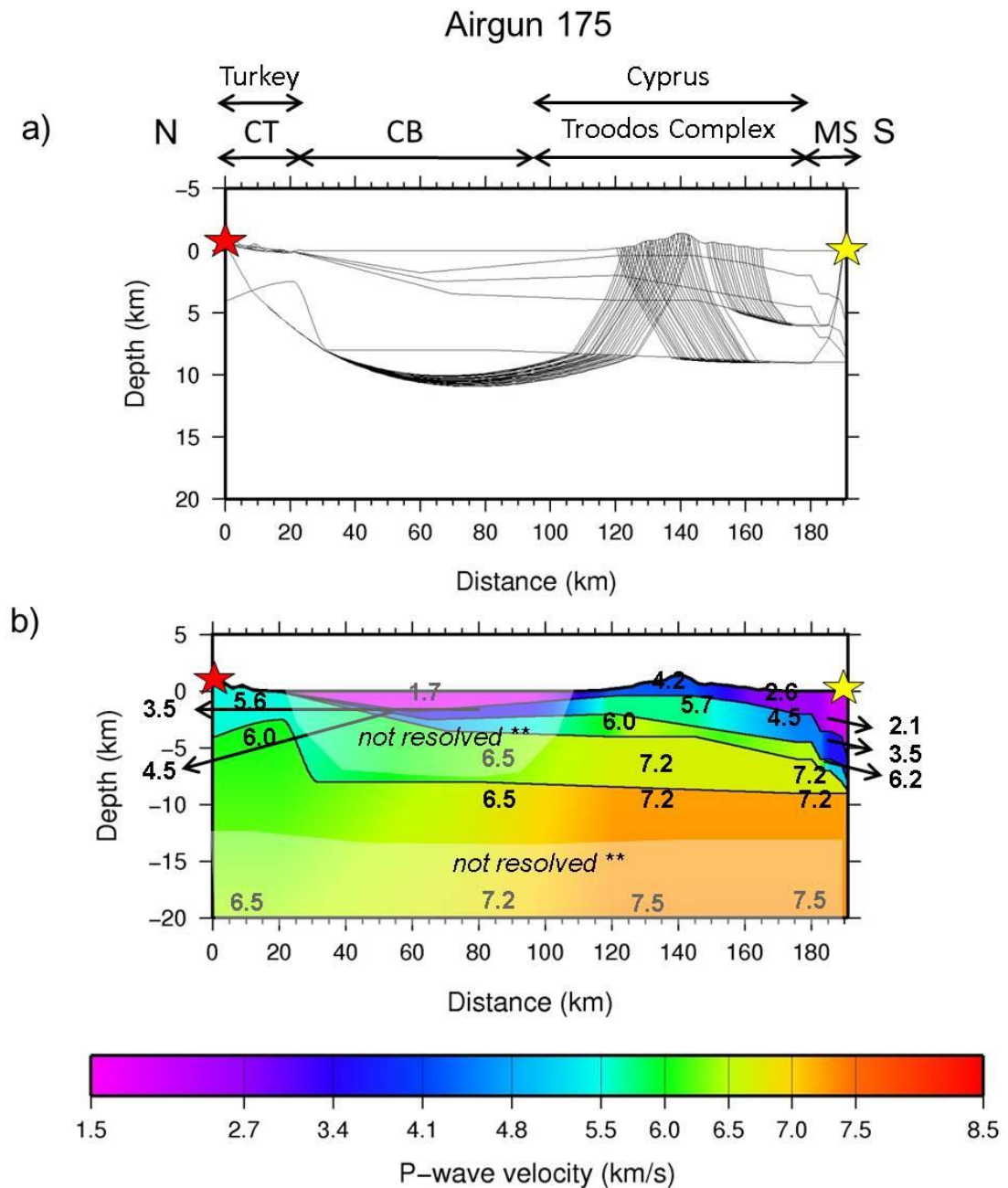


Figure 6.12. a) Ray diagram for refractions, b) Final 2-D crustal P wave velocity model between southern land shot and airgun shot 175 in the sea was produced after travel time modelling by using refractions. Numbers denote P wave velocity, thick black line shows subsurface layers in the model. Red and yellow stars indicate locations of land shot and airgun, respectively. Raypath with picked travel time is plotted with a thin solid line. ** = shaded areas not resolved by seismic phases, but resolved by gravity modelling. CT: Central Taurides, CB: Cilicia Basin.

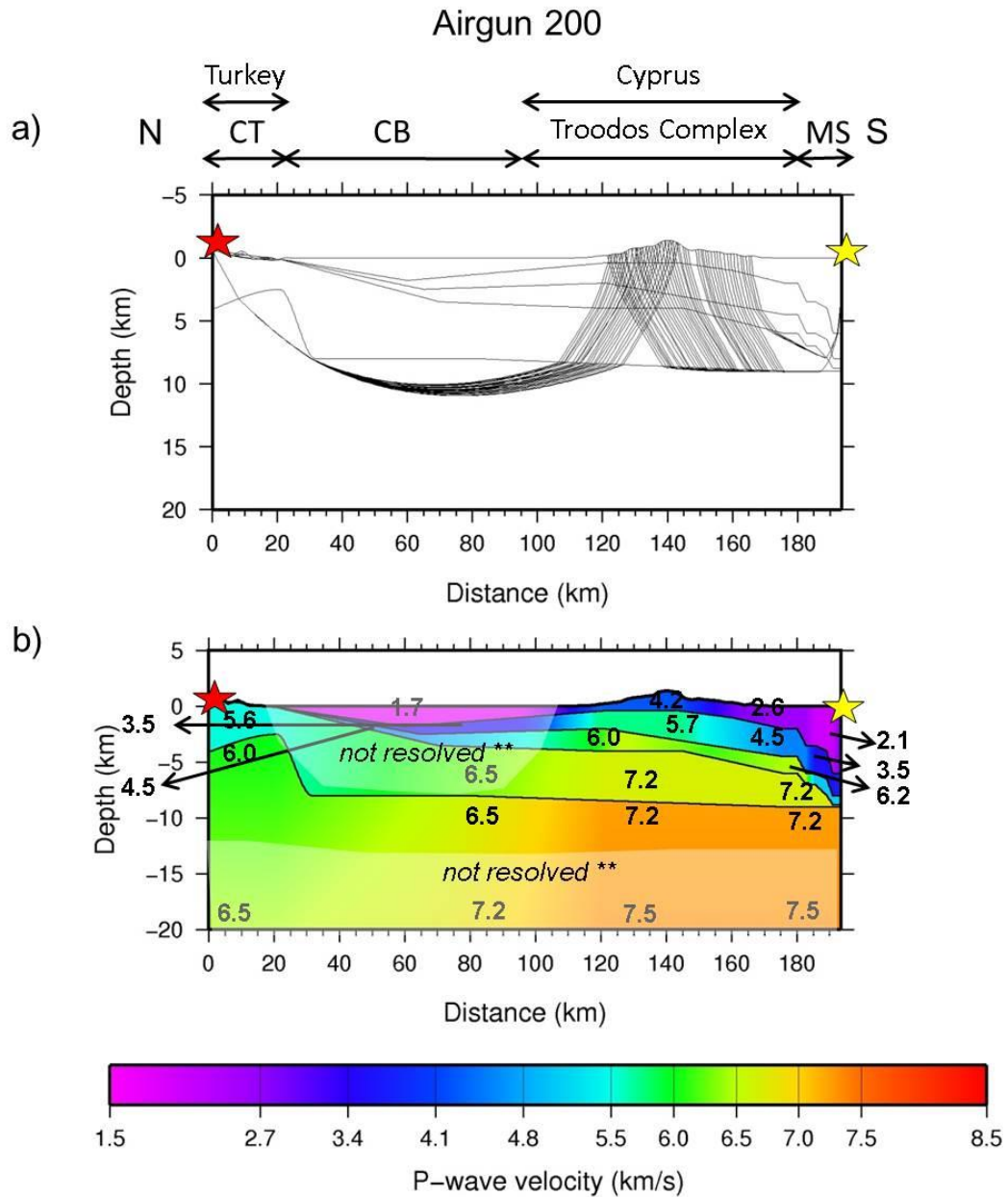


Figure 6.13. a) Ray diagram for refractions, b) Final 2-D crustal P wave velocity model between southern land shot and airgun shot 200 in the sea was produced after travel time modelling by using refractions. Numbers denote P wave velocity, thick black line shows subsurface layers in the model. Red and yellow stars indicate locations of land shot and airgun, respectively. Raypath with picked travel time is plotted with a thin solid line. ** = shaded areas not resolved by seismic phases, but resolved by gravity modelling. CT: Central Taurides, CB: Cilicia Basin.

7. RESULTS OF SYNTHETIC SEISMOGRAMS

Trace-normalized theoretical seismogram sections obtained with the finite-differences approach, proposed by Kelly *et al.* (1976), for the final 2-D crust models. The finite-difference approach gives an opportunity to make crude amplitude estimation which help us to check or arrival times of reflections from crust. In computing the finite-differences synthetic seismograms, the ray-trace model was digitized at a grid spacing of 40 m which allowed a dominant frequency for the source signal of 3.3 Hz, to be utilized for land shots and a grid spacing of 20 m which allowed a dominant frequency for the source signal of 2.7 Hz to be set for airguns.

There is good correlation between the observed and theoretical record sections. For example on the shot WRR1 (the southern land shot) record sections, first arrival seismic phase dominate out to about 200 km distance (Figure 7.1). On the shot WRR2 (the northern land shot), crustal phases observed at model between 130 and 270 km distances. First arrival seismic phases have a good correlation with synthetic seismograms till the end of the profile. The Pn phase is weak compared to later (crustal) phases (Figure 7.2). Some phases are not determined in the observed data. Thus some amplitude calculation was made in order to search for a final model. One advantage of finite-differences synthetic seismograms is that energy can be obtained at places where the ray theory does not estimate any arrival. This can be seen, for instance, on the theoretical record section of the shot WRR1 (the southern land shot) in which rays were not found for the refraction phases at model beyond 200 km distance and the reflection phases at model 50 and 200 km distances (Figure 7.1). Distance between the first seismic station and the first airgun (Airgun 38) is about 12 km. The last airgun (Airgun 200) has a distance approximately 28 km to the first seismic station. All synthetic seismogram sections for airguns indicate first seismic arrival phases which come from shallow layers till approximately 9 km depth layer. When total profile length from every airguns to the last seismic station and 2-D P wave velocity model are taken into consideration, all theoretical record sections can be interpreted as having a good correlation between the theoretical travel times and amplitudes of the first seismic arrival phase for each airgun records (Figures 7.3-7.11).

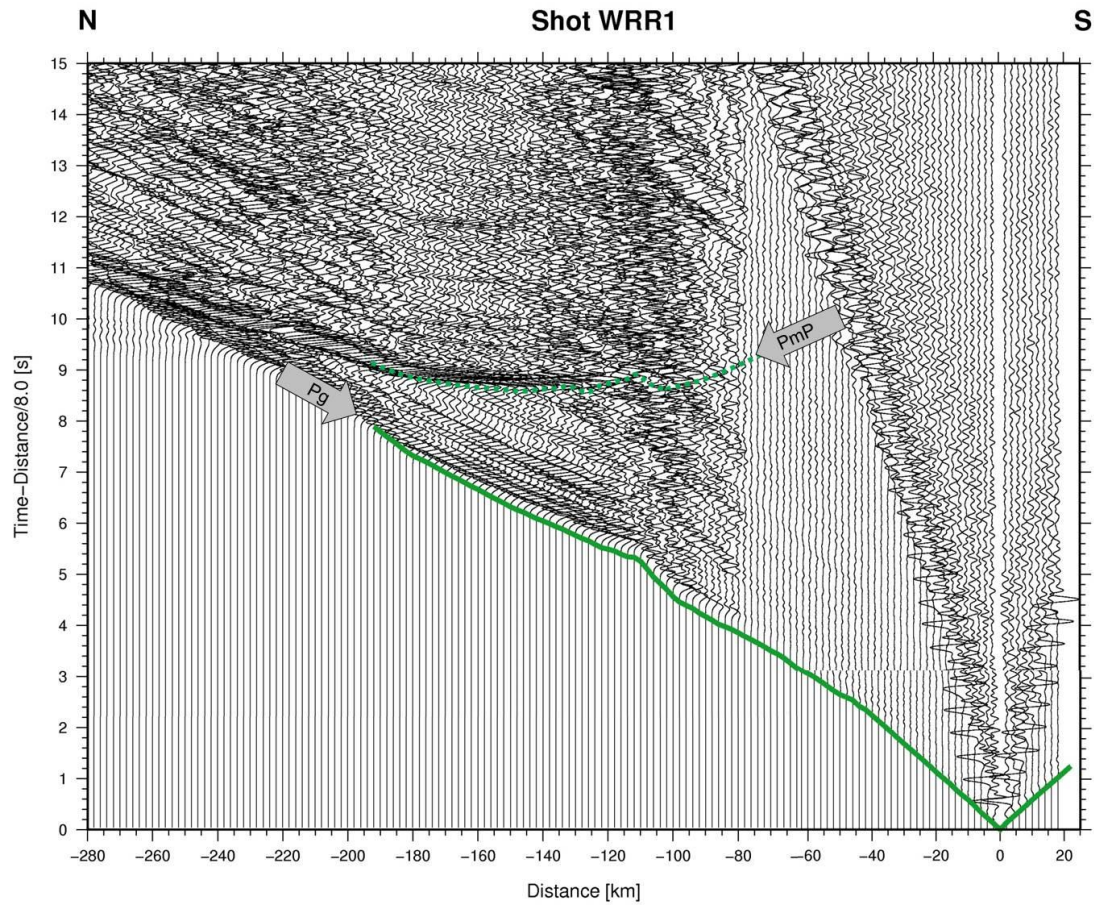


Figure 7.1. Synthetic seismogram section, computed with the finite-difference technique, for shot1 along WRR profile. Reduction velocity is 8 km/s for the record section denotes the vertical component of P wave motion in which each trace is normalized individually. Continuous and dashed green lines show phases computed from the model presented in Figure 6.5c.

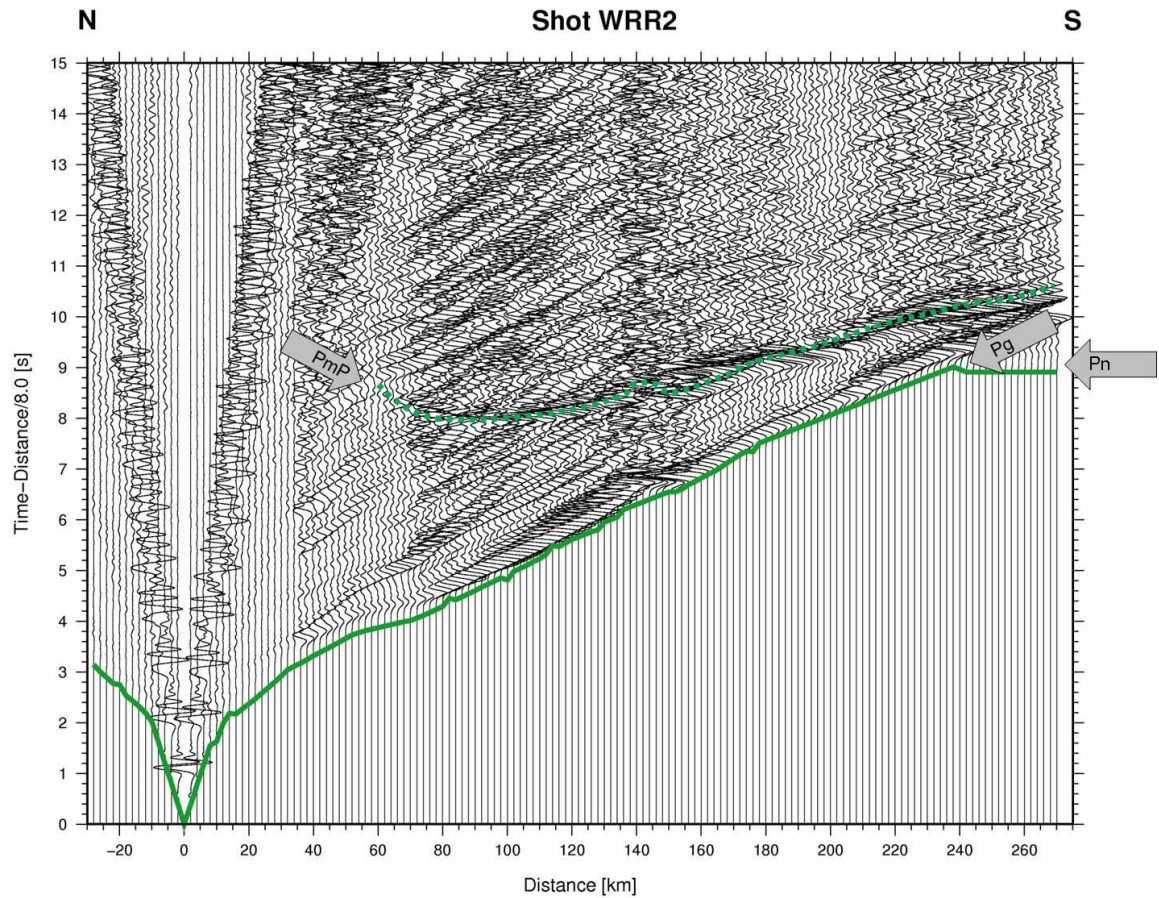


Figure 7.2. Synthetic seismogram section, computed with the finite-difference method, for shot2 along WRR profile. Reduction velocity is 8 km/s for the record section denotes the vertical component of P wave motion in which each trace is normalized individually. Continuous and dashed green lines show phases computed from the model presented in Figure 6.5c.

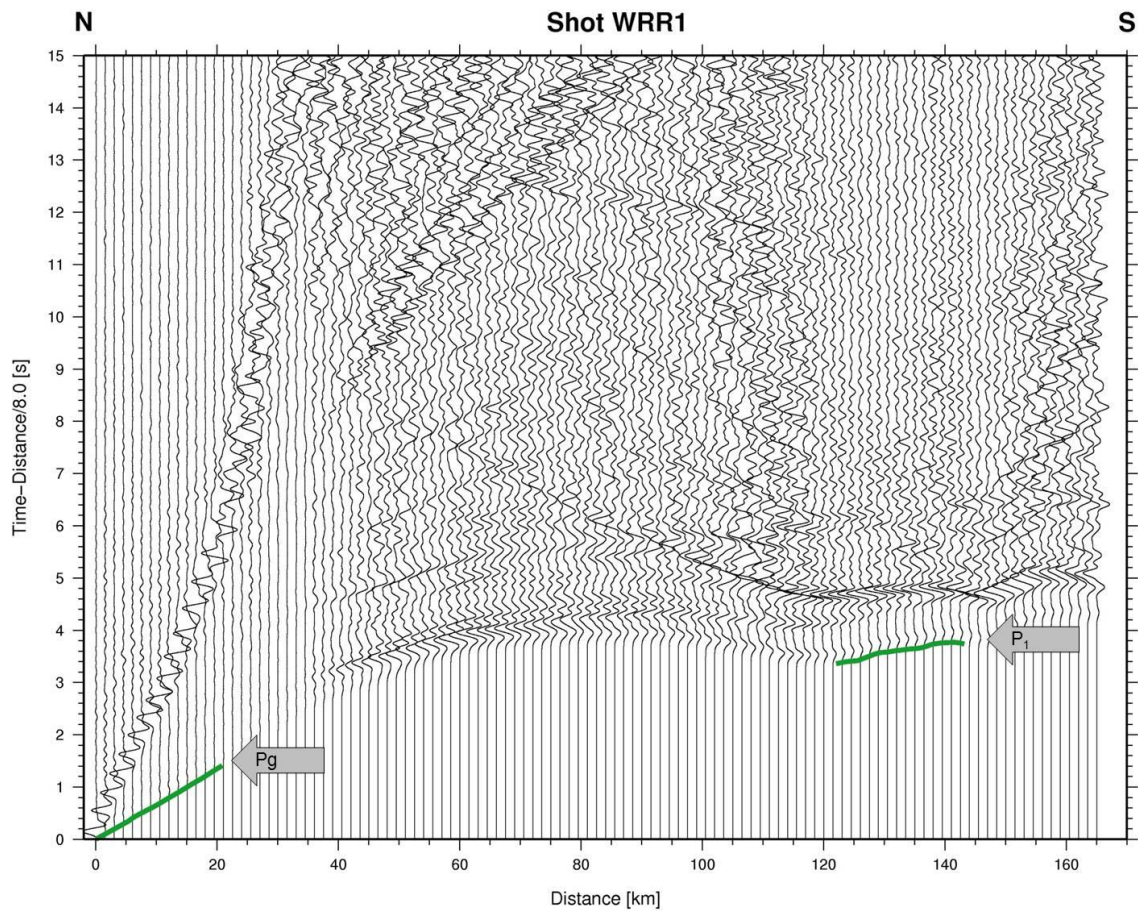


Figure 7.3. Synthetic seismogram section, computed with the finite-difference technique, for shot1 along WRR profile. Reduction velocity is 8 km/s for the record section denotes the vertical component of P wave motion in which each trace is normalized individually. Continuous green lines show phases computed from the model presented in Figure 6.6.

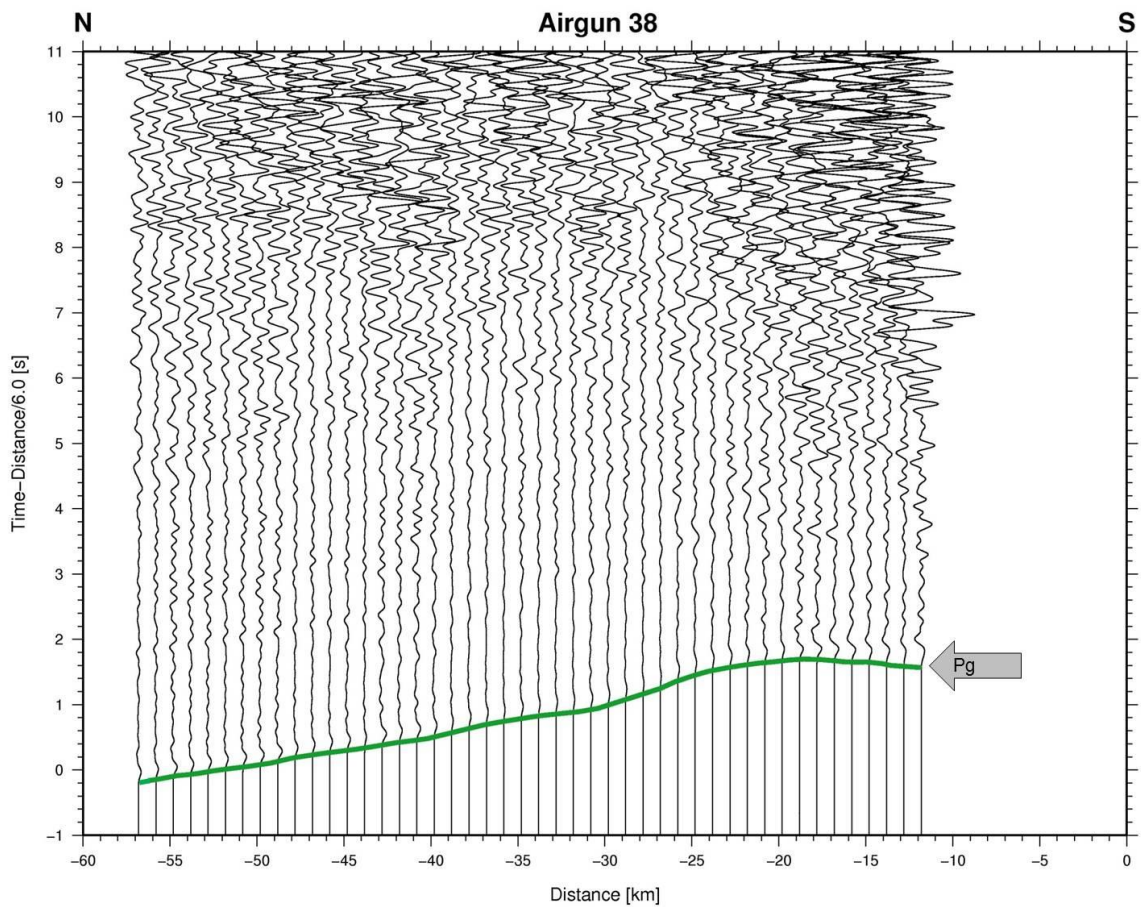


Figure 7.4. Synthetic seismogram section, computed with the finite-difference technique, for airgun 38 along WRR profile. Reduction velocity is 6 km/s for the record section denotes the vertical component of P wave motion in which each trace is normalized individually. Continuous green lines represent phases computed from the model presented in Figure 6.6.

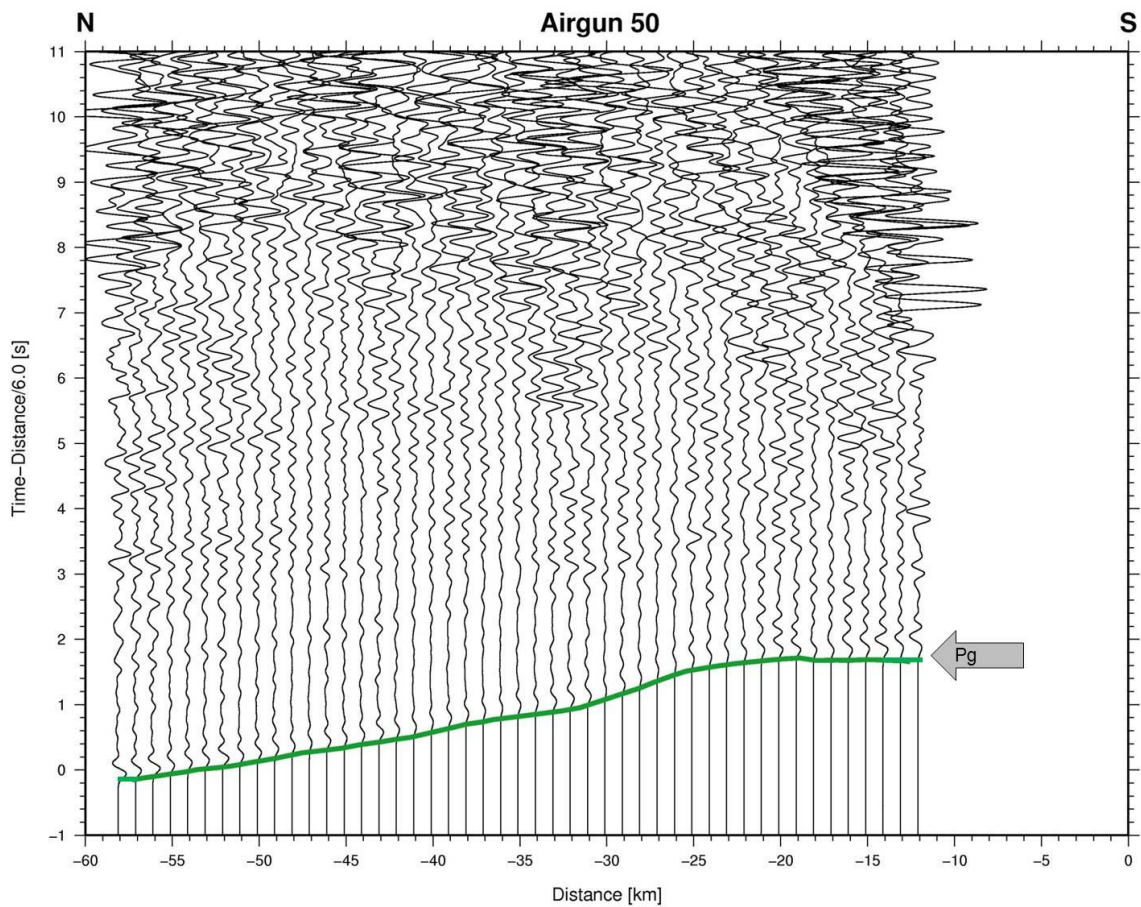


Figure 7.5. Synthetic seismogram section, computed with the finite-difference technique, for airgun 50 along WRR profile. Reduction velocity is 6 km/s for the record section denotes the vertical component of P wave motion in which each trace is normalized individually. Continuous green lines show phases computed from the model presented in Figure 6.7.

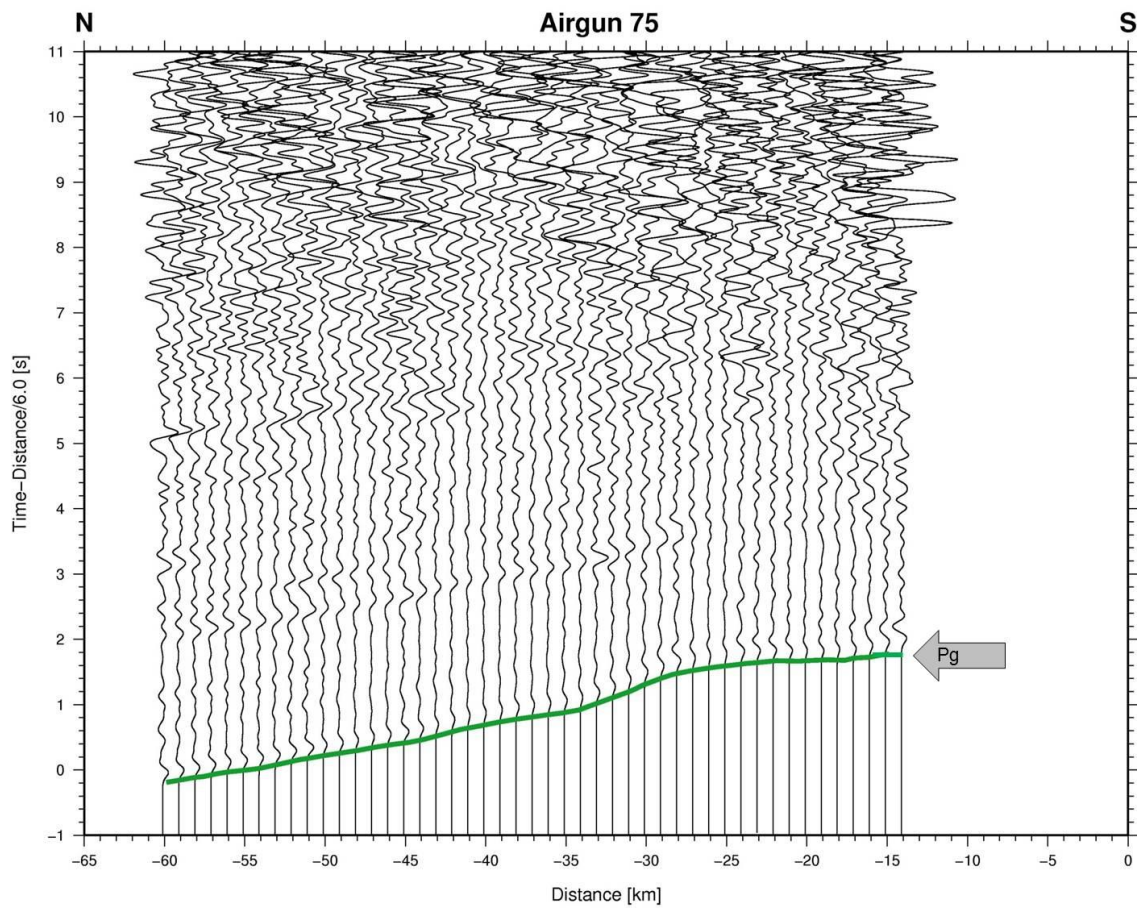


Figure 7.6. Synthetic seismogram section, computed with the finite-difference technique, for airgun 75 along WRR profile. Reduction velocity is 6 km/s for the record section denotes the vertical component of P wave motion in which each trace is normalized individually. Continuous green lines show phases computed from the model presented Figure 6.8.

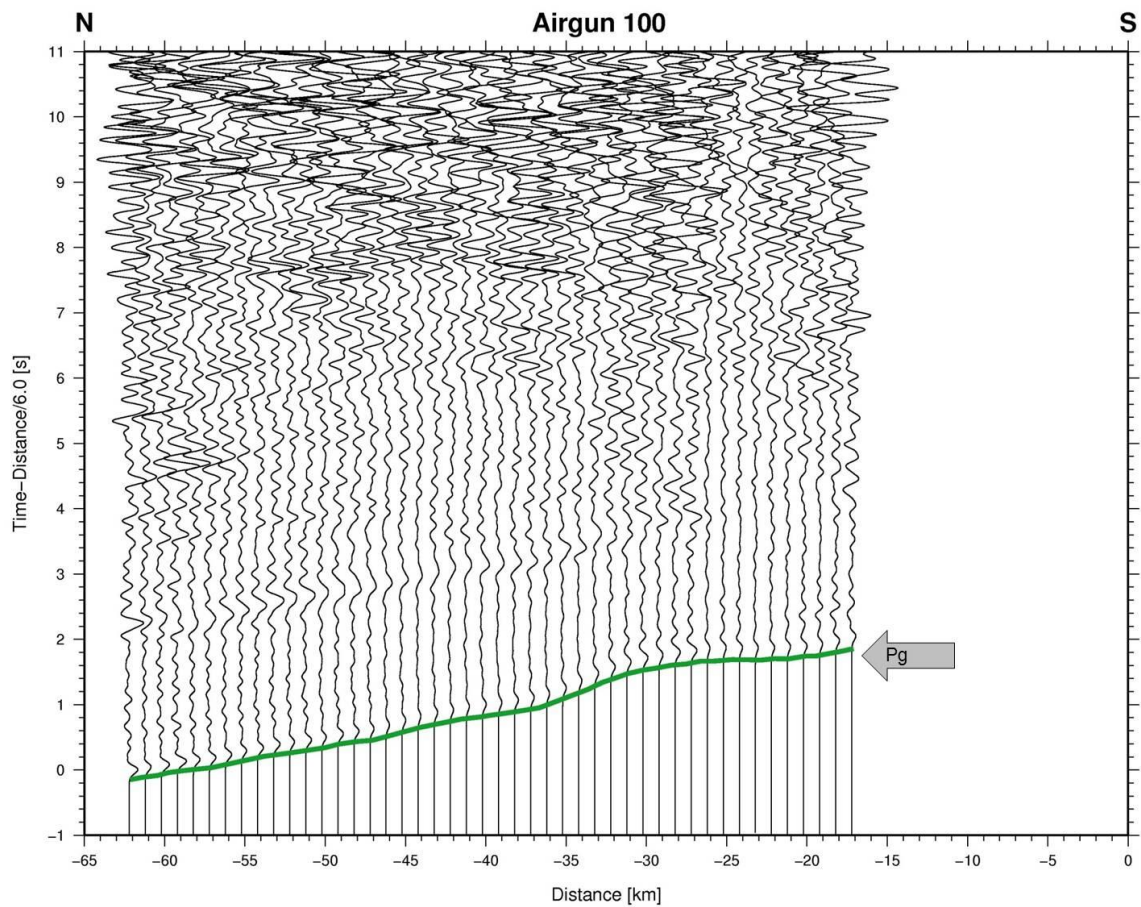


Figure 7.7. Synthetic seismogram section, computed with the finite-difference technique, for airgun 100 along WRR profile. Reduction velocity is 6 km/s for the record section denotes the vertical component of P wave motion in which each trace is normalized individually. Continuous green lines show phases computed from the model presented in Figure 6.9.

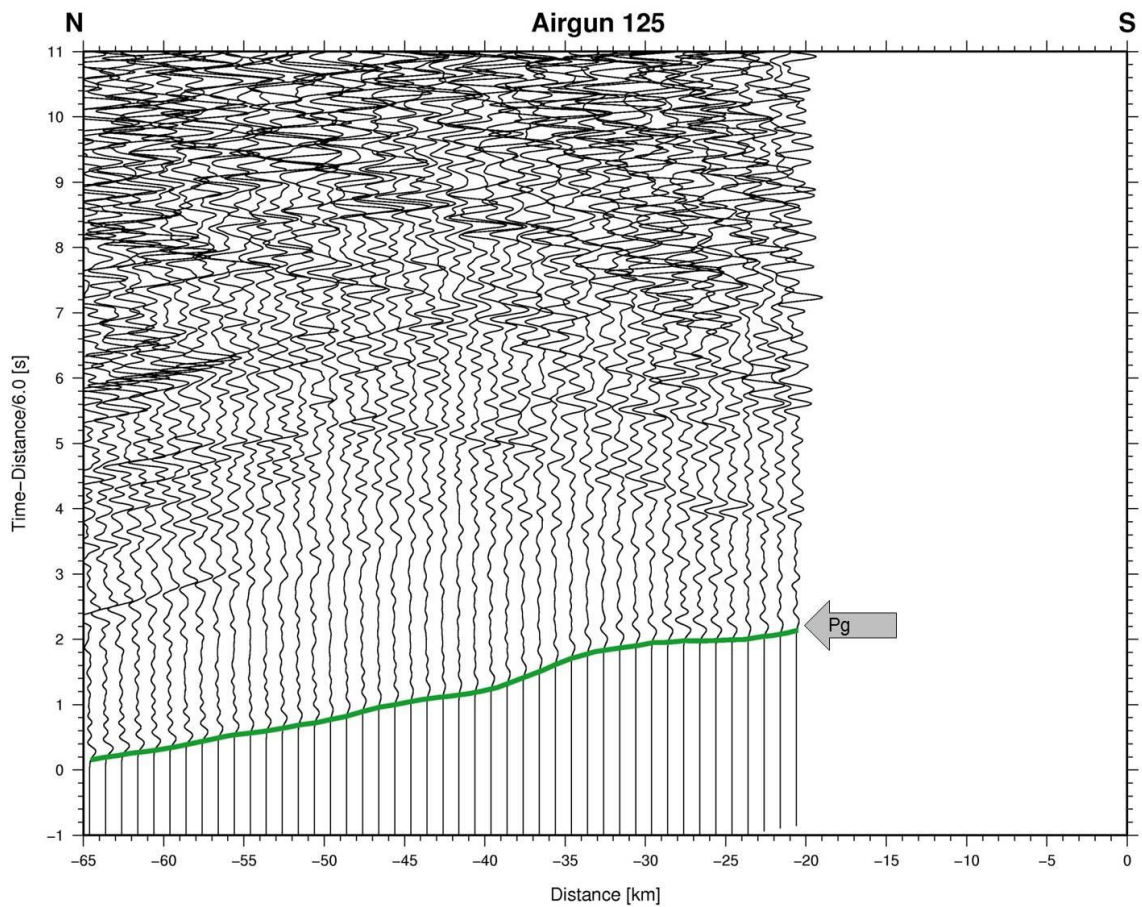


Figure 7.8. Synthetic seismogram section, computed with the finite-difference technique, for airgun 125 along WRR profile. Reduction velocity is 6 km/s for the record section denotes the vertical component of P wave motion in which each trace is normalized individually. Continuous green lines show phases computed from the model presented in Figure 6.10.

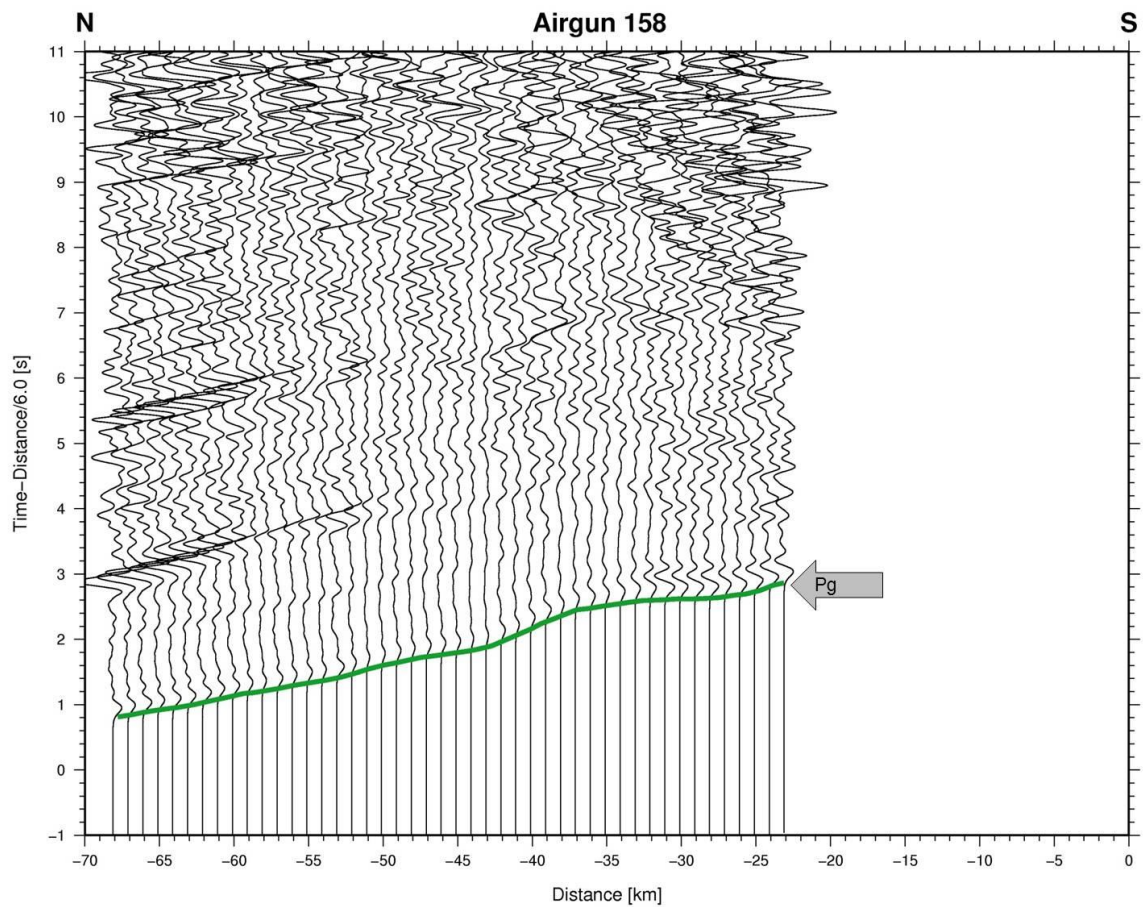


Figure 7.9. Synthetic seismogram section, computed with the finite-difference technique, for airgun 158 along WRR profile. Reduction velocity is 6 km/s for the record section denotes the vertical component of P wave motion in which each trace is normalized individually. Continuous green lines show phases calculated from the model presented in Figure 6.11.

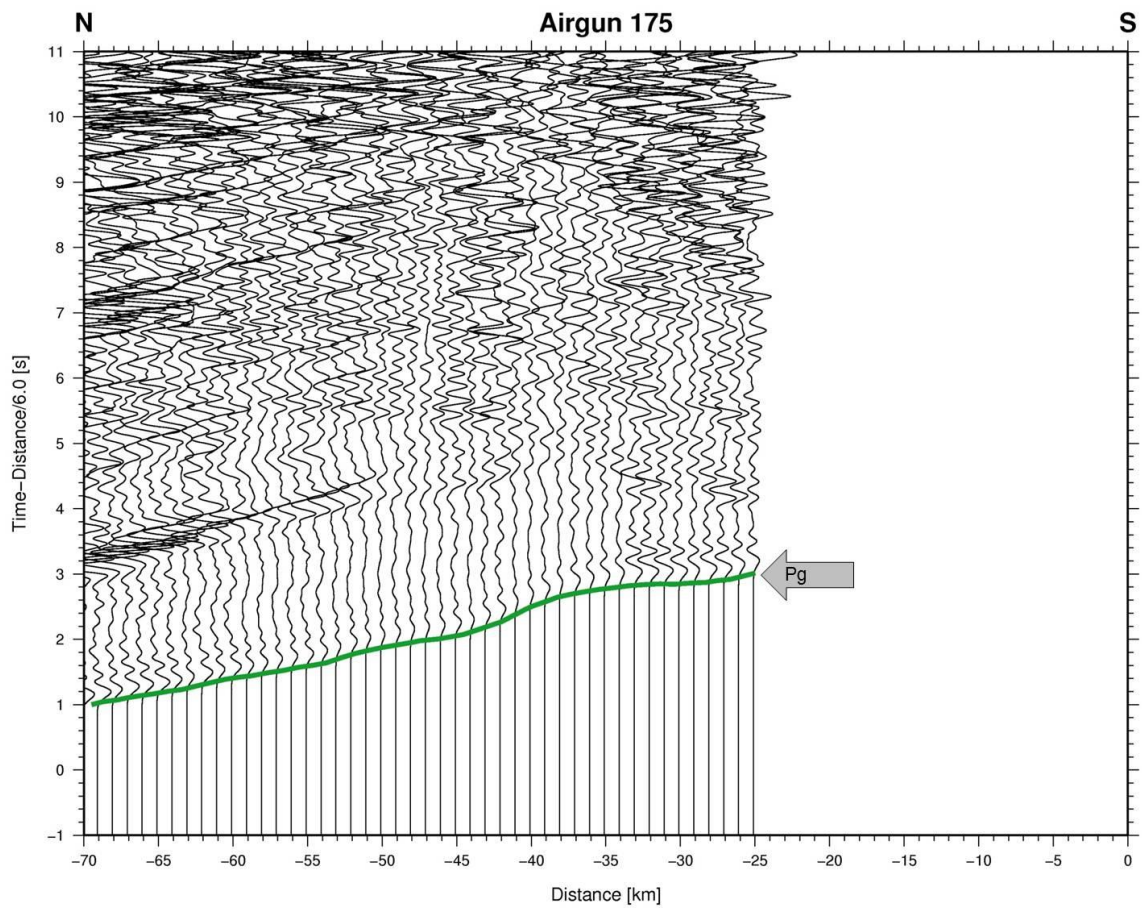


Figure 7.10. Synthetic seismogram section, computed with the finite-difference technique, for airgun 175 along WRR profile. Reduction velocity is 6 km/s for the record section denotes the vertical component of P wave motion in which each trace is normalized individually. Continuous green lines show phases computed from the model shown in Figure 6.12.

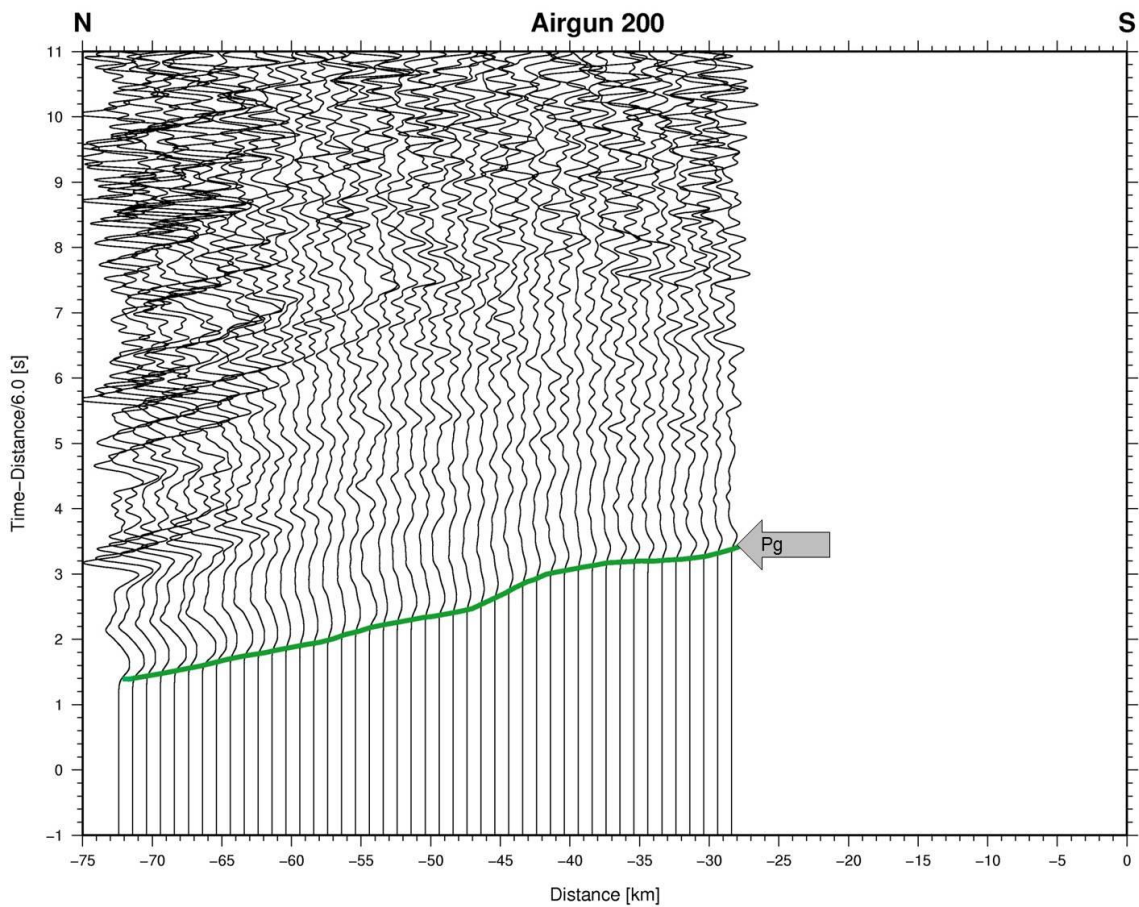


Figure 7.11. Synthetic seismogram section, computed with the finite-difference technique, for airgun 200 along WRR profile. Reduction velocity is 6 km/s for the record section denotes the vertical component of P wave motion in which each trace is normalized individually. Continuous green lines show phases computed from the model presented in Figure 6.13.

8. RESULTS OF GRAVITY MODELLING ALONG THE WRR PROFILES

Gravity modelling was done for checking robustness of the final 2-D layered P wave velocity models. For gravity modelling, obtained P wave velocities were converted into densities by using the Birch law (Nafe and Drake, 1975; Birch, 1961). Birch law is an empirical relationship which defines that velocity is an approximately linear function of density for materials having a common mean atomic weight (Birch, 1961).

$$\rho = 0.352 + 0.3788 * V_p \quad (8.1)$$

Densities related to the P wave velocity models obtained from the 2-D modelling of the seismic profiles in Turkey and southern Cyprus are given at tables 8.1 and 8.2, respectively.

Table 8.1. Units of the final 2-D P wave velocity model and the corresponding densities for seismic profile in Turkey. The corresponding density values were derived by using equation 8.1.

Depth (km)	V _p (km/s)	Density (g/cm ³)
Sediments beneath Turkey	2.8 – 3.6	1.71
Layer between -2 and 6.8 km	5.5 – 5.8	2.43
Layer between 2.5 and 45 km	6.0 – 7.1	2.73
Upper mantle	7.8	3.3

Table 8.2. Units of the final 2-D P wave velocity model and the corresponding densities for seismic profile in southern Cyprus. The corresponding densities were derived by using equation 8.1.

Depth (km)	Vp (km/s)	Density (g/cm ³)
First layer beneath Turkey	5.5 – 5.8	2.43
Sediments beneath Cilicia Basin (Aksu et al., 2005)	1.7 – 5.2	1.0 – 2.3
Sediments beneath Cyprus	4.2 – 6.2	1.95 – 2.7
Sediments beneath Mediterranean, south Cyprus	2.5 – 6.0	1.3 – 2.63
Upper crust beneath Cilicia basin and Cyprus	6.0 – 6.6	2.63 – 2.86
Lower crust	6.0 – 7.5	2.73 – 3.2
Upper mantle	8.0	3.38
Subducting plate (Ergun et al., 2005)	6.8	2.92

A 2-D polygon model cross-sections along the profiles, based on the formula of Talwani *et al.* (1959) with finite-length strike (Cady, 1980) were used with the derived densities to obtain theoretical bouguer gravity anomaly values. The vertical component of gravitational attraction V , due to a whole polygon, is given by

$$V = 2G\rho \sum_{i=1}^n Z_i \quad (8.2)$$

where G is the universal constant of gravitation and ρ is the density of the body.

The summations are made over the n sides of the polygon. The misfit between observed and calculated gravity values can be minimized by systematic variations of the number, locations of vertices and density of the polygon. The gravity model has to be updated and rerun when P wave velocity model has changed and vice versa. A final 2-D P wave velocity and gravity models which are jointly constrain the crustal model through an optimum fitting of both the gravity data and seismic data.

The calculated gravity values show a good agreement with the observed gravity anomalies along profiles (Figures 8.1a and 8.2a). The observed gravity data were compiled from Gass and Masson-Smith (1963), Makris and Wang (1994), Ergün *et al.* (2005), Aydemir and Ateş (2006) and General Directorate of Mineral Research and Exploration (MTA). There is gravity low over the Taurus Mountains and Anatolian plateau in southern Turkey of the Turkish mainland (Figure 8.1a). Cyprus has a high positive bouger anomaly values between 100 and 175 mgal. The maximum anomaly pick (up to approximately 180 mgal) corresponds to the Troodos complex which runs parallel to the Kyrenia range. The observed positive gravity anomaly relatively falls off at the northern part of the Cyprus (Cilicia basin). The high density rocks (around 3.1), which appear to have produced this large anomaly, beneath Troodos complex in Cyprus area at shallow depths (around 8 km depth) have a correlation between the ultrabasic rocks of the Troodos Plutonic Complex and the high-density material causing the main strong positive anomaly (Figure 8.2 a,b). We observed gravity low between Eratosthenes and Cyprus. The observed gravity values increases between Turkey and Cyprus, across the Cilicia basin, this high gravity value is mainly caused by crustal thinning. It reaches to about 30 km depth at the southern end of the profile (Figure 8.2b). The gravity low associated with the Taurus Mountains and the Anatolian plateau in southern Turkey would be expected for continental crust in an elevated, mountainous area, even with a modest isostatic positive contribution (Ergün *et al.*, 2005). An important point about to minimize misfit between calculated and observed gravity values can be attributed to inserting of the sediment layers beneath Cilicia basin as Aksu *et al.* (2005) suggested and northward dipping subducting plate between southern land shot in Turkey and airguns as Ergün *et al.* (2005) suggested. The model of Ergün *et al.* (2005) proposed a subducting plate with a density of 3.0 g/cm^3 . The analysis of the gravity data presented in this study predicts shallow subducting slab (around 50 km depth) with a density of 2.92 g/cm^3 .

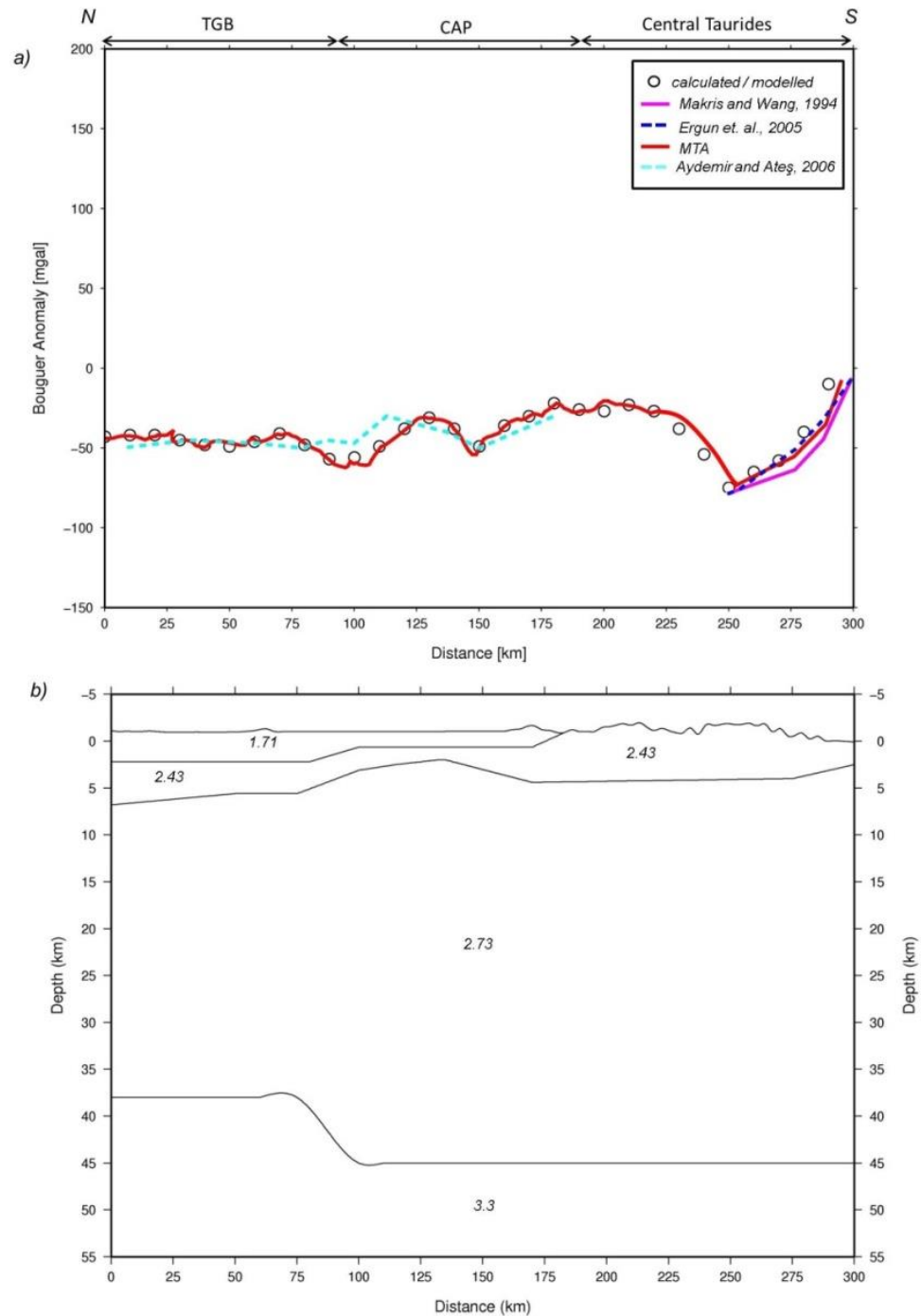


Figure 8.1. a) The calculated gravity values (circles) compared to observed gravity values (Pink solid line shows gravity values from Makris and Wang, 1994; blue dashed line shows gravity values from Ergün *et al.*, 2005; red solid line shows gravity values obtained from General Directorate of Mineral Research and Exploration (MTA); turquoise blue

dashed line shows gravity values from Aydemir and Ateş, 2006). b) Final gravity model.

Numbers denote density in g/cm^3 .

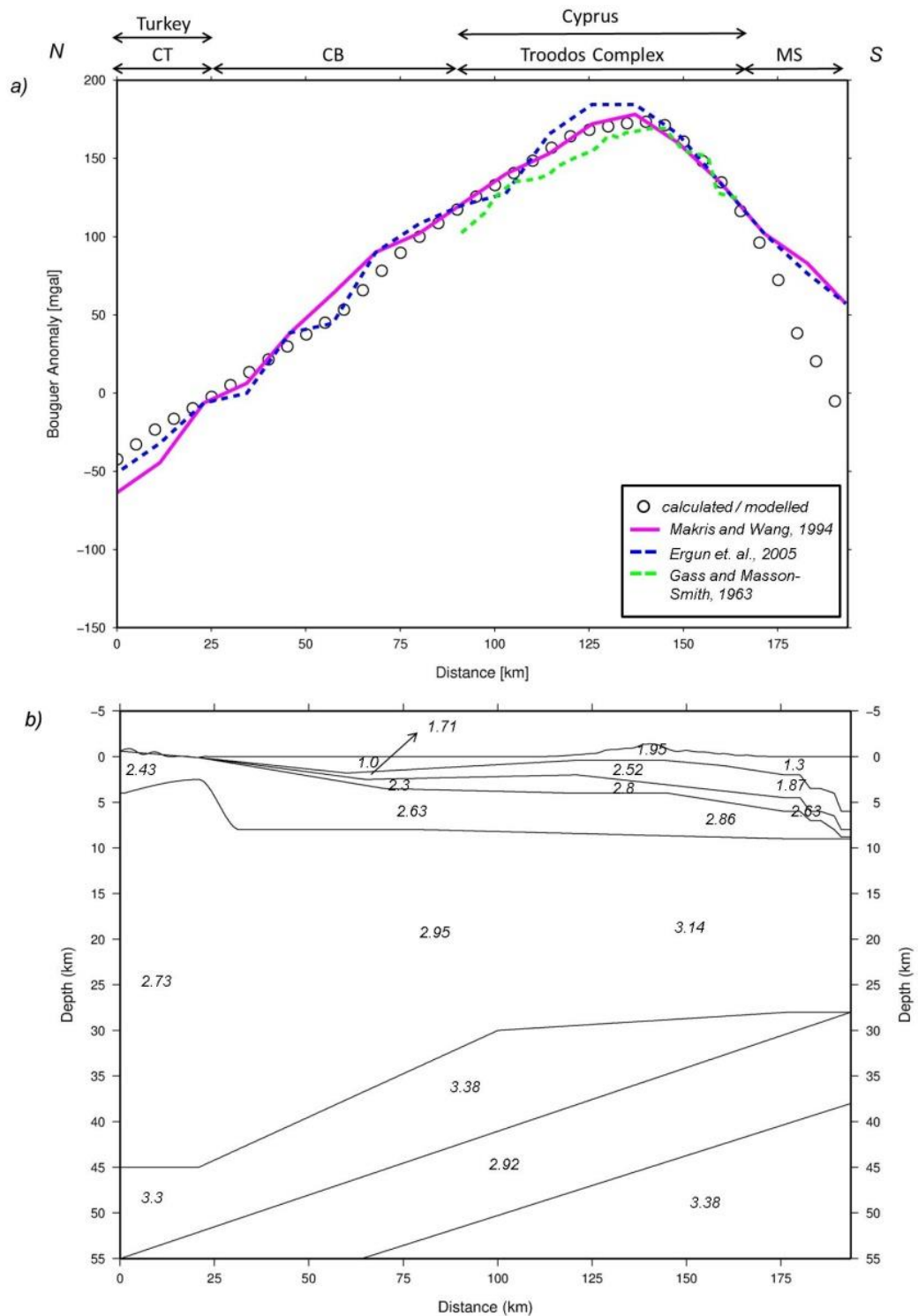


Figure 8.2. a) The calculated gravity values (circles) compared to observed gravity values (Pink solid line shows gravity values from Makris and Wang, 1994; blue dashed line

shows gravity values from Ergün *et al.*, 2005; green dashed line shows gravity values from Gass and Mason Smith, 1963). b) Final gravity model. Numbers denote density in g/cm^3 .

9. DISCUSSION AND CONCLUSIONS

Changes in crustal thickness between Tuz Golu and Anamur in Turkey and in southern Cyprus are observed by processing the WRR (Wide Angle Seismic Refraction/Reflection) data and gravity modelling. Some evidences observed some variations in the geometry of the lower crust topography and the simultaneous change of crustal velocities along WRR profiles. Lower crustal velocities increases laterally from Turkey to Cyprus. The northern part has a lower crustal thickness of about 38 km, lower crustal P wave velocities of 6.0-7.1 km/s. The southern part has a crustal thickness of 45 km, lower crustal P wave velocities of 6.0-7.5 km/s. The crustal thickness can be interpreted based on geologic information and tectonic formations as the boundary between the Central Anatolian Crystalline Complex in the north and the Central Taurus platform in the south (Görür *et al.*, 1998b; Okay, 2000; Clark and Robertson, 2002; Okay, 2008; Dilek and Sandvol, 2009). These crustal units are separated by the Bozkır nappes (Figure 2.2).

The crustal thickness variation and velocity distribution beneath Turkey and Cyprus show a type of continental crust. The maximum crustal thickness of 45 km beneath southern Turkey with an upper mantle P wave velocity of 7.8 km/s is observed by combined processes of the WRR and the gravity data. The decreasing thickness of the sedimentary cover beneath CAP (Central Anatolian Plateau), a change in Moho depth from 38 km to 45 km, a laterally increasing P wave velocity in the lower crust and the simultaneous thickening of the lower crust suggest a lateral change in crustal structure. These results are in a good correlation with some previous studies. Luccio and Pasyanos (2007) derived crustal structures along profiles by analysis of surface wave dispersion curves. Crustal thickness is thinning from south of Turkey to Cyprus like observing our gravity modelling result. Anisotropic Pn tomography was performed by Mutlu and Karabulut (2011) for whole Turkey including the study area. Pn velocities, are correlatable when we compare our profile between Cihanbeyli and Anamur. Mutlu and Karabulut (2011) revealed that Pn velocity is 7.9 km/s for northern part of our profile and 7.7 km/s

for southern part of our profile. Additionally, crust is thicker beneath southern Turkey compared to Central Anatolia as we observed after seismic modelling. Gans *et al.* (2009) conducted Pn tomography and their model indicates thinner crust beneath Central Anatolia compared to southern Turkey. Furthermore, two receiver function analysis studies (Vanacore *et al.*, 2013 ; Tezel *et al.*, 2013) are remarkable to compare and correlate with our results. Vanacore *et al.* (2013) proposed crustal thickness values are varying from 31 km to 45 km for Central Anatolia. In this region, the values may not constrain well due to the scarcity of seismic stations. The decrease in gravity across the Cilicia Basin is mainly originated by a crustal thickening of 45 km beneath the Anatolian plateau. Conversely, an average value of the crustal thickness of 37 km in this region was suggested by Vanacore *et al.* (2013), the gravity data is not coherent with this value. The gravity data propose a crustal thickness of approximately 45 km. Another receiver function analysis was performed by Tezel *et al.* (2013). They proposed a Moho depth of 36 km - 40 km for Tuz Golu basin and the southern boundary of the Central Anatolia. This result has a good agreement especially for northern end of our profile. At the northern end of the profile in Turkey the Moho becomes shallower to 38 km depth in order to fit the gravity data.

MacKenzie *et al.* (2006) performed seismic refraction experiment by using an IANGASS project data. 160 km seismic wide-angle reflection/refraction and gravity profile were modelled. The profile was constructed parallel to the Troodos ophiolite complex. 2-D tomographic velocity model and 2-D velocity model (obtained from ray tracing) of the Troodos ophiolite was revealed and high P wave velocities values were observed beneath Troodos Ophiolite like our final 2-D P wave velocity model and no seismic rays observed from deep layers beneath 15 km over Troodos complex (Figures 6.2 – 6.9). Furthermore, gravity modelling was conducted by MacKenzie *et al.* (2006). For gravity modelling, different calculation approach was used. Initial anomaly densities were obtained by combination of 4 different arguments like empirical formula except Birch law, borehole cores, Shelton's previous density modelling and modern oceanic analogues. Our profile crossed the same local area as the IANGASS profile crosses. The results are quite similar, gravity anomaly observed as approximately 180 mgal at our study IANGASS gravity result shows approximately 200 mgal at the same local site. One of the calculated positive gravity anomalies occur over Cyprus. The axis of maximum anomaly lying over the Troodos massif and parallel to the trend of the Kyrenia range. Investigation of the

anomaly may indicate that it is due to an extensive slab of high density rock which underlies the Cyprus area at shallow depth. This result could be correlated with a previous study performed by Gass and Masson Smith (1963). According to their approach geological and geophysical evidences suggest that this slab was once part of the upper mantle underlying an oceanic area between the African and Eurasian continents. It is suggested that when the continental shields approached to each other during the Alpine orogeny this slab of mantle was underthrust by the edge of the African shield and thereby raised to its position in the crust (i.e. observed high density rocks at very shallow depths (around 7.5 km) beneath Troodos complex, Cyprus.) (Gass and Masson-Smith, 1963). After personal communication with Esen Arpat, we correlated the high density rocks (around 3.1), which appear to have produced this large anomaly, beneath Troodos complex in Cyprus area at shallow depths (around 8 km depth) in our model with the ultrabasic rocks of the Troodos Plutonic Complex and the high-density material causing the main strong positive anomaly. A further aspect of that the Troodos ophiolite in the island of Cyprus exemplifies a late Cretaceous spreading axis (mid-ocean ridge) that has been uplifted because of its localizing on the overriding Anatolian plate at the Cyprus arc and subduction to the south of the Eratosthenes Seamount (Robertson, 1998) and it may be correlated with a high gravity anomalies in Cyprus (Figure 8.2). The low bouguer gravity anomaly values were observed between Cyprus and Eratosthenes (till airgun 200). This result has an agreement with the study conducted by Ergün *et al.*, 2005. It signs the plate boundary and is caused by thick sediments that are the remnants of an accretionary wedge sitting in the former trench (Ergün *et al.*, 2005).

The results of the 2-D crustal models show good correlation with previous studies, existing geological background and tectonic history for the Anatolian plateau and Cyprus. The detailed properties about P wave velocity and density along profile were revealed. Misfit between observed and theoretical travel times and also between observed and theoretical bouguer gravity anomalies were minimized by inserting a northward dipping subducting plate beneath Cyprus. To enlarge and develop the constraints on the deeper part of the subducted plate, additional investigations are necessary. Especially, it would be a big necessity to install seismic stations in the northern part of Cyprus, southern Turkey and also OBS stations in Mediterranean sea between southern Turkey and northern Cyprus for another wide angle experiment.

REFERENCES

Aksu, A.E, T.J. Calon, J. Hall, S. Mansfield, D. Yaşar, “The Cilicia–Adana basin complex, Eastern Mediterranean: Neogene evolution of an active fore-arc basin in an obliquely convergent margin”, *Marine Geology*, Vol. 221, pp. 121–159, 2005.

Aksu, A.E, T.J. Calon, J. Hall, S. Mansfield, D. Yaşar, 2005, “The Cilicia–Adana basin complex, Eastern Mediterranean: Neogene evolution of an active fore-arc basin in an obliquely convergent margin”, *Marine Geology*, Vol. 221, pp. 121–159.

Alterman, Z. and D. Loewenthal, “Seismic waves in quarter and three quarter plane”, *Geophys. J. R. Astr. Soc.*, Vol. 20, pp. 101-126, 1970.

Ambraseys, N.N., “Some characteristic features of the North Anatolian fault zone”, *Tectonophysics*, Vol. 9, pp. 143-165, 1970.

Ambreseys, N.N., “Studies in historical seismicity and tectonics”, *In Geodynamics of Today, The Royal Soc., London*, pp. 7-16, 1975.

Ambreseys, N.N. and C.F. Finkel, “Seismicity of the Northeast Mediterranean region during early 20th Century”, *Annales Geophysicae*, No: 5B, pp. 701-726, 1987.

Ambreseys, N.N., “Engineering seismology”, *Earthquake Eng. Struct. Dyn.*, Vol. 17, pp. 1-105, 1988.

Andrew, T. and A.H.F. Robertson, “The Beyşehir–Hoyran–Hadim Nappes: genesis and emplacement of Mesozoic marginal and oceanic units of the northern Neotethys in southern Turkey”, *Journal of the Geological Society, London*, Vol. 159, pp. 529-543, 2002.

Arni, P., “Keskin ve Yerköy zelzelesi hakkında”, *MTA Enst. yayını*, Seri B, 1, 1938.

Arpat, E. ve F. Şaroğlu, “Türkiye’deki bazı önemli genç tektonik olaylar”, *TJK Bülteni*, No. 18, 91-101, 1975.

Arvidsson, R., Z. Ben-Avraham, G. Ekström and S. Wdowinski, “Plate tectonic framework for the October 9, 1996, Cyprus earthquake”, *Geophysical Research Letters*, Vol. 25, No. 12, pp. 2241-2244, 1998.

Aydemir, A. and A. Ates, “Structural interpretation of the Tuzgolu and Haymana Basins, Central Anatolia, Turkey, using seismic, gravity and aeromagnetic data”, *Earth Planets and Space*, Vol. 58(8), pp. 951-961, 2006.

Babich, V.M. and A. S. Alekseyev, “A ray method of computing wave front intensities”, *Bulletin Academy of Sci. U.S.S.R., Geophysical Series*, Vol. 1, pp. 9-15, 1958.

Ballato, P., C.E. Uba, A. Landgraf, M.R. Strecker, M. Sudo, D.F. Stockli, A. Friedrich, S.H. Tabatabaei, “Arabia–Eurasia continental collision: insights from late Tertiary foreland-basin evolution in the Alborz mountains, northern Iran”. *Geol. Soc. Am. Bull.*, Vol. 123, pp. 106–131, 2011.

Barka, A. and R. Reilinger, “Active tectonics of the Eastern Mediterranean region: deduced from GPS, neotectonic and seismicity data”, *Annali di Geofisica*, Vol. XL, N. 3, pp. 587-610, 1997.

Ben-Avraham, Z., “Multiple opening and closing of the eastern Mediterranean and South China basins”, *Tectonics*, Vol. 8, pp. 351-362, 1989.

Ben-Avraham, Z., G. Tibor, A.F. Limonov, M.B. Leybov, M.K. Ivanov, M. Yu. Tokarev and J.M. Woodside, “Structure and tectonics of the eastern Cyprian Arc”, *Marine and Petroleum Geology*, Vol. 12, No. 3, pp. 263-271, 1995.

Birch, F., "The velocity of compressional waves in rocks to 10 kilobars: 2", *Journal of Geophysical Research*, Vol. 66 (7), pp. 2199-2224, 1961.

Boore, D.M., "Finite-difference methods for seismic wave propagation in heterogeneous materials, in *Methods in computational physics. v. 2: B. Alder, S. Fernbach, and M. Rotenberg. Eds., New York, Academic Press*, p. 21-22, 1972.

Bozkurt, E., "Neotectonics of Turkey-a synthesis", *Geodin. Acta*, Vol. 14, pp. 3-30, 2001.

Cady, J.W., "Calculation of gravity and magnetic anomalies of finite-length right polygonal prisms", *Geophysics*, Vol. 45, No. 10, pp. 1507-1512, 1980.

Calon, T.J, A.E. Aksu and J. Hall, "The Oligocene-Recent evolution of the Mesoria Basin (Cyprus) and its western marine extension, Eastern Mediterranean", *Marine Geology*, Vol. 221, pp. 95-120, 2005.

Cervený, V., I.A. Molotkov, I. Psencik, "Ray method in seismology", *Univerzita Karlova, Praha*, 1977.

Cervený, V., "Seismic Ray Theory", *Cambridge University Press*, Cambridge, 2001.

Clark, M.S. and A.H.F. Robertson, "The role of the Early Tertiary Ulukışla Basin, southern Turkey in suturing of the Mesozoic Tethys ocean", *J. Geol. Soc.*, Vol. 159, pp. 673-690, 2002.

Clark, M. and A.H.F. Robertson, "Uppermost Cretaceous-Lower Tertiary Ulukışla Basin, south-central Turkey: sedimentary evolution of part of a unified basin complex within an evolving Neotethyan suture zone", *Sediment. Geol.*, Vol. 173, pp. 15-51, 2005.

Desert Group, "The crustal structure of the Dead Sea Transform", *Geophysical Journal International*, Vol. 156, pp. 655-681, 2004.

Dercourt, J., L.P. Zonenshain *et al.*, “Geological evolution of the Tethys belt from the Atlantic to the Pamirs since the Lias”, *Tectonophysics*, Vol. 123, pp. 241–315, 1986.

Dewey, J.F. and A.M.C. Şengör, “Aegean and surrounding regions: complex multiplate and continuum tectonics in a convergent zone”, *Geol. Soc. Am. Bull.*, Vol. 90, pp. 84–92, 1979.

Dewey, J.F., M.R. Hempton, W.S.F Kidd, F. Şaroğlu, A.M.C. Şengör, “Shortening of continental lithosphere: the neotectonics of eastern Anatolia—a young collision zone. *In: Coward, M.P., Ries, A.C. (Eds.), Collision Tectonics. Geological Society Special Publication*, Vol. 19, pp. 3-36, 1986.

Dilek, Y. and E. Sandvol, “Seismic structure, crustal architecture and tectonic evolution of the Anatolian-African plate boundary and the Cenozoic orogenic belts in the Eastern Mediterranean region”, *Geological Society, London, Special Publications*, Vol. 327, pp. 127-160, 2009.

Dhont, D., J. Chorowicz, T. Yürür, J.L. Froger, O. Köse, N. Gündoğdu, “Emplacement of volcanic vents and geodynamics of Central Anatolia, Turkey”, *Journal of Volcanology and Geothermal Research*, Vol. 85, pp. 33–54, 1998.

Emre, Ö., T.Y. Duman, S. Özalp, H. Elmacı, Ş. Olgun, “1:250,000 scale Active Fault Map Series of Turkey, Aksaray (NJ36-7) Quadrangle”, Serial Number: 26, General Directorate of Mineral Research and Exploration, Ankara-Turkey, 2011.

Ergün, M., S. Okay, C. Sarı, E.Z. Oral, M. Ash, J. Hall, H. Miller, “Gravity anomalies of the Cyprus Arc and their tectonic implications”, *Marine Geology*, Vol. 221, pp. 349-358, 2005.

Fernandez-Blanco, D., G. Bertotti and T.A. Ciner, “Cenozoic tectonics of the Tuz Gölü Basin (Central Anatolian Plateau, Turkey)”, *Turkish Journal of Earth Sciences*, Vol. 22(5), pp. 715-738, 2013.

Fuller, C.W., S.D. Willett, M. Brandon, “Formation of forearc basins and their influence on subduction zone earthquakes”, *Geology*, Vol. 34 (2), pp. 65–68, 2006.

Galanopoulos, A. and N. Delibasis, “The seismic activity in the Cyprus area”, *Prakt. Akad. Athenon*, Vol. 40, pp. 387-405, 1965.

Gans, C.R., S.L. Beck, G. Zandt, C.B Biryol and A.A. Ozacar, “Detecting the limit of slab break-off in central Turkey: new high-resolution Pn tomography results”, *Geophysical Journal International*, Vol. 179, pp. 1566-1572, 2009.

Gass, I.G. and D. Masson-Smith, “The Geology and Gravity Anomalies of the Troodos Massif, Cyprus”, *Philosophical Transactions of the Royal Society, London*, Vol. 1060 (255), pp. 417-449, 1963.

Genç, Y. and M.T. Yürür, “Coeval extension and compression in Late Mesozoic—Recent thin skinned extensional tectonics in central Anatolia, Turkey”, *J. Struct. Geol.*, Vol. 32, pp. 623-640, 2010.

Glover, C. and A. Robertson, “Neotectonic intersection of the Aegean and Cyprus tectonic arcs: extensional and strike-slip faulting in the Isparta Angle, SW Turkey”, *Tectonophysics*, Vol. 298, pp. 103-132, 1998.

Görür, N., A.I. Okay *et al.*, “Triassic to Miocene palaeogeographic atlas of Turkey”, *MTA Enstitüsü (General Directorate of Mineral Research and Exploration)*, Ankara, 1998a.

Görür, N., O. Tüysüz and A.M.C. Şengör, “Tectonic evolution of the central Anatolian basins”, *International Geology Review*, Vol. 40, pp. 831–850, 1998b.

Grant, F. S. And G.F. West, “Interpretation theory in applied geophysics”, *McGraw-Hill Book Co., Inc., New York*, 1959.

Gürbüz, C. and J.R. Evans, “A seismic refraction study of the western Tuz Gölü basin, central Turkey”, *Geophysical Journal International*, Vol. 106, pp. 239-251, 1991.

Harrison, R.W., W.L. Newell, H. Batıhanlı, I. Panayides, J.P. McGeehin, S.A. Mahan, A. Özhür, E. Tsiolakis, M. Necdet, “Tectonic framework and Late Cenozoic tectonic history of the northern part of Cyprus: implications for earthquake hazards and regional tectonics”, *Journal of Asian Earth Sciences*, Vol. 23, Issue 2, pp. 191-210, 2004.

Helffrich, G., J. Wookey, I. Bostow, “The Seismic Analysis Code, A Primer and User’s Guide”, *Cambridge University Press*, 2013.

Hüsing, S.K., W.J. Zachariasse, D.J.J. van Hinsbergen, W. Krijgsman, M. Inceöz, M. Harzhauser, O. Mandic, A. Kroh, “Oligocene Miocene basin evolution in SE Anatolia, Turkey: constraints on the closure of the eastern Tethys gateway”, *In: van Hinsbergen, D.J.J., Edwards, M.A., Govers, R. (Eds.), Collision and Collapse at the Africa–Arabia–Eurasia Subduction Zone: Geol. Soc., Lond., Spec. Publ.*, Vol. 311, pp. 107–132, 2009.

Imprescia, P., S. Pondrelli, G. Vannucci, S. Gresta, “Regional centroid moment tensor solutions in Cyprus from 1977 to the present and seismotectonic implications”, *J. Seismol.*, Vol. 16, pp. 147-167, 2012.

Jackson, J. A., “Errors in focal depth determination and the depth of seismicity in Iran and Turkey”, *Geophys. J. R. astr. Soc.*, Vol. 61, pp. 285-301, 1980b.

Jackson, J.A. and D. McKenzie, “Active tectonics of the Alpine-Himalayan Belt between western Turkey and Pakistan”, *Geophysical Journal R. astr. Soc.*, Vol. 77, pp. 185–264, 1984.

Jackson, J.A. and D. McKenzie, “The relationship between plate motions and seismic moment tensors, and the rates of active deformation in the Mediterranean and Middle East”, *Geophysical Journal International*, Vol. 93, Issue 1, pp. 45-73, 1988.

Jaffey, N., A. Robertson, “Non-marine sedimentation associated with Oligocene–Recent exhumation and uplift of the Central Taurus Mountains, S Turkey”, *Sediment. Geol.*, Vol. 173, pp. 53–89, 2005.

Julian, B.R. and D. Gubbins, “Three dimensional seismic ray tracing”, *Journal of Geophysics*, Vol. 43, pp. 95-114, 1977.

Kalyoncuoğlu, Ü.Y., Ö. Elitok, M.N. Dolmaz, N.C. Anadolu, “Geophysical and geological imprints of southern Neotethyan subduction between Cyprus and the Isparta Angle, SW Turkey. *J. Geodyn.*, Vol. 52, pp. 70–82, 2011.

Karal, F.C. and J.B. Keller, “Elastic wave propagations in homogeneous and inhomogeneous media”, *J. Acoust. Society of America*, Vol. 31, pp. 694-705, 1959.

Kelling, G., S.L. Gökçen, P.A. Floyd, N. Gökçen, “Neogene tectonics and plate convergence in the eastern Mediterranean: new data from southern Turkey”, *Geology*, Vol. 15, pp. 425-429. 1987.

Kelly, K.R., R.W. Ward, S. Treitel and R.M. Alford, “Synthetic Seismograms: A finite-difference approach”, *Geophysics*, Vol. 41, No.1, pp. 2-27, 1978.

Kempler, D., “Eratosthenes Seamount: The possible spearhead of Incipient continental collision in the EasternMediterranean, in *Proceedings of the Ocean Drilling Program, Scientific Results ed. Robertson, A.H.F., Emeis, K.-C., Richter, C. & Camerlenghi, A.*, Vol. 160, pp. 709-721, 1998.

Ketin, I., “Tectonic units of Anatolia”, *MTA Bulletin*, Vol. 66, pp. 23-24, 1966.

Ketin, I., “Über die nordanatolische Horizontal verschiebung”, *Bull. Mineral Res. Explor. Inst. Turkey*, Vol. 72, pp. 1-28, 1969.

Kinnaird, T.C., A.H.F. Robertson, A. Morris, “Timing of uplift of the Troodos Massif (Cyprus) constrained by sedimentary and magnetic polarity evidence”, *Journal of Geological Society*, Vol. 168 (2), pp. 1-14, 2011.

Kolsky, H., “Stress waves in solid”, *Dover Publishing Co., NewYork*, 1963.

Lecomte, I., “Finite difference calculation of first traveltimes in anisotropic media”, *Geophysical Journal International*, Vol. 113, Issue 2, pp.318-342, 1993.

Lines, R. L. and R. T. Newrick, “16. Seismic Inversion. Fundamentals of Geophysical Interpretation”, *Geophysical Monograph Series*, pp.145-158, Society of Exploration Geophysics, 2004.

Luccio, F. Di. and M.E. Pasyanos, “Crustal and upper-mantle structure in the Eastern Mediterranean from the analysis of surface wave dispersion curves”, *Geophysical Journal International*, Vol. 169, pp. 1139-1152, 2007.

Mackintosh, P. W. and A.H.F. Robertson, “Late Devonian–Late Triassic sedimentary development of the central Taurides, S Turkey: implications for the northern margin of Gondwana”, *Gondwana Research*, Vol. 21, pp. 1089-1114, 2012.

Mackenzie, G.D., P.K.H. Maguire, L. A. Coogan, M.A. Khan, M. Eaton and G. Petrides, “Geophysical constraints on the crustal architecture of the Troodos ophiolite: results from the IANGASS project”, *Geophysical Journal International*, Vol. 167 (3), pp. 1385-1401, 2006.

Makris, J., Z. Ben-Avraham, A. Behle, A. Ginzburg, P. Giese, L. Steinmetz, R.B. Whitmarsh and S. Eleftherion, “Seismic refraction profiles between Cyprus and Israel and their interpretation”, *Geophys. J. R. Astron. Soc.*, Vol. 75, pp. 575-591, 1983.

Makris, J. and J. Wang, “Bouguer gravity anomalies of the Eastern Mediterranean Sea”, *Geological Structure of the Northeastern Mediterranean (Cruise 5 of the Research Vessel ‘Akademik Nikolaj Strakov’)*, *Geological Survey of Israel, TelAviv*, pp. 87-98, 1994.

Mart, Y. and H.F. Robertson, “Eratosthenes seamount: an oceanographic yardstick recording the late Mesozoic: tertiary geological history of the Eastern Mediterranean”, in *Proceedings of the Ocean Drilling Program, Scientific Results*, ed. Robertson, A.H.F., Emeis, K.-C., Richter, C. & Camerlenghi, A., Vol. 160, pp.701-708, 1998.

McClain, J.S., and D. W. Caress, "Seismic tomography in marine refraction experiments", *Seismic Tomography: Theory and Practice* edited by H. M. Iyer and K. Hirahara, pp. 848, Chapman and Hall, London, 1993.

McClusky, S., S. Balassanian, A. Barka, C. Demir, S. Ergintav, I. Georgiev, O. Gurkan, M. K. Hamburger, K. Hurst, H. Kahle, K. Kastens, G. Kekelidze, R. King, V. Kotzev, O. Lenk, S. Mahmoud, A. Mishin, M. Nadariya, A. Ouzounis, D. Paradissis, Y. Peter, M. Prilepin, R. Reilinger, I. Sanli, H. Seeger, A. Tealeb, M.N. Toksoz and G. Veis, "Global Positioning System constraints on plate kinematics and dynamics in the eastern Mediterranean and Caucasus", *Journal of Geophysical Research*, Vol. 15, pp. 5695-5720, 2000.

McKenzie, D.P., "Plate tectonics of the Mediterranean region", *Nature*, Vol. 226, pp. 239-243, 1970.

Mechie, J., K. Abu-Ayyash, Z. Ben-Avraham, R. El-Kelani, A. Mohsen, G. Rumpker, J. Saul, M. Weber, "Crustal shear velocity structure across the Dead Sea Transform from two-dimensional modelling of DESERT project explosion seismic data", *Geophysical Journal International*, Vol. 160, Issue 3, pp. 910-924, 2005.

Mechie, J., Z. Ben-Avraham, M.H. Weber, H.J. Götze, I. Koulakov, A. Mohsen, M. Stiller, "The distribution of Moho depths beneath the Arabian plate and margins", *Tectonophysics*, Vol. 609, pp. 234-249, 2013.

Mutlu, A. and H. Karabulut, "Anisotropic Pn tomography of Turkey and adjacent regions", *Geophysical Journal International*, Vol. 187, Issue 3, pp. 1743-1758, 2011.

Mitchell, A. R., "Computational methods in partial differential equations", *John Wiley & Sons., New York*, 1969.

Monod, O., "Recherches Geologique dans les Taurus occidental au sud de Beyşehir (Turquie)", *These de Doctorat de Science, Univesite de Paris-Sud, Orsay, France*, 1977.

Moser, T.J., "Efficient seismic ray tracing using graph theory", *Society of Exploration Geophysics, Meeting, Expanded abstracts*, pp. 1106-1108, SEG, Tulsa, OK, 1989.

Nafe, J.E. and C.L. Drake, "Variation with depth in shallow and deep water marine sediments of porosity, density and the velocities of compressional and shear waves", *Geophysics*, Vol. 22(3), pp. 523-552, 1957.

Okay, A.I., "Was the Late Triassic orogeny in Turkey caused by the collision of an oceanic plateau?", *Geological Society, London, Special Publications*, Vol. 173, pp. 25-41, 2000.

Okay, A.I., "Geology of Turkey: a synopsis", *Der Anschnitt*, Vol. 21, pp. 19-42, 2008.

Özeren, M.S. and W.E. Holt, "The dynamics of the easternMediterranean and eastern Turkey", *Geophysical Journal International*, Vol. 183, pp. 1165-1184, 2010.

Özsayın, E. and K. Dirik, "Quaternary activity of the Cihanbeyli and Yeniceoba fault zones: İnönü–Eskişehir fault system, Central Anatolia", *Turk. J. Earth Sci.*, Vol. 16, pp. 471-492, 2007.

Özgül, N., "Some basic geological features of the Taurides", *Türkiye Jeoloji Kurumu Bülteni*, Vol. 19, pp. 65–78, 1976.

Özgül, N., "Stratigraphy and tectonic evolution of the Central Taurides", in *Geology of the Taurus Belt*, edited by O. Tekeli and C. Göncüoğlu, *Spec. Pub.*, MTA, Ankara, pp. 77-90, 1983.

Özgül, N., "Stratigraphy and tectonic evolution of the central Taurides. In: Tekeli, O. & Göncüoğlu, M.C. (eds) *Geology of the Taurus Belt, Proceedings of the International Symposium, Maden Tetkik ve Arama, Ankara*, pp. 77–90, 1984a.

Özgül, N., "Geology of the Alanya tectonic window and its western part", *TJK Ketin Sempozyumu*, pp. 97–120, 1984b.

Özgül, N., “Stratigraphy of the tectono-stratigraphic units in the region Bozkır-Hadim-Taşkent (northern central Taurides)”, *Maden Tetkik ve Arama Dergisi*, Vol. 119, pp. 113–174, 1997.

Öztin, F. and N. Bayülke, “Historical earthquakes of Istanbul, Kayseri and Elazığ”, *In Proceedings Workshop on Historical Seismicity and Seismotectonics of the Mediterranean region*, Turkish Atomic Energy Authority, Ankara, Turkey, pp.234-253, 1990.

Papazachos, B.C. and Ch. A. Papaioannou, “Lithospheric boundaries and plate motions in the Cyprus area”, *Tectonophysics*, Vol. 308, pp. 193–204, 1999.

Parejas, E. and H.N. Pamir, “19/4/1938 orta Anadolu yer depremi”, *İstanbul Üniversitesi Fen Fak. Meo. b IV*, 3/4, 1939.

Payne, A.S. and A.H.F. Robertson, “Structural evolution and regional significance of the Polis graben system, western Cyprus”, *In: Panayides, I., Xenophontos, C., Malpas, J. (Eds.), Proceedings of the Third International Conference on the Geology of the Eastern Mediterranean. Geological Survey Department, Republic of Cyprus, Nicosia, Cyprus*, pp. 45-49, 23-26 Sept, 2000.

Platzman, E.S., C. Tapirdamaz and M. Sanver, “Neogene Anticlockwise rotation of Central Anatolia (Turkey): preliminary palaeomagnetic and geochronological results”, *Tectonophysics*, Vol. 299, pp. 175–189, 1998.

Podvin, P. and I. Lecomte, “Finite difference computation of traveltimes in very contrasted velocity models: a massively parallel approach and its associated tools”, *Geophysical Journal International*, Vol. 105, pp. 271-284, 1991.

Pourteau, A., O. Candan, R. Oberhänsli, “High-pressure metasediments in central Turkey: constraints on the Neotethyan closure history”, *Tectonics*, Vol. 29, TC5004, doi:10.1029/2009TC002650, 2010.

Press, W.H., B.P. Flannery, S. A. Teukolsky and W.T. Vetterling, “Numerical Recipes The Art of Scientific Computing”, *Cambridge University Press*, 1986.

Reshef, M. and D. Kosloff, "Migration of common shot gathers", *Geophysics*, Vol. 51, pp. 324-331, 1986.

Reynolds, A.C., "Boundary conditions for the numerical solution of wave propagation problems", *Geophysics*, Vol. 43, No. 6, pp. 1099-1110, 1978.

Richter, C.F., "Elementary Seismology", edited by J. Grithhely and A.O. Woodford (W.H. Freeman and Company, San Francisco), pp. 550, 1958.

Riznichenko, Yu. V., "Geometrical seismics of layered media", *Trudy Inst. Theor. Geophysics*, Vol. 11, *Izd. An. SSSR*, Moscow (in Russian), 1946.

Robertson, A.H.F and J.D. Dixon, "Introduction: aspects of the Geological Evolution of the Eastern Mediterranean. In: Dixon, J. E. & Robertson, A.H.F. (eds) *The Geological Evolution of the Eastern Mediterranean. Geological Society, London, Special Publications*, Vol. 17, pp. 1-74, 1984.

Robertson, A.H.F. and N.H.Woodcock, "The role of the Kyrenia Range lineament, Cyprus, in the geological evolution of the eastern Mediterranean area", *Philos. Trans. R. Soc. A.*, Vol. 317, pp. 141-177, 1986.

Robertson, A.H.F., P.D. Clift, P.J. Degan and G. Jones, "Palaeogeographical and palaeotectonic evolution of the Eastern Mediterranean Neotethys", *Palaeoceanography, Palaeoclimatology, Palaeoecology*, Vol. 87, pp. 289-343, 1991.

Robertson, A.H.F., J.E. Dixon, S. Brown, S. Collins, E. Pickett, I. Sharp, T. Ustafmer, "Alternative tectonic models for the Late Palaeozoic-Early Tertiary development of Tethys in the Eastern Mediterranean region", In: Morris, A., Tarling, D.H. (Eds.), *Palaeomagnetism and Tectonics of the Mediterranean Region: Geol. Soc., Lond., Spec. Publ.*, Vol. 105, pp. 239-263, 1996.

Robertson, A.H.F., "Mesozoic-Tertiary tectonic evolution of the easternmost Mediterranean area: integration of marine and land evidence. In: Robertson, A.H.F., Emeis,

K.C., Richter, C., Camerlenghi, A. (Eds.), *Proceeding of the Ocean Drilling Program, Scientific Results*, Vol. 160, pp. 723–782, 1998.

Robertson, A.H.F., “Mesozoic–Tertiary tectonic–sedimentary evolution of a south Tethyan basin and its margins in southern Turkey”, *In: Bozkurt, E., Winchester, J.A., Piper, J.D.A. (Eds.), Tectonics and Magmatism in Turkey and the Surrounding Area: Geol. Soc., Lond., Spec. Publ.*, Vol. 173, pp. 97–138, 2000.

Robertson, A.H.F., O. Parlak and T. Ustaömer, “Overview of the Palaeozoic–Neogene evolution of Neotethys in the Eastern Mediterranean region (southern Turkey, Cyprus, Syria)”, *Petroleum Geoscience*, Vol. 18, pp. 381–404, 2012b.

Robertson, A.H.F., “Overview of tectonic settings related to the rifting and opening of Mesozoic ocean basins in the Eastern Tethys: Oman, Himalayas and Eastern Mediterranean regions”, *In: Karner, G., Manatschal, G. & Pinheiro, L. M. (eds) Imaging, Mapping and Modelling Continental Lithosphere Extension and Breakup, Geological Society, London, Special Publications*, Vol. 282, pp. 325–389, 2007.

Robertson, A.H.F., O. Parlak and T. Ustaömer, “Late Palaeozoic–Early Cenozoic tectonic development of Southern Turkey and the easternmost Mediterranean region: evidence from the inter-relations of continental and oceanic units”, *Geological Society, London*, Vol. 372, pp. 9–48, 2013.

Rotstein, Y. and A.L. Kafka, “Seismotectonics of the southern boundary of Anatolia, eastern Mediterranean region: subduction, collision and arc jumping”, *Journal of Geophysical Research*, Vol. 87, pp. 7694–7706, 1982.

Sandmeier, K.J., “Untersuchung der Ausbreitungseigenschaften seismischer Wellen in geschichteten und streuenden Medien”, *PhD thesis*, Karlsruhe University, Karlsruhe, 1990.

Saito, H., “Traveltimes and raypaths of first arrival seismic waves: computation method based on Huygens’ principle”, *SOC. Exploration Geophys. 1989 Meeting*, Expanded abstracts, pp. 244–247, SEG, Tulsa, OK., 1989.

Saito, H., “3-D ray tracing method based on Huygens’ principle”, *SOC. Exploration Geophys. 1990 Meeting*, Expanded abstracts, pp. 1024-1027, SEG, Tulsa, OK, 1990.

Sarođlu, F., E. Boray, S. Özer and İ. Kuşçu, “Orta Toroslar-Orta Anadolu’nun güneyinin neotektoniđi ile ilgili görüřler”, *Jeomorfoloji Dergisi*, Vol. 11, pp. 35-44, 1983.

Schildgen, T.F., D. Cosentino, B. Bookhagen, S. Niedermann, C. Yıldırım, H. Echtler, H. Wittmann, M.R. Strecker, “Multi-phased uplift of the southern margin of the Central Anatolian plateau, Turkey: A record of tectonic and upper mantle processes”, *Earth and Planetary Science Letter*, (317-318), pp. 85-95, 2012a.

Schildgen, T.F., D. Cosentino, A. Caruso, R. Buchwaldt, C. Yıldırım, S.A. Bowring, B. Rojay, H. Echtler, M.R. Strecker, “Surface expression of Eastern Mediterranean slab dynamics: Neogene topographic and structural evolution of the SW margin of the Central Anatolian Plateau, Turkey”, *Tectonics*, Vol. 31, TC2005. <http://dx.doi.org/10.1029/2011TC003021>, 2012b.

Schildgen, T., C. Yildirim, D. Cosentino and M. Strecker, “Linking slab break-off, Hellenic trench retreat, and uplift of the Central and Eastern Anatolian plateaus”, *Earth Science Reviews*, Vol. 128, pp. 147-168, 2014.

Schneider, W.A. Jr., K.A. Ranzinger, A.H. Balchs and C. Kruse, “A dynamic programming approach to first arrival travelttime computation in media with arbitrarily distributed velocities”, *Geophysics*, Vol. 57, No. 1, pp. 39-50, 1992.

Sharma, P.V., “Chapter 12. Inversion theory and tomography”, *Environmental and engineering geophysics*, Cambridge University Press, United Kingdom, 1997.

Shelton, A.W., “Troodos revisited: The Mount Olympus gravity anomaly”, in *Magmatic Processes and Plate Tectonics*, Prichard, H.M., Alabaster, T., Harris, N.B.W. & Neary, C.R., Geological Society London, Special Publication, Vol. 76, pp. 197-212, 1993.

Şengör, A.M.C. and Y. Yılmaz, Y., “Tethyan evolution of Turkey: a plate tectonic approach”, *Tectonophysics*, Vol. 75, pp. 181–241, 1981.

Şengör, A.M.C., Y. Yılmaz and O. Süngürlü, “Tectonics of the Mediterranean Cimmerides: nature and evolution of the western termination of Palaeo-Tethys. In: Dixon, J.E., Robertson, A.H.F. (Eds.), *The Geological Evolution of the Eastern Mediterranean*, Geol. Soc., Lond., Spec. Publ., Vol. 17, pp. 77–112, 1984.

Şengör, A.M.C., N. Görür, F. Saroglu, “Strike-slip faulting and basin related formation in zones of tectonic escape”, *Soc. Econ. Paleontol. Mineral. Spec. Publ.*, Vol. 37, pp. 227–440, 1985.

Şengör, A.M.C., O. Tüysüz, C. Imren, M. Sakıncı, H. Eyidogan, N. Gorur, X. LePichon, Rangin, C., “The North Anatolian Fault: a new look”, *Ann. Rev. Earth planet. Sci.*, Vol. 33, pp. 37–112, 2005.

Talwani, M., J.L. Worzel and M. Landisman, “Rapid gravity computations for two-dimensional bodies with application to the Mendocino submarine fracture zone, *Journal of Geophysical Research*, Vol. 64, pp. 49-59, 1959.

Talwani. M. And J.R. Heirtzler, “Computation of magnetic anomalies caused by two-dimensional structures of arbitrary shape”, in *Computers in the mineral industries: G. Parks, Edition, Stanford Univ.*, pp. 464-480, 1964.

Tan, O. and T. Taymaz, “Active tectonics of the Caucasus: earthquake source mechanisms and rupture histories obtained from inversion of teleseismic body-waveforms, in Post-Collisional Tectonics and Magmatism in the Mediterranean Region and Asia”, *Geological Society of America*, Special Paper 409, pp.531-578, 2006.

Taymaz, T., J. Jackson and D.P. Mckenzie, “Active tectonics of the North and Central Aegean Sea”, *Geophysical Journal International*, Vol. 106, pp. 433-490, 1991a.

Taymaz, T., H. Eyidogan and J.A. Jackson, “ Source Parameters of large earthquakes in the East Anatolian Fault Zone (Turkey)”, *Geophysical Journal International*, Vol. 106, pp.537-550, 1991b.

Taymaz, T., Y. Yilmaz, and Y. Dilek, “The geodynamics of the Aegean and Anatolia: introduction”, *Geological Society, London, Special Publications*, Vol. 291, pp. 1-16, 2007.

Taymaz, T., T. Wright, S. Yolsal, O. Tan, E. Fielding, G. Seyitoğlu, “Source characteristics of June 6, 2000 Orta-Çankırı (Central Turkey) earthquake: a synthesis of seismological, geological and geodetic (InSAR) observations, and internal deformation of Anatolian plate, *In: Taymaz, Tuncay, Yılmaz, Yücel, Dilek, Yıldırım (Eds.), The Geodynamics of the Aegean and Anatolia. The Geological Society of London, Special Publications Book*, Vol. 291. ISBN: 978-1-86239-239-7, pp. 259–290, 2007b.

Ten Veen, J.H., J.M. Woodside, T.A.C. Zitter, J.F. Dumont, J. Mascle and A. Volkonskaia, “Neotectonic evolution of the Anaximander Mountains at the junction of the Hellenic and Cyprus arcs”, *Tectonophysics*, Vol. 391, pp. 35-65, 2004.

Tezel, T., T. Shibutani and B. Kaypak, “Crustal thickness of Turkey determined by receiver function”, *Journal of Asian Earth Sciences*, Vol. 75, pp. 36-45, 2013.

Thornburgh, H. R., “Wave-front diagrams in seismic interpretation”, *AAPG Bull.*, Vol. 14, pp. 185-200, 1930.

Thurber, C.H., “Local earthquake tomography: velocities and V_p / V_s – theory”, *Seismic Tomography: Theory and Practice* edited by H.M. Iyer and K. Hirahara, *published by Chapman & Hall, 2-6 Boundary Row, London*, 1993.

Wdowinski, S., Z. Ben-Avraham, R. Arvidsson and G. Ekström, “Seismotectonics of the Cyprian Arc”, *Geophysical Journal International*, Vol. 164, pp. 176-181, 2006.

Williams, G.D., U.C. Ünlügenç, G. Kelling, C. Demirkol, “Tectonic controls on stratigraphical evolution of the Adana basin”, *J. Geol. Soc.*, Vol. 152, pp. 873–882, 1995.

www.moa.gov.cy, Republic of Cyprus, Ministry of Agriculture, Rural Development and Environment, Geological Survey Department/Sediments.

www.moa.gov.cy, Republic of Cyprus, Ministry of Agriculture, Rural Development and Environment, Geological Survey Department/Tectonic Evolution.

www.moa.gov.cy, Republic of Cyprus, Ministry of Agriculture, Rural Development and Environment, Geological Survey Department/Troodos.

www.sw3d.mff.cz, Cerveny, V. and I. Psencik, "Numerical Modelling of Seismic Wave Fields in 2-D Laterally Varying Layered Structures by The Ray Method", *Program Seis88 manual*.

www.wikipedia.org, Geology of Cyprus.

Vanacore, E.A., T. Taymaz and E. Saygin, "Moho structure of the Anatolian Plate from receiver function analysis", *Geophysical Journal International*, Vol. 193, pp. 329-337, 2013.

Van Trier, J. and W.W. Symes, "Upwind finite-difference calculation of seismic traveltimes", *SOC. Exploration Geophys. 1990 Meeting*, Expanded abstracts, pp. 1000-1002, SEG, Tulsa, OK., 1990.

Van Trier, J. and W.W. Symes, "Upwind finite-difference calculation of traveltimes", *Geophysics*, Vol. 56, pp. 812-821, 1991.

Vidale, J., "Finite-Difference Calculation of Travel Times", *Bulletin of the Seismological Society of America*, Vol. 78, No. 6, pp. 2062-2076, 1988.

Vidale, J., "Finite-difference calculation of traveltimes in 3-D", *Geophysics*, Vol. 55, pp. 521-526, 1990.

Yolsal-Çevikbilen, S. and T. Taymaz, “Earthquake source parameters along the Hellenic subduction zone and numerical simulations of historical tsunamis in the Eastern Mediterranean”, *Tectonophysics*, Volumes 536–537, pp. 61-100, 2012.

Yıldırım, C., T.F. Schildgen, H. Echtler, D. Melnick, M.R. Strecker, “Late Neogene orogenic uplift in the Central Pontides associated with the North Anatolian Fault-implications for the northern margin of the Central Anatolian Plateau, Turkey”, *Tectonics*, Vol. 30, TC5005.doi:10.1029/2010TC002756, 2011.

Yıldırım, C., “Relative tectonic activity assessment of the Tuz Gölü Fault Zone; Central Anatolia, Turkey”, *Tectonophysics*, Vol. 630, pp. 183-192, 2014.

Yılmaz, Y., O. Tüysüz, E. Yiğitbaş, S.C. Genç, A.M.C. Şengör, “Geology and tectonic evolution of the Pontides”, In: *Robinson, A.G. (Ed.), Regional and Petroleum Geology of the Black Sea and Surrounding Region: Am. Assoc. Petroleum Geologists Memoir, Tulsa, OK*, Vol. 68, pp. 183–266, 1997.